UNIVERSITY OF CALIFORNIA SAN DIEGO

Seismic Behavior of Deep and Slender Steel Columns through Full-Scale Cyclic and Hybrid Testing

A Dissertation submitted in partial satisfaction of the requirements
for the degree Doctor of Philosophy

in

Structural Engineering

by

Claudio Sepulveda

Committee in charge:

Gilberto Mosqueda, Co-Chair
Chia-Ming Uang, Co-Chair
Chung-Che Chou
John L. Harris
Mauricio de Oliveira
Pui-Shum Shing

2024

The Dissertation of Claudio Sepulveda is approved, and it is acceptable in quality and form for publication on microfilm and electronically.

University of California San Diego

2024

TABLE OF CONTENTS

LIST OF FIGURES

LIST OF TABLES

ACKNOWLEDGEMENTS

I would like to express my deepest gratitude to my advisor, Professor Gilberto Mosqueda, for his unwavering support and guidance throughout my PhD journey. His technical expertise and insightful feedback were instrumental in shaping this dissertation. I am equally grateful for his constant encouragement and belief in me, which helped me navigate challenges and reach my full potential. Beyond his professional guidance, I deeply appreciate his genuine concern for my well-being, always ensuring that my journey was not just academically enriching but also personally fulfilling. I also extend my appreciation to Professor Chia-Ming Uang, whose teachings in seismic design and steel structure testing have been invaluable to my research. His willingness to engage in brainstorming sessions, even on topics beyond his expertise, led to many insightful ideas that significantly contributed to my work.

I appreciate the tremendous technical support and huge hospitality of all the people from the National Center for Research on Earthquake Engineering of Taiwan, NCREE, starting for his director Professor Chung-Che Chou, Dr Kung-Juin Wang, Cheng-Wei Huang, Po-Chia Huang, and the rest of the NCREE team.

I would like to acknowledge the valuable input and guidance provided by Professor Gülen Özkula, Professor Tracy Becker, Dr. Mao Cheng, Dr. Andreas Schellenberg, and Professor Javad Hashemi. I appreciate also the feedback provided by the committee members, Professor Pui-Shum (Benson) Shing, Dr. John L. Harris, and Professor Mauricio de Oliveira.

This accomplishment would not be possible without the constant support from my partner Natalia, whose understanding have been my anchor throughout this demanding journey. Additionally, I am grateful for the friends I have made during this time, whose companionship and

support have enriched this experience. Special thanks to Ricardo and Franco for the enriching technical conversations and brainstorming sessions that have greatly contributed to my research. I must express my profound gratitude to my family, whose values and upbringing have been fundamental in shaping the person I am today.

Thanks to the NIST project title "Resilience of Steel Moment Frame Systems with Deep Slender Column Sections" for providing funding to conduct this research. Thanks to the US Fulbright Program, National Research and Development Agency of Chile (ANID, folio 72200073), and Universidad Tecnica Federico Santa María, for funding my studies.

Chapter 3, in part, is currently being prepared for publication of the material as it may appear in "Full-scale quasi-static and hybrid simulation of steel moment frame with deep and slender columns", C. Sepulveda, G. Ozkula, G. Mosqueda, C.M. Uang, C.C. Chou, K.J. Wang, C.W. Huang, P.C. Huang, S. El-Tawil, J. McCormick. *Earthquake Engineering and Structural Dynamics*. The dissertation author was the primary researcher and author of this paper.

Chapter 4, in part, is a reprint of the material as it appears in "Hybrid simulation framework with mixed displacement and force control for fully compatible displacements." C. Sepulveda, G. Mosqueda, K.J. Wang, P.C. Huang, C.W. Huang, C.M. Uang, C.C. Chou (2023). *Earthquake Engineering and Structural Dynamics*. https://doi.org/10.1002/eqe.4048. The dissertation author was the primary researcher and author of this paper.

Chapter 5, in part, has been submitted for publication of the material as it may appear in "Selective online model updating in hybrid simulation of a full-scale steel moment frame" C. Sepulveda, M. Cheng, T. Becker, G. Mosqueda, K.J. Wang, P.C. Huang, C.W. Huang, C.M. Uang, C.C. Chou (2024): *Earthquake Engineering and Structural Dynamics*. The dissertation author was the primary researcher and author of this paper.

VITA

2016 Bachelor of Science in Civil Engineering, Universidad Técnica Federico Santa María

2016 Master of Science in Civil Engineering, Universidad Técnica Federico Santa María

2024 Doctor of Philosophy in Structural Engineering, University of California San Diego

PUBLICATIONS

Journal Papers:

C. Sepulveda, G. Mosqueda, K.J. Wang, P.C. Huang, C.W. Huang, C.M. Uang, C.C. Chou (2023): "Hybrid simulation framework with mixed displacement and force control for fully compatible displacements." *Earthquake Engineering and Structural Dynamics.* https://doi.org/10.1002/eqe.4048

K.J. Wang, C.C. Chou, C.W. Huang, H.K. Shen, **C. Sepulveda**, G. Mosqueda, C.M. Uang (2023): "Hybrid simulation of a steel dual system with buckling-induced first-story column shortening: A mixed control mode approach." *Earthquake Engineering and Structural Dynamics.* https://doi.org/10.1002/eqe.3944

C. Sepulveda, M. Cheng, T. Becker, G. Mosqueda, K.J. Wang, P.C. Huang, C.W. Huang, C.M. Uang, C.C. Chou (2024): "Selective online model updating in hybrid simulation of a full-scale steel moment frame." *Earthquake Engineering and Structural Dynamics.* (in review)

C. Sepulveda, G. Ozkula, G. Mosqueda, C.M. Uang, C.C. Chou, K.J. Wang, C.W. Huang, P.C. Huang, S. El-Tawil, J. McCormick (2024): "Full-scale quasi-static and hybrid simulation of steel moment frame with deep and slender columns." *Earthquake Engineering and Structural Dynamics.* (In Preparation)

R. Bustamante, K. Erler, **C. Sepulveda**, G. Mosqueda, M. Del Carpio, J. Lopez, K.J. Elwood (2024): "Seismic Isolation Retrofit Following Early Design Standards: A Case Study" (In Preparation)

A. Braniff, D. Kusanovic, **C. Sepulveda** (2024): "Evaluation of seismic isolation systems for mid-rise buildings considering high-fidelity soil-structure interaction." *Earthquake Engineering and Structural Dynamics.* (In Preparation)

H. Gomez, P. Heresi, **C. Sepulveda** (2024): "Retrofit Alternative Assessment of Steel Moment Frame Portfolio Based on Expected Economic Losses." *Earthquake Spectra* (In Preparation)

Conference Papers:

C. Sepulveda, G. Mosqueda, C.M. Uang, G. Ozkula, C.C. Chou, K.J. Wang, C.W. Huang, P.C. Huang, M. Cheng, T. Becker, S. El-Tawil, J. McCormick (2024): "Full-Scale Testing of Steel Moment Frames Cruciform Subassemblies Towards System-Level Behavior Analysis" *18th World Conference on Earthquake Engineering*, Italy

C. Sepulveda, G. Mosqueda, K.J. Wang, C.W. Huang, B.C. Huang, C.M. Uang, C.C. Chou (2024): "Performance Assessment of Mixed Displacement and Force Control Framework for Hybrid Simulation" *18th World Conference on Earthquake Engineering*, Italy

G. Mosqueda, **C. Sepulveda**, R. Bustamante (2024): "Performance of Seismically Isolated Bridge Considering Abutment Pounding" *18th World Conference on Earthquake Engineering*, Italy

K.J. Wang, C.C. Chou, C.W. Huang, H.K. Shen, **C. Sepulveda**, G. Mosqueda, C.M. Uang (2024): "Hybrid Simulation Using Mixed Displacement Force Control with Column Shortening Compatibility" *18th World Conference on Earthquake Engineering*, Italy

G. Ozkula, **C. Sepulveda**, G. Mosqueda, C.M. Uang (2024): "Seismic Compactness Requirement for I-Shaped Columns with Varying Axial Load" *11th International Conference on the Behaviour of Steel Structures in Seismic Areas*, Italy

H. Gomez, P. Heresi, **C. Sepulveda** (2023): "Evaluación de Alternativas de Reforzamiento Estructural en Edificios de Marcos de Acero en Función de las Pérdidas Económicas Esperadas." *XIII Chilean Conference on Seismology and Earthquake Engineering*, Chile

C. Sepulveda, G. Mosqueda (2023): "Performance Assessment of a Mixed Displacement and Force Control Mode for Hybrid Simulation." *XIII Chilean Conference on Seismology and Earthquake Engineering*, Chile

C. Sepulveda, G. Mosqueda, C.M. Uang, K.J. Wang, C.C. Chou (2023): "Hybrid simulation of a steel dual system with buckling-induced first-story column shortening: A mixed control mode approach." *XIII Chilean Conference on Seismology and Earthquake Engineering*, Chile

C. Sepulveda, R. Bustamante, G. Mosqueda (2023): "Seismic Performance of Isolated Bridges Under Extreme Shaking." 17th *World Conference on Seismic Isolation*, Italy

C. Sepulveda, G. Mosqueda, C.M. Uang, G. Ozkula, K.J. Wang, C.C. Chou, P.C. Huang, C.W. Huang, M. Cheng, T. Becker (2022): "Hybrid Simulation of Moment Frames With Deep Columns Experiencing Axial Shortening." *8th Asia Conference on Earthquake Engineering*, Taiwan

R. Bustamante, K. Erler, **C. Sepulveda**, G. Mosqueda, M. Del Carpio, M. Hershberg, J. Lopez, K. Elwood (2022): "Evaluation of Seismically Isolated Structures Designed to Early Standards." *13th HSTAM International Congress on Mechanics*, Greece

K.J. Wang, C.C. Chou, C.W. Huang, H.K. Shen, M.H. Tam, **C. Sepulveda**, G. Mosqueda, C.M. Uang (2022): "Hybrid Simulation of a Seven-story BRBF Using a Mixed Displacement and Force Control Method on the First-story Beam-to-column Subassemblage." *12th National Conference on Earthquake Engineering*, USA

C. Sepulveda, G. Mosqueda, C.M. Uang, C.C. Chou, K.J. Wang (2022): "Hybrid Simulation Using Mixed Displacement and Equivalent-Force Control to Capture Column Shortening in Frame Structures." *12th National Conference on Earthquake Engineering*, USA

Technical Reports:

C. Sepulveda, R. Bustamante, G. Mosqueda (2024): "Seismic Performance of Isolated Bridges Under Beyond Design Basis Shaking." *Technical Report PEER 2024/02* Pacific Earthquake Engineering Research Center, University of California, Berkeley

E. Fischer, S. Aldea, J. Archbold, J. Bantis, M. Bravo, L. Ceferino, J. Carrillo, K. Cheng, D. Cordero, A. Elkady, H. Guerrero, S. Gunay, M. Hakhamaneshi, P. Heresi, C. Hoepfinger, Z. Khalil, V. Mathur, A. Martin, A. Metz, Z. Mijic, E. Miranda, C. Pajaro, A. Poulos, **C. Sepulveda,** E. Toraman, A. Wein, K. Wu, J. Zambrano, J. Zhang (2022): "EERI: Lugu, Taiwan September 18, 2022, Mw 6.9 Earthquake." DesignSafe-CI. https://doi.org/10.17603/ds2-65yg-nn97

ABSTRACT OF THE DISSERTATION

Seismic Behavior of Deep and Slender Steel Columns through Full-Scale Cyclic and Hybrid Testing

by

Claudio Sepulveda

Doctor of Philosophy in Structural Engineering

University of California San Diego, 2024

Gilberto Mosqueda, Co-Chair
Chia-Ming Uang, Co-Chair

Steel moment frames composed of wide flange steel members are commonly used in seismic regions, with deep and slender column sections often selected to economically satisfy drift limit requirements. The section slenderness makes the columns more susceptible to local and global buckling and subsequent axial shortening when subjected to combined axial forces and lateral deformations. Numerous tests have been conducted on isolated column members under a

wide range of axial loads and loading patterns. Experimental data of subassembly or complete frame configurations providing insight into system level interaction of the column with other members in the frame are very limited. This study presents experimental observations from a full-scale testing program conducted on four cruciform beam-to-column subassemblages subjected to loading patterns based on both symmetric quasi-static cyclic loading and hybrid simulation. The experimental results are compared with previous testing of individual columns and the data is used towards developing column models that can capture axial shortening. A column hinge macro-element is developed to assess the expected axial shortening due to column buckling and effects on the building structure.

The hybrid simulations conducted as part of this test program required a novel framework to apply mixed displacement- and force-controlled loading on the experimental substructures. A full nonlinear model of a complete frame was developed for the numerical substructure that interacts with the subassembly applying displacements for lateral loading and the axial load in force control. The framework uses a controller-based transformation to satisfy both force equilibrium and displacement compatibility between the experimental substructure experiencing shortening and the numerical model. The numerical substructure and the overall substructuring strategy of the hybrid simulation is further improved by implementing an online model updating algorithm to update the numerical beam hinge parameters based on the latest measured response during the test. These tests also include one of the most advanced applications of model updating with hybrid simulation on a large and complex structural system.

Chapter 1 Introduction

1.1. General

Wide flange steel column members are commonly used for steel moment frames in seismic regions. Following the 1994 Northridge Earthquake, more restrictive drift requirements for buildings [1] resulted in the use of deep columns with increased moment of inertia and stiffness with minimal sectional area. However, deep columns are susceptible to experiencing local and global buckling that can result in axial shortening [2] and significantly degrade member resistance [3,4]. An accurate prediction of the residual deformation including axial shortening impacts the reparability or the potential need for demolition [5]. Axial shortening may also produce a redistribution of vertical forces between adjacent columns due to the differential settlement.

Numerical simulations using high-fidelity finite elements models have been carried out for single wide flange columns to characterize their stability under combined axial and lateral loads [6–9]. Experiments have been conducted on individual column members to characterize this behavior under quasi-static load patterns at various axial loads [10,11]. Those studies have exposed the effects of the axial load magnitude and pattern, inelastic deformation, and boundary conditions on the resulting axial shortening [2,12]. While the impact of column buckling and subsequent axial

shortening has been numerically examined from a system-level point of view [13–15], there is limited experimental data for system-level verification.

Full-scale physical testing of structural components under simulated seismic loading provides valuable data to verify numerical models, especially for complex behavior such as column buckling. While shaking table testing is considered one of the most realistic and reliable testing methods, full-scale testing can be cost-prohibitive in this case requiring multi-story, multi-bay frames. Quasi-static subassembly tests are a more economical and viable option for testing structural members at full-scale. This testing method has standard loading protocols that have been widely applied to define acceptance criteria for beam-to-column connections subjected to a design-basis earthquake [16]. Nonetheless, this predefined cyclic load pattern may not always serve as a proper representation of the actual seismic demand. Hybrid simulation (HS) is a method that combines physical testing using the same equipment as for quasi-static testing, with the loading driven by a numerical model subjected to a ground acceleration record. The experimental substructure is selected to represents the most complex and interesting part of the structure that is challenging to simulate and interacts with the rest of the numerical structure to capture the system level behavior.

1.2. Research Objective and Scope

The goal of this study is to experimentally assess the system behavior of moment frame structures with deep and slender columns by conducting quasi-static tests and hybrid simulations (HS), including full-scale cruciform subassemblies. Tests were conducted at the National Center for Research on Earthquake Engineering (NCREE) in Taiwan. Quasi-static tests are performed

first to assess the cyclic behavior of the subassembly employing standard protocols. Advanced HS are conducted to quantify the structural damage of the system due to seismic-induced loads.

A novel framework was developed for hybrid simulation with mixed displacement and force control using a controller-based displacement-to-force transformation for stiff DOFs. The framework can be implemented with displacement-based time-integration schemes and is demonstrated here using the widely used OpenSees [17] and OpenFresco [18] platforms. Force-controlled experimental DOFs are applied as in past studies, then compatibility with the numerical model is imposed by transforming the experimentally measured displacement into an equivalent nodal force updated at each integration time-step. The controller transformation can be tuned to reduce the measured noise transferred to the numerical substructure. The framework is presented and evaluated by virtual HS, and then applied for the hybrid simulations with the full-scale subassemblies.

Online Model Updating (OMU) is applied as part of the hybrid simulation framework to updated modeling parameters of the RBS in the numerical substructure based on the measured experimental response. The OMU takes full advantage of the data being measured during the experiment to update numerical models and by providing more consistency between both. This consistency improves the accuracy of the substructuring scheme and boundary conditions between the experimental and numerical substructures. Importantly, beam fracture was observed in some of the experiments, which prompted a selective update feature since updating all connections to this data would indicate simultaneous fracture of all connections. This conditional feature ensures that the simulation remains physically meaningful to capture the expected propagation of failure.

1.3. Overview of the Dissertation

This work has been divided into 7 chapters with the following content:

Chapter 2 provides additional technical background and literature review of the main subjects covered in this study including hybrid simulation.

Chapter 3 presents an overview of the experimental program, including the tests setup, instrumentation plan, for all quasi-static and hybrid tests performed. A summary of the most important results measured are illustrated herein.

Chapter 4 delves into the detail the mixed displacement-force control methodology developed for hybrid simulation. Numerical simulations are used to illustrate the theory behind the framework. Subsequently, the chapter explores the performance of the method in the context of the hybrid tests carried out to capture column buckling enforcing displacement compatibility.

Chapter 5 describes the online model updating scheme employed in the hybrid simulation to improve the beam numerical model for a better simulation of the column boundary conditions. Additionally, a selective model updating approach is proposed to deal with beam fracture that depends on its relative position respect to the column.

In Chapter 6, a new numerical macro-element is presented, capable of capturing the moment-rotation behavior of deep columns using fiber-based elements, while the axial shortening is simulated through an empirical expression. The macro-element is added to a frame model to assess the expected axial shortening due to the ground motion associated with the maximum considered earthquake.

Finally, Chapter 7 summarizes the main contribution and findings of this study. Conclusions and recommendations for future work is shown herein.

Chapter 2 Background and Literature Review

This chapter presents additional technical background and literature review of the advanced testing methods used in this study. Strategies to load stiff specimens in hybrid simulation, and the use of online model updating in hybrid testing are reviewed. The introductory chapter provides motivation and background on deep and slender columns.

2.1. Hybrid Simulation for Stiff Systems

Hybrid simulation (HS) is an experimental method that combines numerical models and experimental substructures to provide a more reliable representation of the response of complex systems. HS was first proposed about five decades ago [19,20] as a cost-effective alternative to traditional experimental testing methods. In conventional HS, the structural model is divided into numerical and experimental substructures, with displacement commands generated by the numerical model and applied to the physical substructure using actuators. The restoring force response is then measured using sensors and fed back into the numerical model at each integration time-step. This displacement-based approach is compatible with the majority of structural analysis software for time-history analyses that send nodal displacements to numerical elements for state determination and return restoring nodal forces. Moreover, servo-hydraulic actuators and control

systems are typically designed for displacement-control, while force-control can be more challenging [21], especially in the nonlinear response range of test specimens.

Displacement-controlled actuators can be used to impose displacements at most boundary conditions in the physical specimen, with the accuracy reduced for stiff degrees of freedom (DOFs). Due to the small time-step required in the numerical integration, displacement increments for stiff DOFs can be small and below the resolution of the transducer used as feedback for the controller. Small displacement variations including noise will be amplified in the corresponding feedback force due to the high stiffness of the specimen, which may cause convergence issues in the time integration methods especially for a complex numerical model [22].

Stiff DOFs are typically encountered in HS when considering axial forces in columns. In previous HS involving large-scale experimental substructures, axial loads were set as constant with the measured deformations neglected [23–27]. To account for varying axial load on specimens, the force extracted from the numerical model has been applied as a command signal to force-controlled actuators, typically in a manner of open-loop control without displacement feedback to the numerical model. One of the first implementations of this approach was in the HS of a base isolated structure considering bearings with varying the axial load as the experimental substructure [28]. Del Carpio et al. [29] used hydraulic actuators to vary the axial load in columns of a steel moment frame subassembly. Chae et al. [30] added a flexible compliance beam on top of a reinforced concrete column to apply the command axial force through displacement-controlled actuators. More recently, Imanpour et al. [31] tested a steel column using a Multi-Axial Subassemblage Testing (MAST) frame with force control for application of the vertical load on the specimen while also neglecting the measured displacement and compatibility with the numerical substructure.

Alternative solutions to include stiff DOFs in experimental substructures have been proposed. For instance, Whyte and Stojadinovic [32] used a high-precision external transducer to overcome the resolution limitations of displacement-controlled actuators. This approach is directly applicable to displacement-based HS, though it requires the use of specialized instrumentation and can be sensitive to displacement reversals due to backlash and other imperfections in the setup. Wu et al. [33] proposed an equivalent force control method that enables conducting HS in force control mode by substituting the displacement-based time integration scheme with a controller-based algorithm. Notably, other researchers have employed this method to examine large-scale stiff structures [25]. Nevertheless, this force-based method is not readily adaptable to displacement based finite element platforms commonly used in earthquake engineering with access to a vast library of nonlinear elements and other algorithms for more advanced modeling capabilities.

Kim [34] developed a mixed displacement and force control method implemented in the middleware OpenFresco [35]. In this method, forces are imposed on the specimen boundary, while the measured displacement is fed back to the numerical model. The transformation of displacement into forces and vice versa can be done employing an estimation of the experimental tangent stiffness matrix [36] or by using Krylov subspace methods [37] that do not require the tangent stiffness. This framework has been tested on small-scale models without high stiffness and requires further evaluation [38]. Another approach [39] that does not require the experimental tangent stiffness is the staggered coordination scheme. This is an approximate method with constraints at the boundary DOF by using the measured displacement from the previous integration step, adding a delay of one step. The method was successfully implemented in a full-scale specimen to drive the axial DOF in force control using OpenSees as the numerical platform. The authors note that

the approximations employed may not be adequate for systems exhibiting high nonlinearity at the boundary conditions and the computational implementation could be time consuming.

2.2. Model Updating in Hybrid Simulation

The first experimental application of online model updating (OMU) in a HS was carried out by Kwon & Kammula [40] using a weighted average of force vectors from different alternative numerical substructures. Shortly thereafter, Hashemi et al. [41] added a more formal system identification algorithm employing unscented Kalman filter (UKF) [42] to identify the numerical parameters in a fast and efficient manner. Since then, researchers have proposed different improvements in the identification process [43,44] and quantification of the enhancement of the HS fidelity by employing this additional feature [45]. Nevertheless, due to its novelty, most of the experimental applications of HS with OMU have been performed for simplified physical test beds. Recently, Wang et al. [46] applied OMU for a full-scale hybrid test of a steel panel damper specimen by using a multi-axial testing system, demonstrating the feasibility of applying OMU to more realistic complex structures. Al-Subaihawi et al. [43] also implemented OMU in a large-scale real-time hybrid simulation including testing of a nonlinear viscous damper.

2.3. Summary

This study presents a testing program conducted on full-scale cruciform beam-to-column subassemblages subjected to both quasi-static cyclic loading and hybrid simulation. A novel framework was developed to carry out mixed displacement- and force-control hybrid simulation with fully compatible displacements. The approach was numerically validated and then applied to these hybrid tests. An online model updating algorithm was integrated within the hybrid simulation

to enhance the response of numerical beams, thereby improving the column boundary conditions of the experimental substructure.

Chapter 3 Testing Program and Experimental Results

This chapter describes the archetype structures, testing setup, and experimental observations of the full-scale testing program of cruciform beam-to-column subassemblies through quasi-static and hybrid simulation. Quasi-static tests are first performed to assess the cyclic behavior of the subassembly following the standard loading protocols for steel structures. Hybrid simulations using advanced testing methods are also conducted to quantify the structural damage of the frame structure directly under simulated seismic loads using historical records. The hybrid simulations include a full nonlinear numerical model of the prototype frame and applies a novel mixed displacement and force control method described in Chapter 4. Online model updating, described in Chapter 5, was also applied to the hybrid simulation in an effort to obtain reliable results.

3.1. Archetype Structures

Two six-story archetype steel moment frame (SMF) structures were designed to investigate the seismic performance of first-story column with varying slenderness ratios. The building plan view and elevation are depicted in Figure 3.1 for both archetypes. The structural system is designed

for both vertical and lateral loads following provisions outlined in ASCE 7-16 [1] and AISC 341-16 [47] for a site located in San Diego, California, with soil type D. The first story height is 5.5 m (18 ft.), while all other stories have 4.3 m (14 ft.) in height. The seismic-resistant frame in the north-south (N-S) direction examined in this study is comprised of four bays, each measuring 7.9 meters (26 feet) in length.

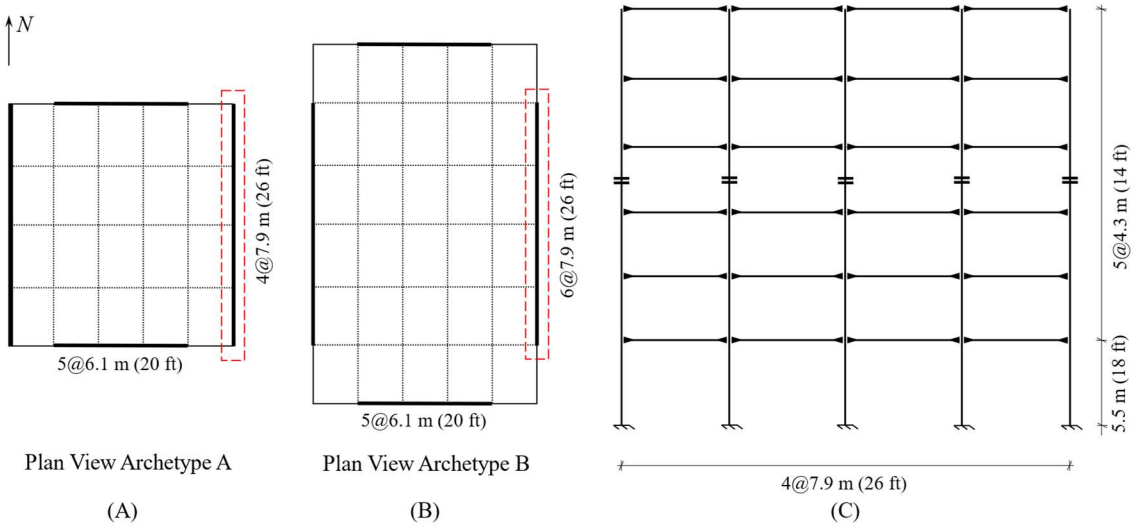

Figure 3.1: Archetype building scheme: (A) Plan view specimen A, (B) Plan view specimen B, (C) Elevation for both archetype buildings A and B.

The use of W24x176 and W24x131 section for the first-story columns with a height of 5.5 m is specifically chosen to facilitate comparisons with the results of member-level tests conducted by Ozkula [4]. The columns were classified as slender based on the slenderness ratio for the flange ($b_f/2t_f$) and web (h/t_w) and their proximity to the seismic compactness limits for highly ductile members as per AISC 341-16 [47], the design code in use at the time of the design of the archetypes. Table 3.1 shows beam and column cross sections and column slenderness. The structural steel components are constructed using A992 Grade 50 steel. Figure 3.2 illustrates the

slenderness requirements for highly ductile members per AISC 341-16 [47]. Details of each test and ID are explained in the following section. The limit required by AISC 341-22 [48] is also indicated for reference, although it was released after the archetypes were designed. Eq. (3.1) shows the slenderness limit equation from AISC 341-16. Note that in the 2016 code version, all columns would qualify as highly ductile members, while for the 2022 version the qualification depends on the axial load. The seismically effective unit weight for the first five floors is 4.5 KPa (94 psf) each, while the roof has a seismically effective weight of 4.3 KPa (90 psf). Based on past studies and experience, first-story columns typically subjected to axial forces ranging from 5% to 20% of their yield capacity [4]. In the design of this building and for the purpose of this experimental program, first-story columns were subjected to an axial force ranging from 20% to 40% of their yield capacity to investigate typical and beyond design cases. This range of loading also allows for a direct comparison with member-level test having similar sections [4,11].

Table 3.1: Summary of member section

Archetypes:	Building A		Building B	
	in×lb	mm×kg	in×lb	mm×kg
Column Section (1st to 3rd floor)	W24×131	W610×195	W24×176	W610×262
Beam Section (1st to 3rd floor)	W27×94	W690×140	W27×129	W690×192
Column Section (4th to roof floor)	W24×117	W610×262	W24×131	W610×195
Beam Section (4th to roof floor)	W27×84	W690×125	W27×94	W690×140
1st Story Column $\lambda_f = b_f/2t_f$	6.7		4.81	
1st Story Column $\lambda_w = h/t_w$	35.6		28.7	

$$2.57\sqrt{\frac{E}{R_yF_y}}(1-1.04C_a) \qquad \text{for } C_a \le 0.114$$

$$0.88\sqrt{\frac{E}{R_yF_y}}(2.68-C_a) \ge 1.57\sqrt{\frac{E}{R_yF_y}} \qquad \text{for } C_a > 0.114 \tag{3.1}$$

$$\text{With} \qquad C_a = \frac{P_u}{\phi_c R_y F_y A_g} \quad \text{(for LRFD)}$$

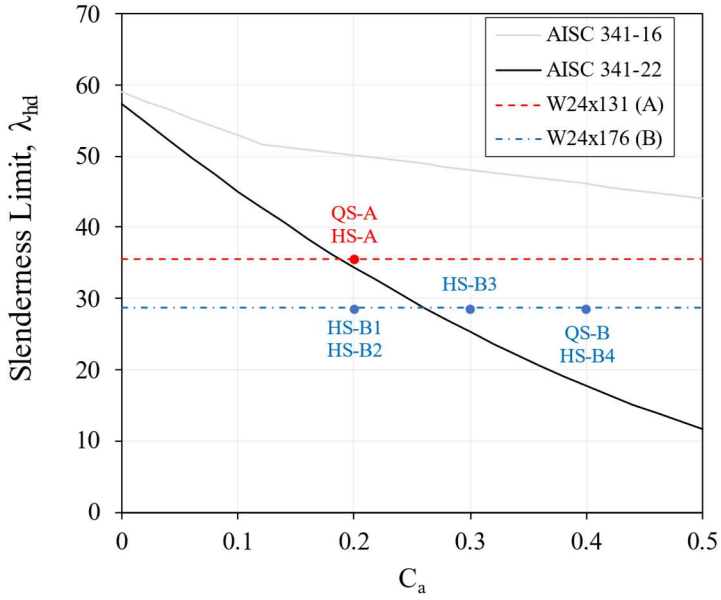

Figure 3.2: AISC Slenderness requirements for highly ductile members and columns tested.

In the building design, the SMF columns were assumed to be fixed at their base and spliced at the mid-height of the fourth story. The beam-column connection considers a doubler plate for the panel zone, continuity plate, and reduced beam sections (RBS) per the guidelines provided by AISC 358-16 [49]. The steel backing between the top beam flange and the column was not removed, and a continuous fillet weld was added on the edge below the CJP weld. The steel backing between the bottom beam flange and the column was removed, and the root pass was back gouged to sound weld metal and back welded with a reinforcing fillet. Bolts in the beam web were used for erection purposes, and a CJP groove weld was provided between the entire length of the beam web and the column flange. Before testing, all CJP groove welds passed the Ultrasonic Welding Test (UT) inspection. Figure 3.3 shows details of the beam-column connection for archetypes A and B.

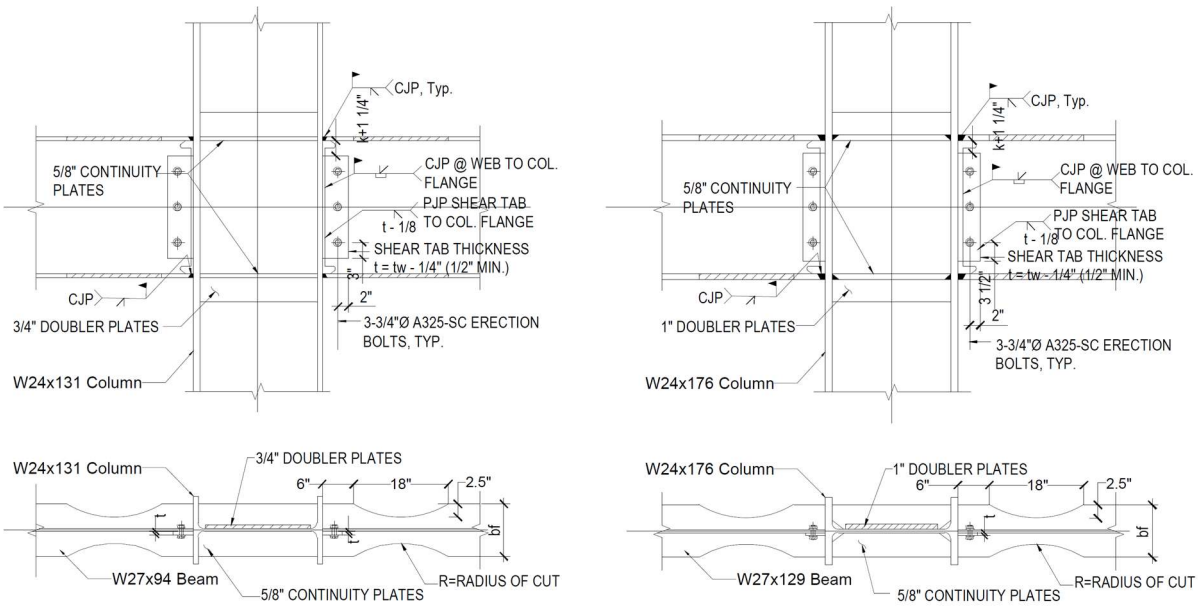

Figure 3.3: Connection detailing for archetypes A and B.

3.2. Experimental Program

3.2.1. Subassembly description

To study the story-level behavior and the interactions between columns, beams, and beam-to-column connections, a cruciform subassemblage was selected for the experimental program. The column height is one and one-half stories, including beams on each side extending half the bay length. External transducers located at the bottom of the panel zone are assigned as the control point for the system loading. The lateral displacement of the specimen is applied by two pin-connected actuators located at the top of the subassembly commanded to match the displacement feedback of the control point. The axial force was applied by four hydraulic jacks on a loading beam attached to the top of the specimen and anchored to the strong floor through steel rods. Pin-connected vertical actuators control the vertical displacement of each beam end, following the vertical movements of the control point below the panel zone. This assumes that any vertical displacement experienced by the column during quasi-static or hybrid tests is similar in

neighboring columns and maintains the presumed point of inflection for the beam at the same height. The cruciform subassembly and the actuator configuration are illustrated in Figure 3.4A.

(A) (B)

Figure 3.4: Experimental setup showing: (A) Specimen and actuator configuration; (B) Lateral bracing.

3.2.2. Experimental setup

The experimental setup required lateral restraints to maintain the in-plane response of the frame. Column flanges at the panel zone and beam top flanges were laterally braced using lubricated horizontal plates supported by diagonal bracing (blue bracing elements of Figure 3.4B) to replicate the bracing provided by the slab. Beams were also braced along the length with additional lateral supports. To prevent subassembly twisting, the abovementioned plates limit the torsion of the column.

The instrumentation deployment is depicted in Figure 3.5. The *Optitrack Motion Capture Systems* (MoCap) was employed to track the absolute displacement of the specimen. LED sensors (not shown) were installed throughout the specimen with a clear line of sight such as the column to enable monitoring of the 3D movement. Strain gauges were utilized along the specimen to capture the beams and column flange response. Inclinometers monitored the absolute rotation at different locations. To better visualize damage in regions of interest, a 10 cm grid was drawn in the column base and RBS zone. Two orthogonal Temposonics linear position sensors (Temposonic III) measured the in-plane displacement of the control point with a resolution of 0.005 mm. Horizontal and vertical displacement components are computed within MTS controller applying kinematic transformations to control the horizontal and vertical actuators. High-sensitivity displacement transducers are employed to monitor the overturning and sliding movement of the column base plate (see Figure 3.6A). Two similar devices are also used to compute the rotation across the RBS as shown in Figure 3.6B, that was used for the online model updating application. The shear distortion of the panel zone is calculated based on the measurement from an X-shape instrument configuration using Pi-shape displacement transducer (Figure 3.6C).

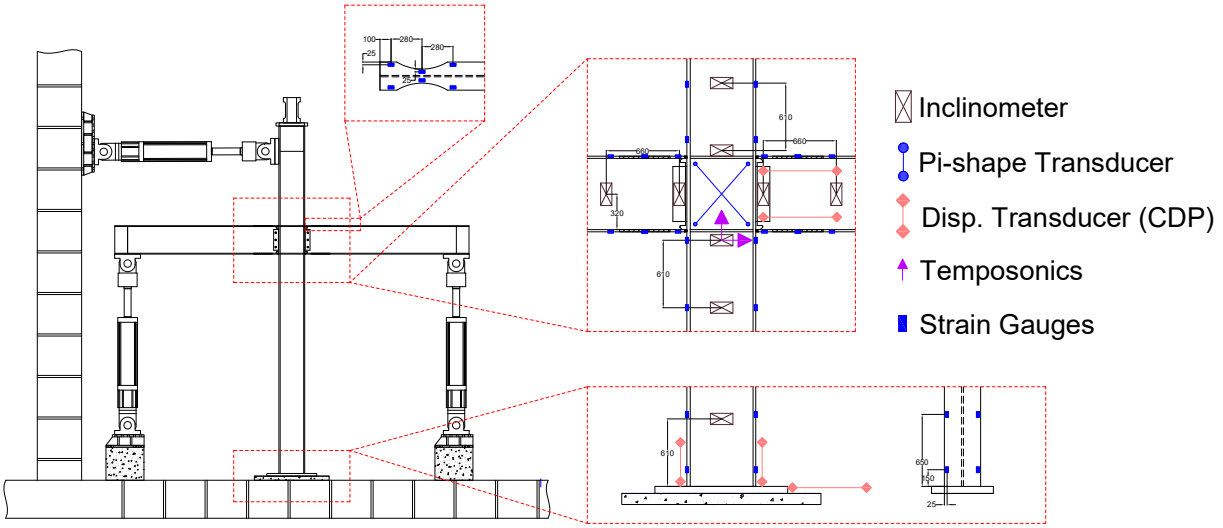

Figure 3.5: Instrumentation setup.

(A) (B) (C)

Figure 3.6: Displacement transducer setup for local measurements of: (A) base plate overturning (red) and sliding (yellow); (B) RBS rotation; (C) panel zone shear distortion.

3.2.3. Testing matrix

Four specimens were tested: two using archetype building A and two using archetype Building B. A quasi-static test and a hybrid simulation was conducted on each archetype. Table 3.2 summarizes the testing matrix, including the sequence and designation Test ID for each test. The axial load for quasi-static tests was constant and based on C_a as per defined as “ratio of required strength to available axial yield strength” per AISC-341-22 [48] and calculated as

$$C_a = \frac{\alpha_s P_r}{R_y F_y A_g} \tag{3.2}$$

where α_s=1 is the LRFD-ASD force level adjustment factor, and $R_y = 1.1$ the ratio of the expected yield stress to the nominal value. For the hybrid tests, the axial load can vary over time due to shifting seismic loads and redistribution of axial forces between columns due to shortening. The column axial force shown in the table for HS corresponds to the gravity load at the start of the seismic excitation. Each test configuration is also compared against the AISC slenderness requirements for highly ductile members, as shown in Figure 3.2. The drifts listed are the maximum achieved for each test.

Table 3.2: Summary of testing matrix

				Ground Motion for HS		Drift (%)	
Test ID	**Type of Test**	**Archetype**	**C_a**	**Level**	**Earthquake**	**Min**	**Max**
QS-A	Quasi-static	A	20%	-	-	-3.3	4.3
HS-A1	Hybrid Simulation	A	20%	Elastic	Kobe (1995)	-0.14	0.15
HS-A2	Hybrid Simulation	A	20%	DBE/MCE	Kobe (1995)/Chi-Chi (1999)	-2.9	2.5
HS-A3	Hybrid Simulation	A	20%	MCE	Northridge (1994)	-2.9	2.0
HS-A4	Hybrid Simulation	A	20%	1.3MCE	Northridge (1994)	-2.7	2.4
QS-B	Quasi-static	B	40%	-	-	-3.0	3.0
HS-B1	Hybrid Simulation	B	20%	Elastic	Kobe (1995)	-0.15	0.14
HS-B2	Hybrid Simulation	B	20%	DBE/MCE	Kobe (1995)/ Northridge (1994)	-5.0	1.5
HS-B3	Hybrid Simulation	B	30%	1.3MCE	Kobe (1995)	-3.1	3.3
HS-B4	Hybrid Simulation	B	40%	1.3MCE	Kobe (1995)	-2.9	2.5

Tensile material testing was conducted for each specimen using coupons extracted after subassembly tests were completed. Figure 3.7 presents a histogram of the measured properties normalized by the corresponding nominal value, and Table 3.3 provides the measured properties of each sample normalized by the nominal value.

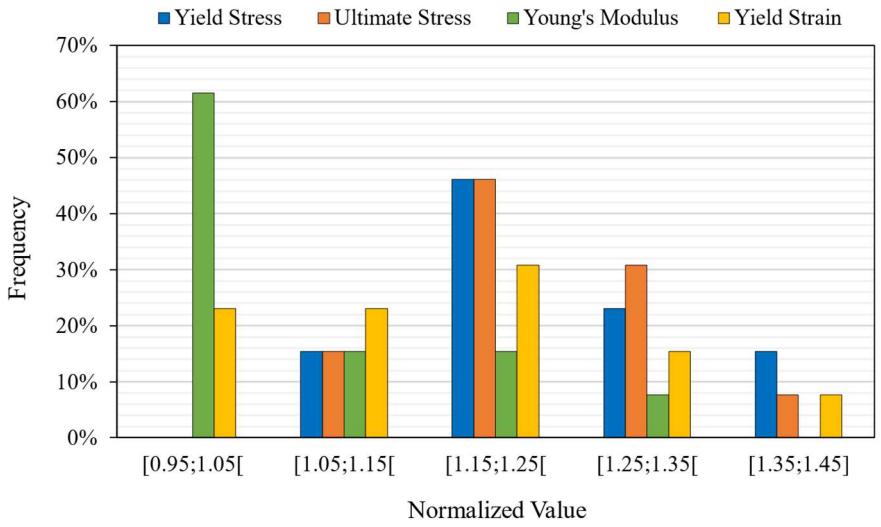

Figure 3.7: Histogram of normalized properties measured from tensile coupon tests.

Table 3.3: Coupon testing results of each member normalized by nominal value

Label	Location	Yield Stress (345 MPa)	Ultimate Stress (450 Mpa)	Young's Modulus (200 GPa)	Yield Strain (1.725 ‰)	Fracture Elongation (%)
Q-A	Column Web	-	-	-	-	-
	Column Flange	1.16	1.20	1.02	1.15	29.6
	Beam Web	1.33	1.28	1.00	1.33	19.6
	Beam Flange	1.16	1.15	0.97	1.20	27.2
HS-A	Column Web	1.35	1.35	1.19	1.13	24.0
	Column Flange	1.36	1.41	1.32	1.04	28.8
	Beam Web	1.37	1.32	1.01	1.36	19.8
	Beam Flange	1.14	1.15	1.05	1.09	27.4
Q-B	Column Web	1.28	1.26	1.01	1.27	25.3
	Column Flange	1.17	1.24	0.96	1.22	29.2
	Beam Web	-	-	-	-	-
	Beam Flange	-	-	-	-	-
HS-B	Column Web	1.19	1.24	1.17	1.02	24.1
	Column Flange	1.20	1.23	1.02	1.18	28.0
	Beam Web	1.19	1.16	1.00	1.19	24.1
	Beam Flange	1.11	1.18	1.13	0.98	28.6
Average (X)		1.23	1.24	1.06	1.16	25.8
SD (S)		0.0932	0.0792	0.105	0.115	3.37
X-S		1.14	1.17	0.96	1.19	22.5
X+S		1.33	1.32	1.17	1.13	29.2

The symmetric protocol specified by AISC 360-16 [50] was employed for quasi-static tests up to a 5% drift ratio, which was the maximum displacement allowed by the setup. However, none of the quasi-static tests reached that level since the specimens suffered significant damage before such drift.

Four hybrid tests were conducted for each selected specimen using different intensities of ground motions as shown in Table 3.2. The testing plan consisted of first conducting a low-level test to check all the instrumentation and hardware/software connectivity maintaining the specimen in the linear-elastic range. Then, a sequence of a design-basis earthquake (DBE) followed by a maximum-considered earthquake (MCE) ground motion was preprogramed to account for the cumulative damage and residuals within the numerical and experimental substructure. Following this sequence, both specimens remained with sufficient capacity and additional HS were conducted to obtain more experimental data on cumulative damage. For those tests, the simulation had to be reset, and did not maintain the residual state of the numerical substructure.

3.3. Hybrid Simulation Setup

3.3.1. Numerical substructure

The hybrid simulation comprised the complete 5-bay 6-story frame and associated weight and mass. The numerical model was developed utilizing the OpenSees platform [17]. Figure 3.8 illustrates the modeling scheme for the beam-to-column connections. Columns are assumed to have fixed connections at the base and were represented using distributed plasticity elements employing a displacement-based formulation with 4 Gauss-Lobatto points. The change in sectional properties due to column splices were considered by using different sections for the upper and lower portion. The panel zone flexibility was simulated using the parallelogram approach with a

rotational spring in one of the corners [51] using the trilinear shear force-shear distortion proposed by Krawinkler et al [52].

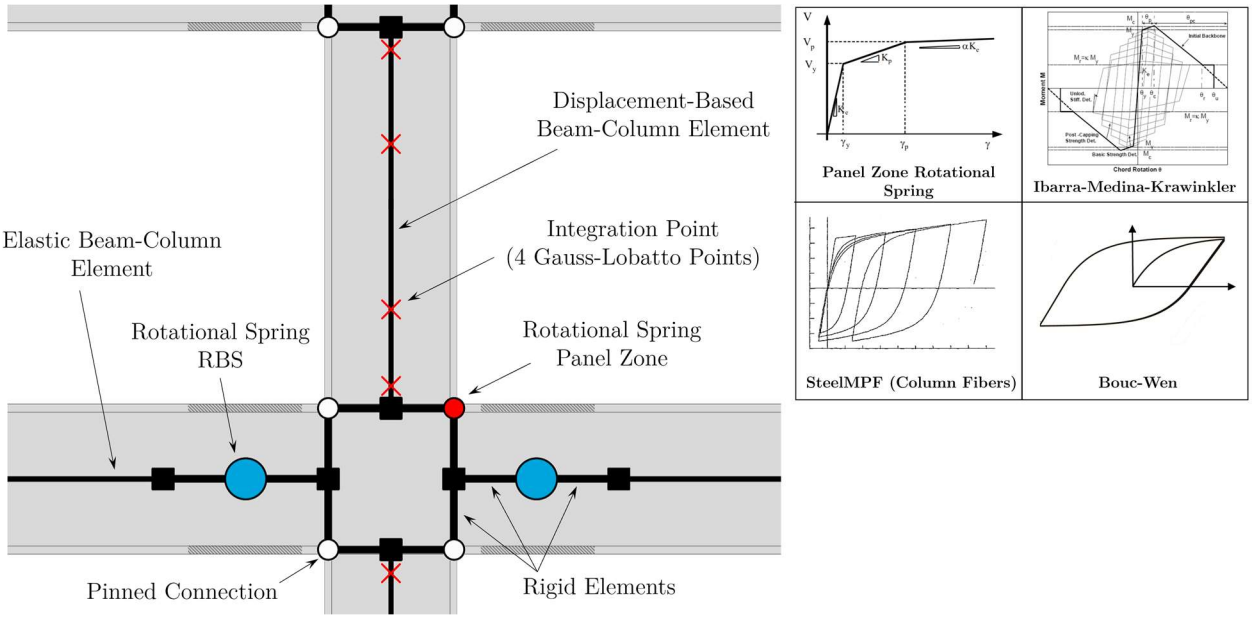

Figure 3.8: Beam-to-column connection numerical model.

Beams were modeled using an elastic beam-column element for the middle section, with rigid offsets and a lumped plasticity rotational spring at each end. Starting from the second story and above, the response of the RBS was simulated using the Ibarra-Medina-Krawinkler (IMK) model [53], with properties initially defined based on the recommendations of Lignos and Krawinkler [54], and then adjusted based on the quasi-static results. For the RBS hinges located on the first level, a Bouc-Wen model was used implement as part of the Online Model Updating (OMU) scheme that updated the numerical hinge properties based on the measured data during the HS. More details about OMU can be found in Sepulveda et al. [55] and Chapter 5. Rayleigh damping assigned as 2.5% of critical was added as inherent damping anchored to the first and third elastic modes. A P-Delta transformation was incorporated into column elements. A leaning column

was added alongside the moment frame to account for the contribution of the P-Delta effect of the gravity frame and experimental column.

3.3.2. Substructuring and control strategy

Numerical simulations conducted on the complete frame system showed negligible differences in loads and deformations among the three interior columns [56]. Considering the cruciform subassemblage and test setup, the physical substructure was defined to represent the behavior of the three interior first story columns, while the exterior columns were simulated in the numerical substructure. Although the exterior columns may also experience axial shortening due to buckling, previous isolated column testing has demonstrated that the axial load variation resulting from overturning delays local buckling initiation and significantly reduces axial shortening when compared to interior columns with more constant loading [4,57]. In these simulations, the axial shortening of the exterior columns was solely attributed to material nonlinearity through the fiber-based column element.

The experimental subassembly has hinge connections at the ends of beam and columns following typical practice of assuming inflection points at the midspan of beams and column. To better account for these boundary conditions in the hybrid simulation, an overlapping substructuring method [58] is applied. A diagram of the substructuring approach together with the hybrid loop and online model updating loop are exhibited in Figure 3.9. noting the overlap between the experimental second story and the numerical substructure. The two paired horizontal actuators on top of the subassembly apply the horizontal displacement at the control point as commanded by the numerical model. The axial load command computed by the numerical substructure was applied using the force-controlled oil jacks on top of the specimen. The two vertical actuators

maintain the end of the beams at the same vertical position of the panel zone following any shortening of the column. Further details regarding the control strategy can be found in Sepulveda et al. [59] and Chapter 4.

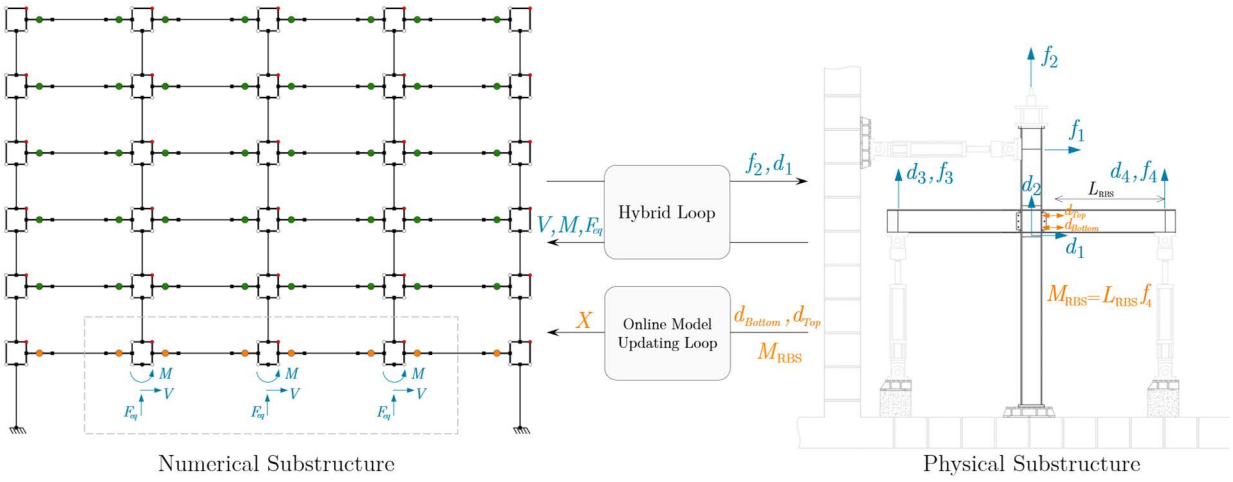

Figure 3.9: Substructuring scheme.

3.3.3. Hardware/Software architecture

HS are conducted using detailed nonlinear numerical models in OpenSees integrated in the hybrid control loop as shown in Figure 3.9. In the experimental setup, the horizontal first-story displacement (d_1) is transmitted from the numerical substructure to the horizontal actuator controller. The axial load command is obtained from a numerical load cell element placed at mid-height of the middle second-story column with a length equal to the depth of the section. The calculation of the force from the deformations is carried out in the middleware OpenFresco.

OpenSees [17] and OpenFresco [18,35] run in the same host PC that transfers signals via TCP/IP to a Simulink model running on a real-time digital signal processor (Speedgoat Target PC). The real-time processor runs a predictor-corrector algorithm[60] to generate a smooth continuous command signal to the actuators. The Target PC also scales the simulation time scale

to 200 times slower than real-time, determined by the maximal loading rate of the actuators. The commanded signals are sent to the MTS controller via shared-memory SCRAMNet GT200. Two orthogonal Temposonics linear position sensors (Temposonic III) measure the in-plane displacement of the control point with a resolution of 0.005 mm. Horizontal and vertical displacement components are computed within MTS controller applying kinematic transformations to control horizontal and vertical actuators. The feedback signals are returned in a reverse fashion with a 7-points moving average filter in the Simulink model further reducing measurement noise.

The feedback signals are received by OpenFresco in the host PC, which first applies kinematic transformations to convert actuator DOFs into numerical model DOFs. Vertical displacement d_2^{msr} is also transferred through the middleware to OpenSees to execute the controller-based displacement-to-force transformation. Note that this transformation can be alternatively performed at the middleware or in the real-time processor. Finally, feedback forces are received at the bottom node of the first-story panel zone. Figure 3.10 also includes signals related to the online model updating feature implemented on these HS. Note that when virtual hybrid simulation is executed, all the components beyond OpenFresco are replaced by another OpenSees instance running within the same host computer (see Figure 3.10b).

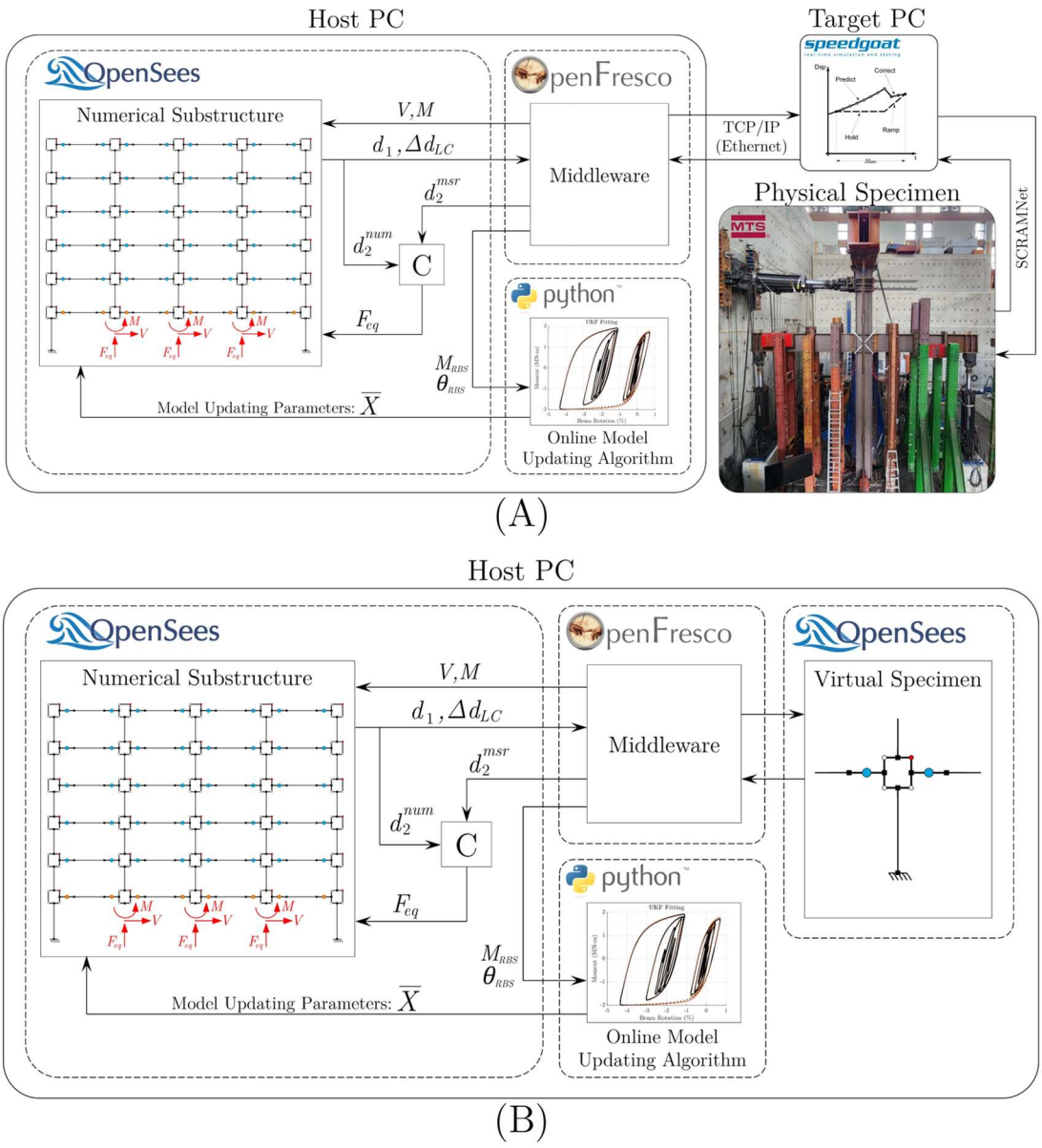

Figure 3.10: Hardware architecture for: a) Hybrid Simulation; b) Virtual Hybrid Simulation.

3.4. Experimental Results: Specimen A

3.4.1. Test Q-A

Carrying out the experimental program at this scale and size came with significant challenges in terms of the setup and fully restraining out of plane motion. The setup was first

developed for box columns having large out of plane stiffness [61]. Accounting for the column slenderness in the weak axis, it was not practical to apply direct restraints at the top of specimen considering the elevation, scale and location of the setup. The horizontal actuators were initially placed in a V-shape configuration to control the out-of-plane displacement of the specimen at the top. After the first cycle of +4.3% drift, the severity of the column and RBS local buckling increased, producing column twisting. The testing was stopped before the first peak at -4.3% due to excessive specimen twisting. Figure 3.11 depicts the drift ratio measured during the test. For the following tests, the out-of-plane deformation was successfully controlled by reinforcing the lateral bracing at the beam elevation, and the column twisting was controlled through a parallel configuration for the horizontal actuators, both working in displacement control mode. The torsional constraint was necessary for laboratory safety. It should also be noted that in the quasi-static test of specimen A, the applied drift ratio slightly exceeds AISC 360-16 values because the control point was positioned below the reference height for the actuator-imposed deformation. This was corrected for the following tests.

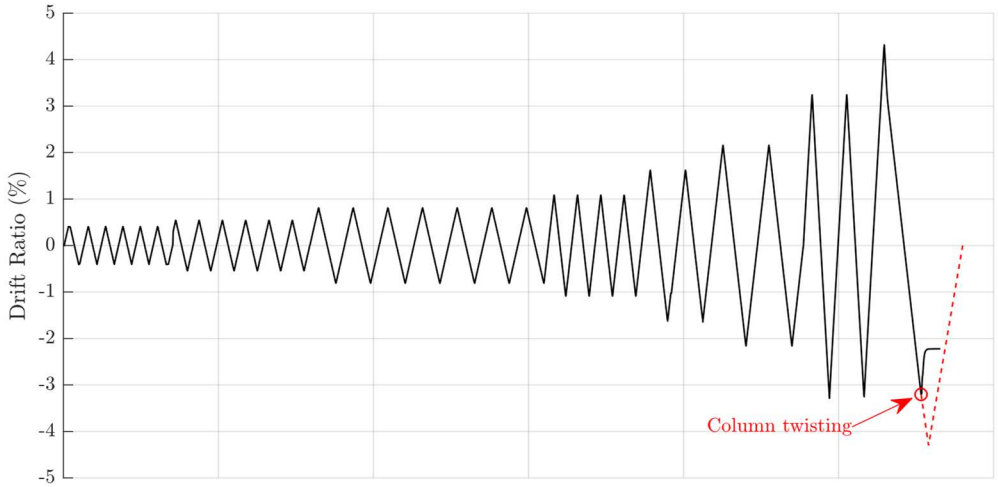

Figure 3.11: Loading protocol for Q-A test.

3.4.2. Test HS-A

The experimental substructure was replaced with an identical Specimen A and subjected to four consecutive hybrid simulations. HS-A1 was an elastic level simulation used to verify the test setup. HS-A2 was composed of a sequence of DBE and MCE ground motions. The test was stopped prior to reaching the maximum response of the MCE motion due to a fracture the bottom flange weld of the south beam and excessive tilting of the loading beam on top of the specimen. The fracture was repaired, and the specimen was recentered to minimize residual deformations and forces on the specimen and the beam. The testing was continued with HS-3, a different MCE level motion, in order to further evaluate the column behavior. An additional test HS-A4 was conducted to evaluate the remaining capacity of the specimen. The numerical substructure was restarted for this test losing the residual state of the numerical model and actuator forces were manually brought to zero maintaining the horizontal offset. The ground motion was scaled up to 1.3 times MCE to maximize the specimen drift. The test was stopped before reaching the maximum response because there was notable out of plate rotation at the top of the column including the loading beam, both beams experienced weld fracture at the bottom flanges, and the column yielded and twisted but showed no significant buckling. The applied drift ratio history for the first story and maximum drift for all the stories can be observed in Figure 3.12.

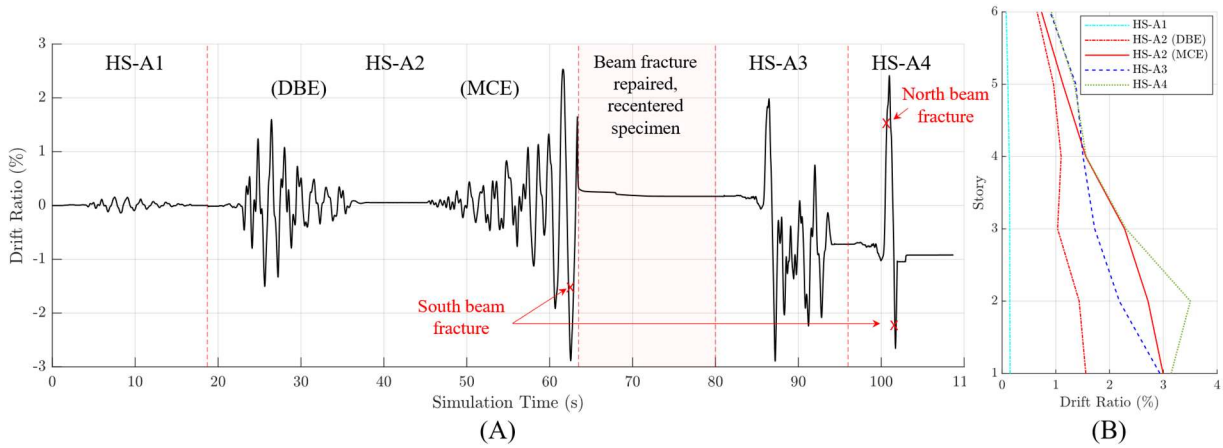

Figure 3.12: Response from HS-A tests: (A) First story drift; (B) Maximum story drift (numerical substructure).

3.4.3. Column response

The column response in terms of moment at the base vs. story drift is shown in Figure 3.13 for both the QS and HS tests. Moment at the base is computed based on Eq. (3.3)

$$M_{base} = f_1\left(H_1 + \frac{H_2}{2}\right) + f_3\frac{L}{2} - f_4\frac{L}{2} \tag{3.3}$$

where f_1 to f_4 are the actuator forces shown in Figure 3.9, H_1 and H_2 are the story height of first and second floor, respectively, and L is the bay length. Note that f_2 (axial force) is not included in the equation since the steel rods followed the column inclination. Nonlinear geometry due to actuator rigid body motion was assumed negligeble for this purpose and was not considered herein. The column showed essentially linear behavior until 1.0% drift ratio in the QS-A test and steel yielding after that. At the first cycle of 3.25% drift, column web buckling was identified by visual inspection (Figure 3.14A). Antisymmetric local buckling was noticed for the following cycles 2. The severity of buckling increased rapidly during the 3.25% cycles, showing stregth

degradation in the moment-drift response (Figure 3.13A). The final state of the column after one 4.3% cycle is shown in Figure 3.14B and Figure 3.14C.

During the hybrid tests, the severity of the damage was limited compared to the quasi-static tests. Although the maximum drift ratio achieved in the HS was only slightly smaller, no degradation is observed in the moment response, for drift ratios up to 3% (Figure 3.13B). Limited column web buckling can be observed only at the end of the last HS, as illustrated in Figure 3.15A. However, despite the reinforced lateral bracing, the second story of the column twisted with RBS buckling (Figure 3.15B). The observed strength degradation indicates the notably more intense demands of the QS test compared to the HS.

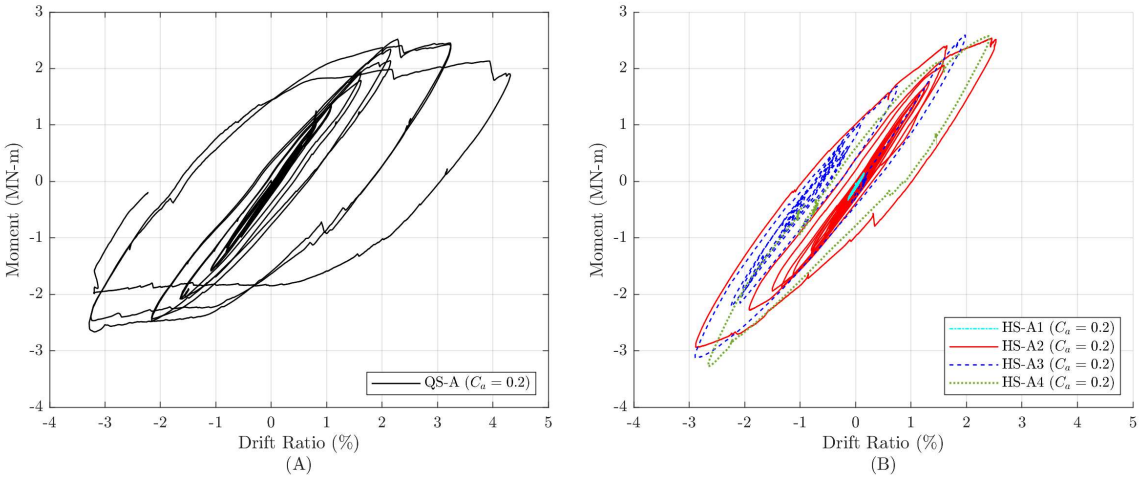

Figure 3.13: Column base moment vs. drift ratio: (A) QS-A; (B) HS-A.

(A) (B) (C)

Figure 3.14: Photos of column base for QS-A: (A) After first 3.25% drift; (B) after 4.3% drift; (C) after 4.3% drift (lateral view).

(A) (B)

Figure 3.15: Column state at the end of HS-A4: (A) Column base; (B) Second story twisting.

The behavior of the column is further evaluated through localized strain gauge measurements. Figure 3.16 shows the strain measurement at an elevation of 650 mm from the base plate normalized by the nominal yield strain. Strains measured on the front and back sides of a flange are displayed on the X and Y axes, respectively. If the column deforms symmetrically, the strains are equal and align at 45º. A deviation from the 45º line could indicate unsymmetrical

deformations caused by buckling. As can be seen, for QS-A (Figure 3.16A), there is a nonsymmetric pattern after reaching 3.25% drift, in agreement with previous observations. For the hybrid tests (Figure 3.16B), the pattern deviates slightly from the 45º line. More symmetric deformations could also result from the lateral bracing improvement applied after QS-A to limit column twisting.

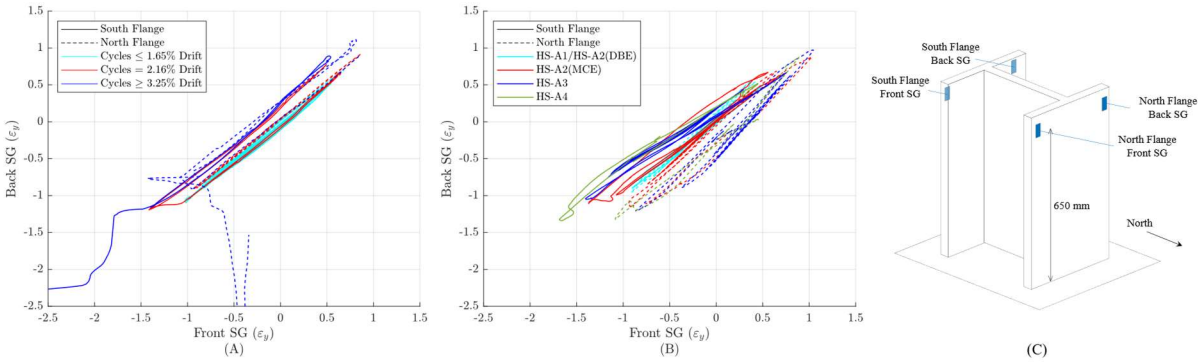

Figure 3.16: Column flange strains: (A) QS-A; (B) HS-A; (C) Strain gauge location.

Axial shortening (Δ_{axial}) was monitored during all tests using the measurement at the control point. The measured values for both QS-A and HS-A are plotted in Figure 3.17 as a function of drift. The gravity load resulted in Δ_{axial} of around 2.5 mm. For QS-A the specimen experienced additional 2.5 mm in the last drift cycle of 2.16%. As the test progressed, column buckling became evident and Δ_{axial} continued to increase to around 26 mm by the last cycle of 3.25%, and 53 mm by the end of the test.

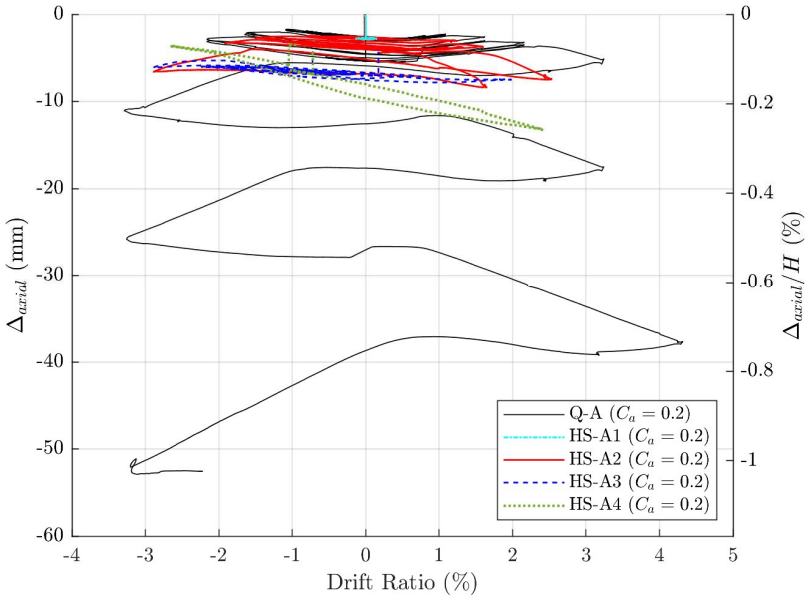

Figure 3.17: Axial shortening versus column drift ratio for Q-A and HS-A.

For the hybrid test, gravity loads resulted in similar Δ_{axial} of 2.5 mm, followed by an additional 2.0 mm after the DBE ground motion level of HS-A2 that applied peaks of -1.9%/1.6% drift. Under the MCE ground motion, the specimen was subjected to drift ratios as high as -2.9%/2.5%, and experienced a total Δ_{axial} of 8.4 mm. In the subsequent tests HS-A3 and HS-A4, vertical oscillations were observed to be correlated with the horizontal deformation of the specimen. This behavior is likely attributable to the tilting of the loading beam, which may have affected the displacement measurements at the control point. Notably, these last tests did not lead to substantial increase in Δ_{axial}. For both QS-A and HS-A tests, axial shortening observed up to around 2% drift can be attributed to steel yielding, as suggested by the strain profiles and visual inspections that did not indicate column buckling [15]. After this point, the QS test induced column buckling and significant Δ_{axial} with drift ratio of 3.25% and one cycle of 4.3%. On the other hand, HS did not produce a substantive increment in Δ_{axial}, even up to 2.9% drift that is relatively close to the 3.25% drift achieved in QS-A. This difference can be attributed to the dependency between

buckling-induced axial shortening and the cumulative damage induced to the column as suggested by previous studies [62–64].

3.4.4. Beam response

The RBS response is presented in terms of the moment at the column face versus the measured local rotation across the RBS section with the setup shown in Figure 3.6B. Figure 3.18 plots the north beam response for both QS and HS. There is limited strength degradation in all the experiments, being observable at the end of the tests. Unlike the column response, the RBS response exhibits more similarities when comparing quasi-static and hybrid tests. A sudden drop in the beam strength of around 40% is observed at the end of HS-A4 due to the bottom flange fracture mentioned earlier.

Strain gauges were attached at both beam flanges along the RBS zone (Figure 3.19C). Figure 3.19A and Figure 3.19B presents the measurements at a distance of 660 mm away from the column face for both QS-A and HS-A. Similar to the column response, the relation deviates from the 45º line at 3.3% drift during QS-A. During the MCE level ground motion of HS-A, the pattern also deviates from the 45º pattern, but remains within a limited zone.

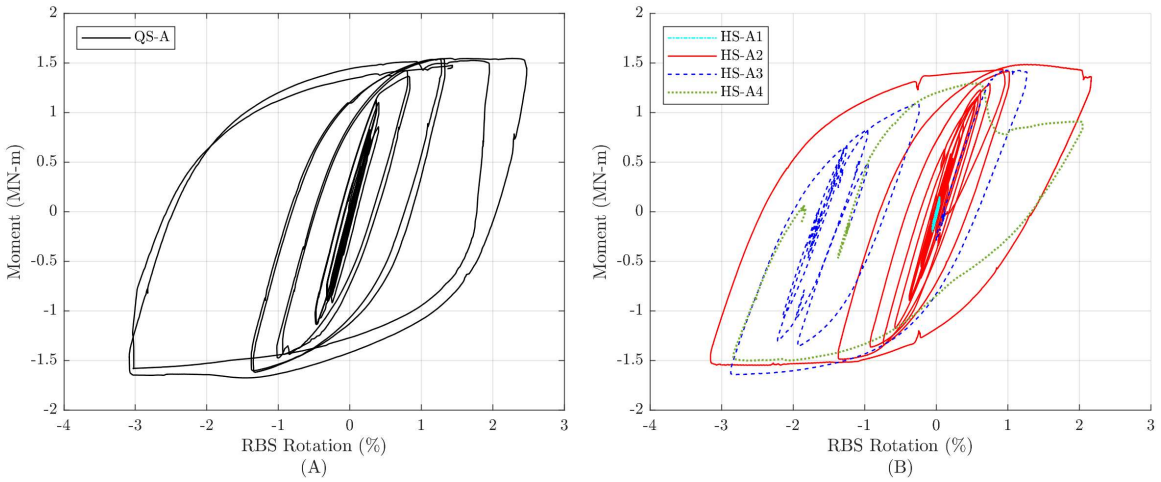

Figure 3.18: RBS local moment-rotation response: (A) QS-A; (B) HS-A.

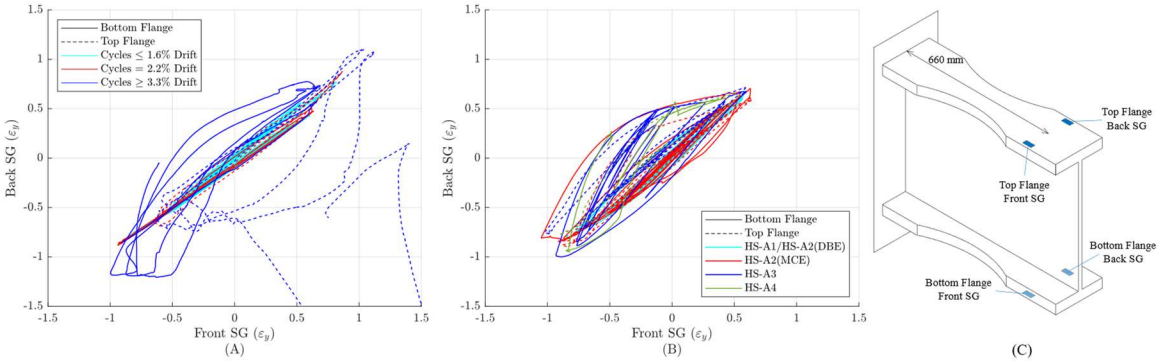

Figure 3.19: Beam flange strains: (A) QS-A; (B) HS-A; (C) Strain gauge location.

Figure 3.20A and Figure 3.20C display beam local buckling and lateral tortional buckling, observed at the end of QS-A. Figure 3.20B depicts ductile tearing at the reduced section of the south RBS. After QS-A, more cycles were imposed on this specimen to check hardware/software connections in preparation for HS-A (not shown here). During those trials, ductile tearing increased and finally led to beam fracture.

While the column behavior may have differed, beam damage in HS-A was similar to that in QS-A. Buckling wave lengths were larger for QS, but with comparable moment-rotation response. Figure 3.21 shows the progression of beam local buckling from HS-A2 up to HS-B4.

Figure 3.21C also shows the bottom flange weld fracture during HS-4. Lateral buckling increased its severity from HS-A2 to HS-A4 (see Figure 3.22).

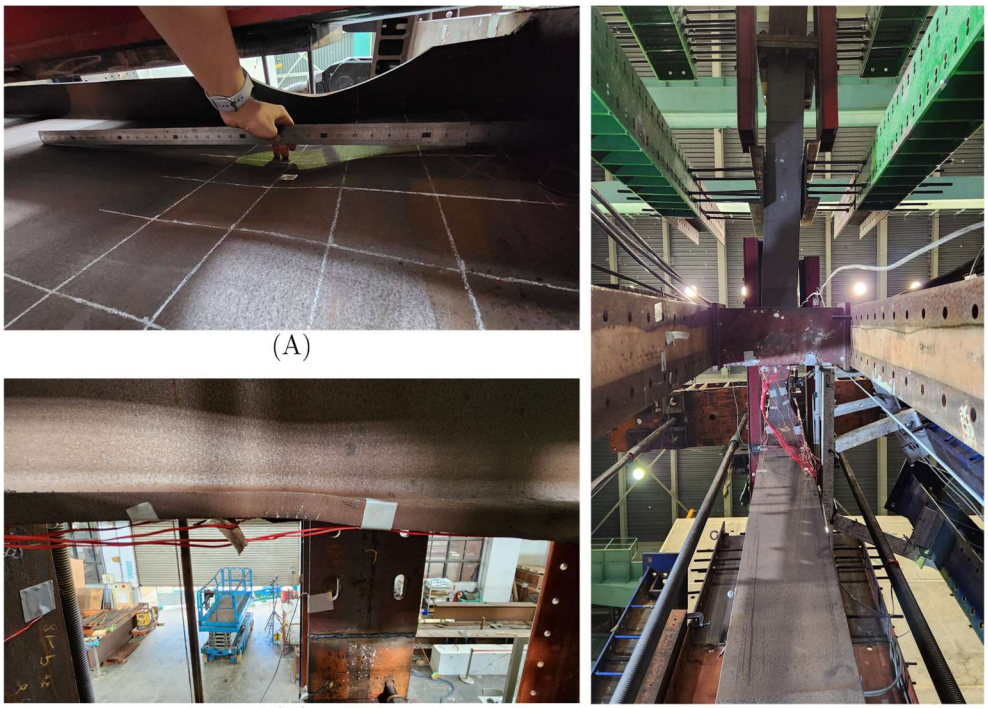

(A) (B) (C)

Figure 3.20: Final state after Q-A: (A) RBS local buckling; (B) Ductile tears at the left RBS; (C) Lateral buckling.

(A) (B) (C)

Figure 3.21: Beam local buckling: (A) HS-A2; (B) HS-A3; (C) HS-A4

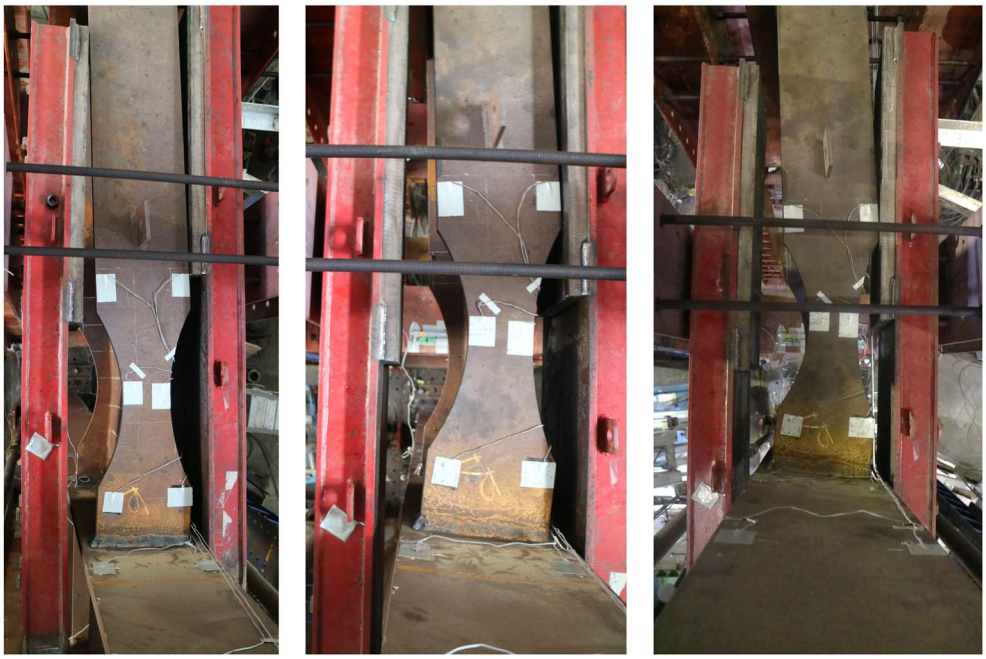

(A) (B) (C)

Figure 3.22: Beam lateral buckling: (A) HS-A2; (B) HS-A3; (C) HS-A4

3.5. Experimental Results: Specimen B

3.5.1. Test Q-B

Two specimens representative of archetype B were also subjected to a QS and HS loading sequence. Test QS-B was initially conducted using the same axial load ratio as QS-A (C_a=20%). When the specimen reached the first peak drift of -2%, bottom beam flange weld unexpectedly fractured in the south beam that ended the test. With no significant damage to the column, new beams were installed using improved welding details. The loading protocol was restarted from the start and the axial load was increased up to C_a=40% to examine a more critical scenario. At the second 3% drift cycle, the column buckled globally and experienced excessive out-of-plane deformation and tilting. Only the results from the repaired specimen are presented here. Figure 3.23 shows the drift ratio measured during Q-B.

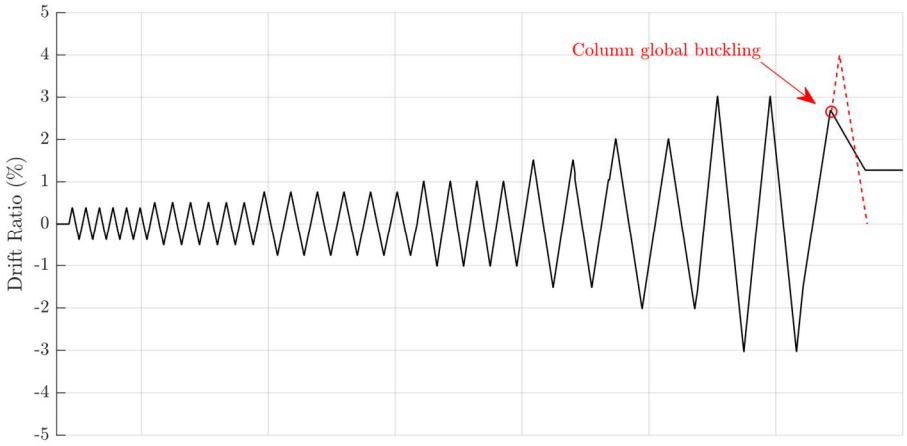

Figure 3.23: Loading protocol for Q-B test

3.5.2. Test HS-B

The second specimen based on archetype B was subjected to a sequence of four ground motions starting with C_a=20%, following a similar approach to HS-A. Figure 3.24 presents the specimen drift ratio history for the first story and maximum drift for all the stories per test. HS-B1 was a low-level test for verification of the setup. HS-B2 applied a sequence of DBE and MCE motions resulting in a peak -5% drift that was near the physical limit of the experimental setup. After HS-B2, there was significant residual drift and the specimen was recentered to minimize displacement and force offsets, with limited buckling at the beams and no significant buckling in the column.

With the specimen already having significant damage, HS-B3 and HS-B were conducted to gain more insight and data on the residual capacity of the specimen following the previous loading cycles. For HS-B3, the gravity load was increased to apply column axial forces equivalent to C_a=30% for the experimental substructure. The MCE ground motion was scaled by an additional factor of 1.3 to achieve a larger positive drift in the specimen but within the setup constraints. By this stage, the column had notable web buckling at the base and ended with near zero residual

deformation. For HS-B4, the axial load was increased to C_a=40%, to induce more damage in the column while limiting drifts that can lead to increased out-of-plane movement of the specimen. The numerical substructure for archetype A was used for HS-B4 as it provided a more desirable distribution of deformations in the upper stories to better align within the limits of the test setup. By this point, the selection of the numerical model was not considered critical in terms of the expected global response since the specimen was damaged and the numerical model had to be reset and starting from an undamaged state.

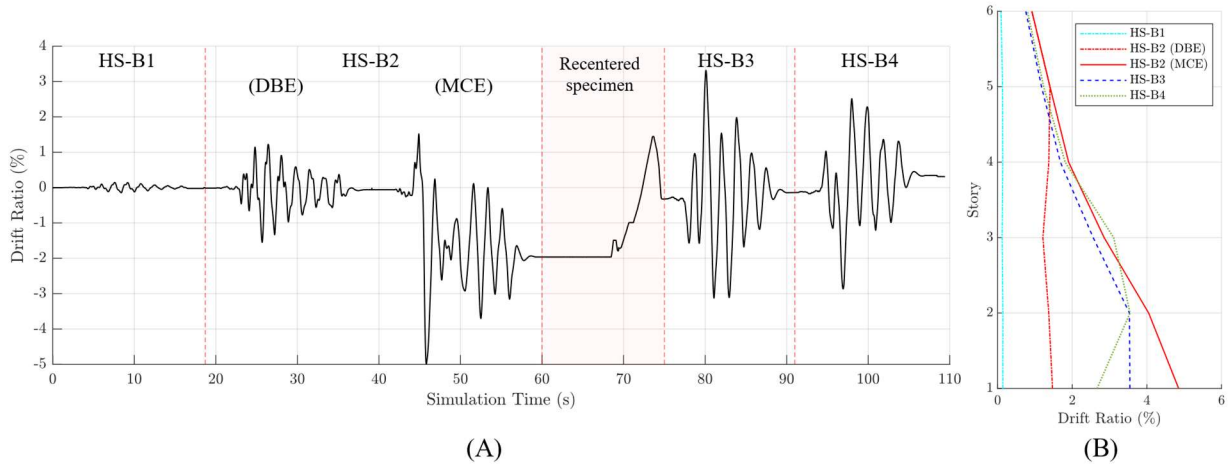

(A) (B)

Figure 3.24: Overall response from HS-B test sequence: (A) First story drift ratio; (B) Maximum story drift ratio (numerical substructure).

3.5.3. Column Response

Figure 3.25 plots the total measured response at the column base for each specimen. QS-B with C_a=40% shows a more well-defined yield point and significant strength degradation especially after the first cycle at 3% drift. HS-B1 was the elastic hybrid test employed to verify hardware/software connections. HS-B2 produced a -5% drift ratio, the largest peak deformation among all the tests conducted in this study. This peak was achieved with less cycles and lower axial load compared to QS-B, and exhibits a smoother transition between the elastic and inelastic range with a more gradual change in stiffness. HS-B3 applied a postive peak in the opposiste

direction with no evident strenght degradation between the two peaks of -3%. The continued loading in HS-B4 exhibits a closer behavior with the QS-B envelope in terms of strenght degradation with both being loaded with the same axial load. However, the level of strength degradation is more substantial in QS-B test.

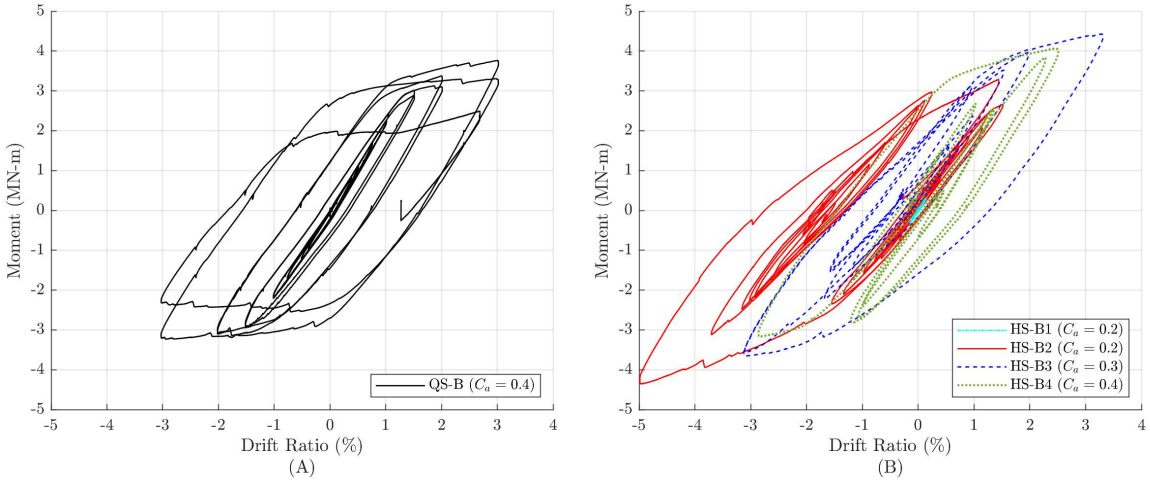

Figure 3.25: Column base moment vs. drift ratio for Q-B and HS-B tests

Figure 3.26 and Figure 3.27 show photos of the column state for QS-B and HS-B, respectively. After reaching a 2% drift ratio during QS-B, the first evidence of local buckling in the web was visually detected at the column base (Figure 3.26A). When the specimen was subjected to the first cycle at 3% drift, the severity of the buckling increased, exhibiting antisymmetric local buckling with a second local buckling wave coupled with lateral-torsional buckling and out-of-plane global buckling, called coupled buckling [2]. Figure 3.26B and Figure 3.26C show the column coupled buckling at the end of QS-B. Although column buckling was more visually evident at 3% lateral deformation, drifting in the strain gauge measurements suggests it was triggered at 2% in QS-B (Figure 3.28A).

(A) (B) (C)

Figure 3.26: Column base for QS-B: (A) After first 2% drift; (B) at the end of the test; (C) lateral view at the end of the test.

While HS-B2 produced the largest lateral deformation in the specimen, it did not produce observable buckling (Figure 3.27A). HS-B3 with increased axial load initiated the local buckling at the column base without visible global buckling. HS-B4 increased the severity of the local buckling with no observable global buckling, though the loading beam began to tilt at the end of HS-B4. After disassembling the specimen, an apparent out-of-plane bending can be observed (Figure 3.27D), suggesting out-of-plane global buckling also showed up during the hybrid tests. The strain distribution shows a limited deviation from the 45º line indicating more symmetric behavior for HS-B2 (Figure 3.28B) and deviations indicating buckling during HS-B3.

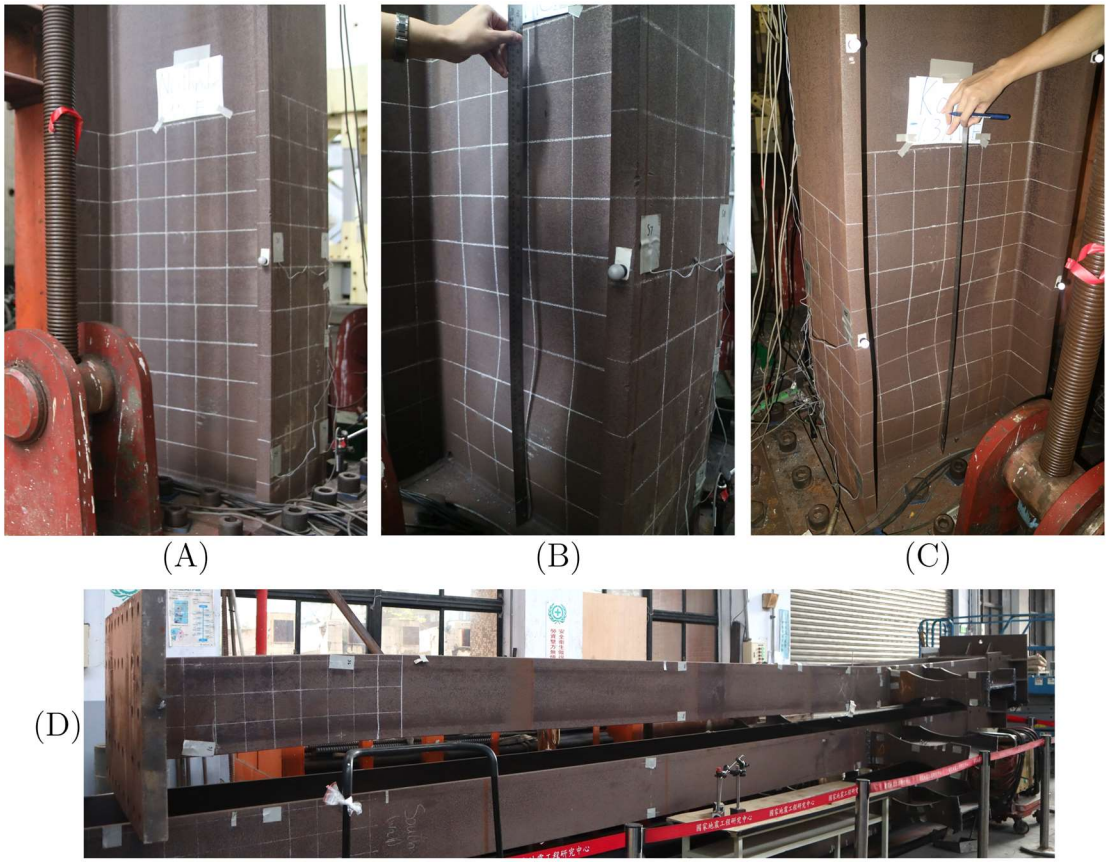

Figure 3.27: Column base at the end of HS-B tests: (A) HS-B2; (B) HS-B3; (C) HS-B4; (D) disassembled specimen.

A comparison of both tests shows that there was more damage during QS-B compared to HS-B. A direct comparison is not as straightforward for archetype A since axial load of QS-B was higher than HS-B for most of the testing and a larger peak drift was achieved during HS-B. Nonetheless, QS-B and HS-B4 employed the same axial load and similar maximum lateral drift, exhibiting different final damage state. This indicates that structural damage is not only related to the maximum deformation but also to cumulative damage.

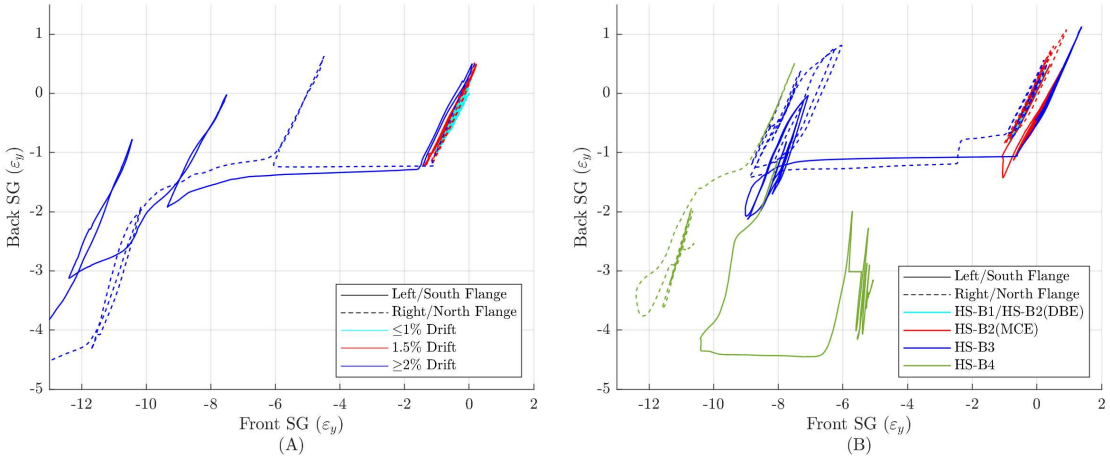

Figure 3.28: Column flange strains at 65 cm from the base plate: (A) Q-B; (B) HS-B.

Axial shortening for QS-B and HS-B is compared in Figure 3.29 Based on visual inspection and strain profile data mentioned above, buckling was not observed for drift ratios up to 1.5% for test QS-B. At that stage, axial shortening was composed of 5.3 mm due to the gravity loads, plus 3 mm after the last 1.5% drift cycle, completing a total Δ_{axial} = 8.3 mm. Upon concluding this test, Δ_{axial} = 94 mm for a maximum drift ratio of 3%.

HS-B2 test induced an initial gravity displacement of 3.6 mm in the specimen. Despite the large drift ratio produced by this test, the total Δ_{axial} reached about 8.2 mm, mainly due to steel yielding based on visual inspection and strain measurements. HS-B3 tests induced column buckling and a total shortening of 18.5 mm. Lastly, HS-B4 induced -2.9%/2.5% peak drift ratios and an equivalent axial load to QS-B and a total Δ_{axial} of 38.4 mm at the end of the test.

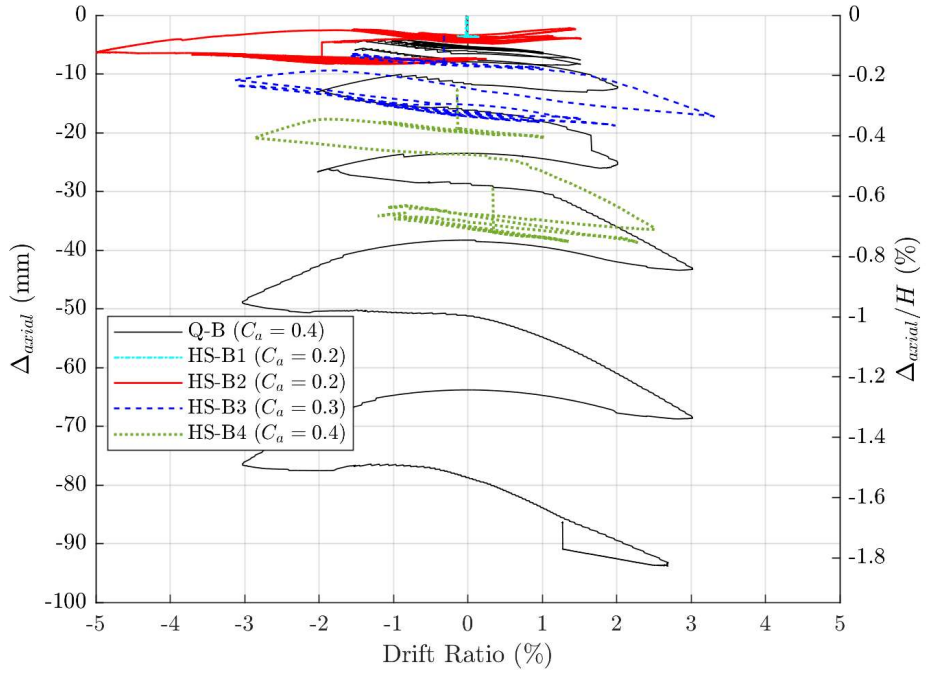

Figure 3.29: Axial shortening versus column drift ratio for QS-B and HS-B.

3.5.4. Beam response

The RBS response was also monitored during testing of archetype B. During the QS-B test, RBS exhibits smaller rotations and limited strenght degradation (Figure 3.30A). This is consistent with the visual observatios of limited local buckling as shown in Figure 3.31B. Unlike specimen A, no lateral buckling was observed during QS protocol (Figure 3.31A). This might be attributable to a combination of higher column torsional stiffness and out-of-plane beam stiffness. The largest RBS rotation demand occurred during test HS-B2, consistent with the drift level of the test, and maintains a stable response with no significant degradation in Figure 3.30B. No buckling was evidenced even at the end of HS-B4 (Figure 3.31C).

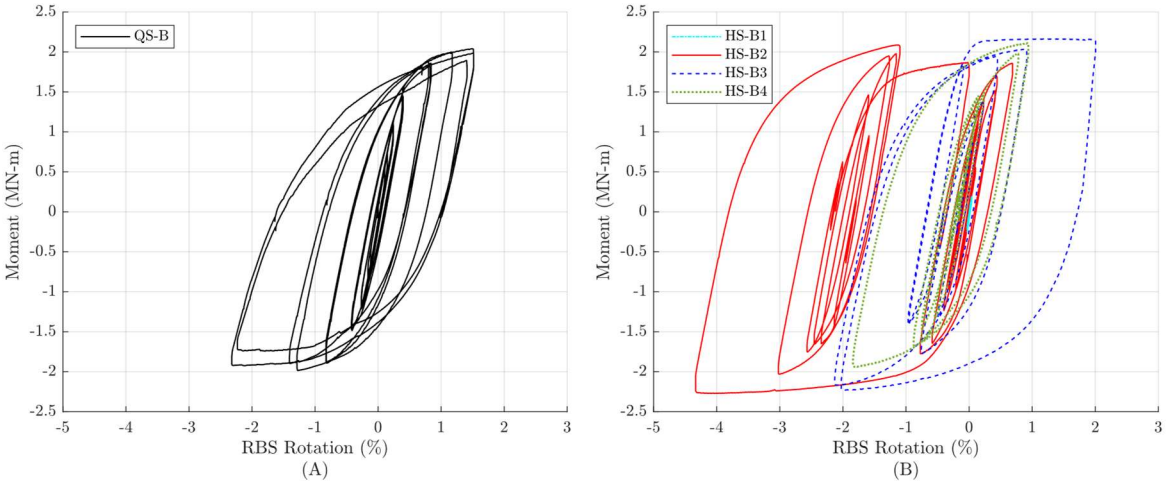

Figure 3.30: RBS local moment-rotation response: (A) QS-B; (B) HS-B.

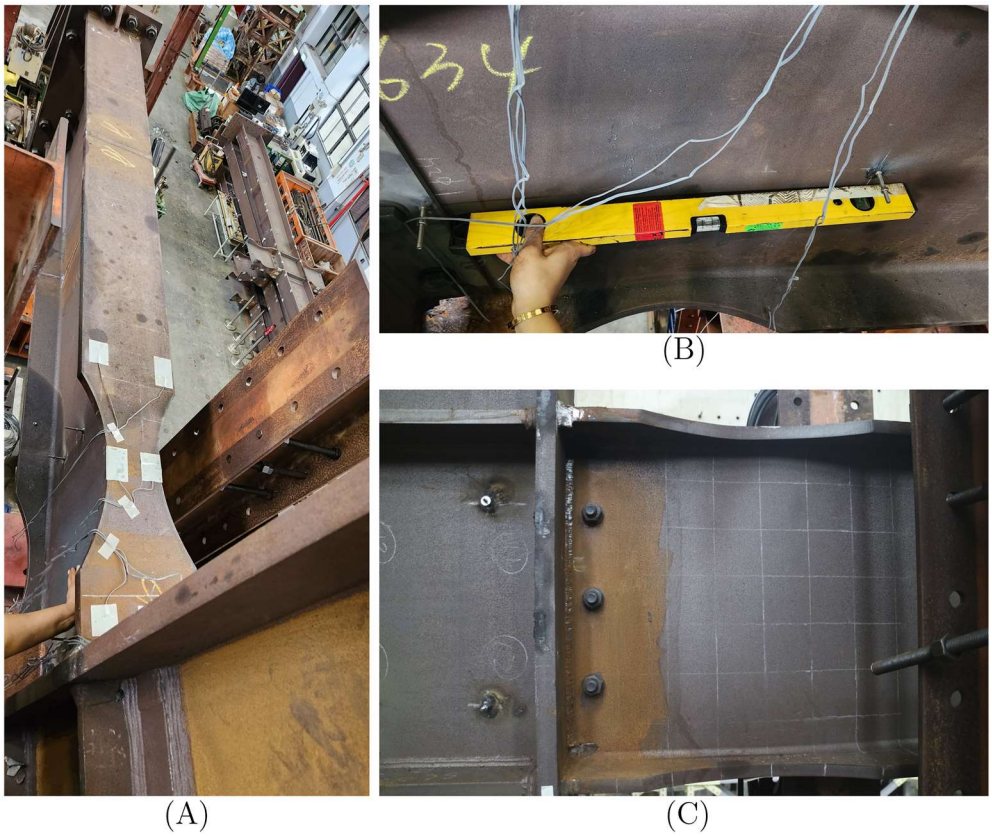

Figure 3.31: Beams for specimen B: (A) Top view of beam at the end of QS-B; (B) RBS at the end of QS-B; (C) RBS at the end of HS-B4.

Consistent with the above observations, strain gauge measurements of Figure 3.32A indicate nonsymmetric beam behavior during QS-B starting at 2% drift. However, it is unclear if

this resulted from minor local bucking in the RBS, lateral-torsional buckling, or a distortion resulting from the column buckling. For HS-B, the pair of strain gauges show that the response remains mostly symmetric.

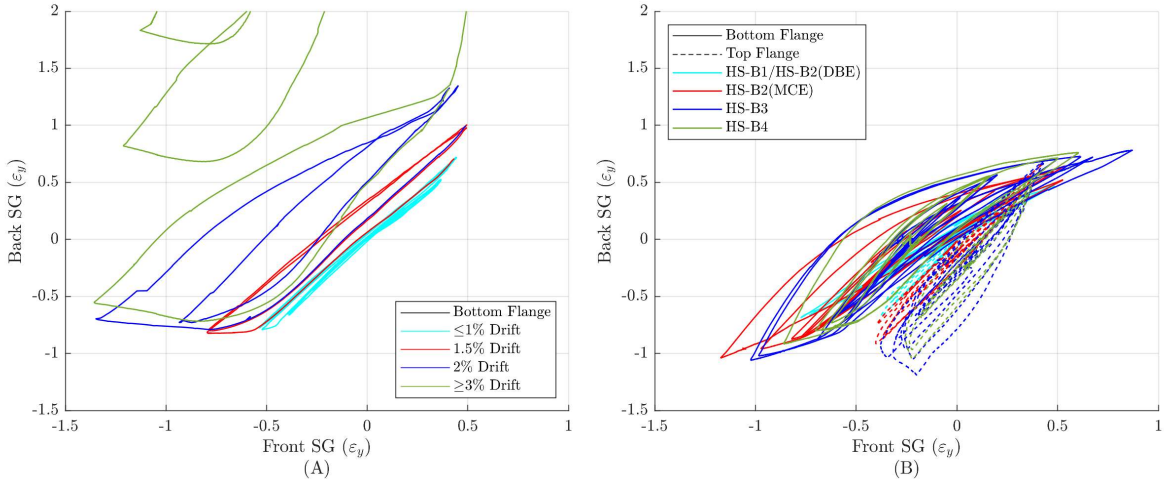

Figure 3.32: Beam flange strains at 66 cm from the column face: (A) QS-B; (B) HS-B.

3.6. Subassembly Versus Member-Level Tests

The response of columns in the subassembly during QS tests presented here are compared with member-level tests conducted at the Caltrans Seismic Response Modification Device (SRMD) Test Facility in UC San Diego [11]. A series of isolated columns were tested with different column sections, axial load levels, and boundary conditions to investigate the effect of slenderness parameters. All isolated columns were 18 ft length, having the same height as in this study. It should be noted the 18-foot height was measured at the mid-point of the panel zone, while the control point in the subassembly test was located below the panel zone, leading to a slight difference in the free column height between both tests. Test ID "2L" corresponded to a W24x131 column section, with both ends fixed, and constant axial load equivalent to C_a=16.4% using the Eq.(3.2), corresponding to the same cross section and similar axial load level as QS-A. Test ID "11M" corresponds to a column section W24x176 with both ends fixed and axial load equivalent

to C_a=32.7%, same cross-section and similar axial load of test QS-B. A comparison of the column behavior between member-level and subassembly-level test are shown below.

3.6.1. Column section W24x131 (specimen A)

Member-level testing indicated that web and flange local buckling initiated at 3 % drift and continued to increase in amplitude for 4% drift. These findings are consistent with the behavior noted during the QS-A test. Both test setups exhibited the same antisymmetric local buckling mode, with both flanges buckling inward on one side and outward on the other. The buckling pattern for both tests is shown in Figure 3.33.

(A) (B) (C) (D)

Figure 3.33: Section W24x131: (A) Column test at 3% drift; (B) Subassembly test at 3.25% drift; (C) Column test at 4% drift; (D) Subassembly test at 4.3% drift.

The moment response for both tests exhibit a comparable envelope and level of degradation (see Figure 3.34A and Figure 3.35). Member level test shows a greater initial stiffness due to the fixed-fixed boundary condition, which may trigger column yielding at lower lateral deformations. However, once the column yields, member and subassembly levels provide similar moment response. Figure 3.34B compares the axial shortening for both tests. Note that for the isolated column test, only half of the shortening is displayed herein since the fixed-fixed boundary condition produces two column ends with buckling. In contrast, for the subassembly test, the

damage is concentrated at the base for only fixed base condition. Comparable Δ_{axial} values are also evidenced for both tests, with reasonable variations considering the different loading conditions.

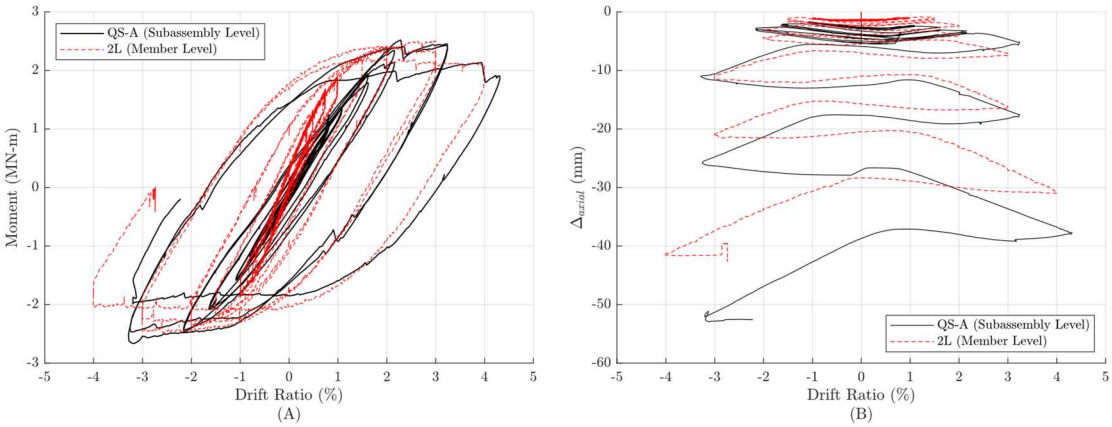

Figure 3.34: Section W24x131: (A) Moment vs Drift; (B) Axial shortening vs drift.

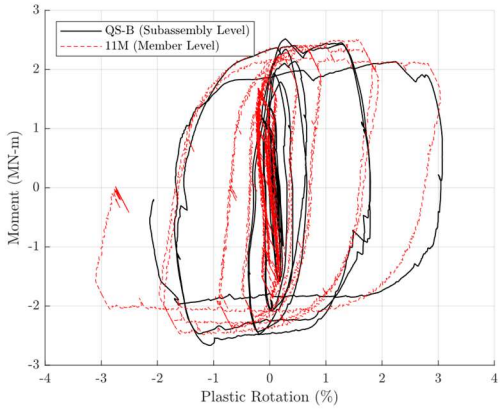

Figure 3.35: Section W24x131 - Moment vs plastic rotation.

3.6.2. Column section W24x176 (specimen B)

For the W24x176 member level test, CP was the dominant buckling mode, the same pattern observed in the QS-B subassembly test. During member level test, minor lateral-tortional buckling is reported to initiated at 1.5% drift and being more noticeable at a 2% drift ratio. This is in

agreement with visual inspections and strain gauge measurements in QS-B. Notably, the buckled length in QS-B is larger than two times the column depth (Figure 3.26B), and larger than the buckling length of QS-A, which is also consistent with member level test observations [2]. Figure 3.36 illustrates a comparison between both member-level and subassembly-level tests for 2% and 3% drift ratios.

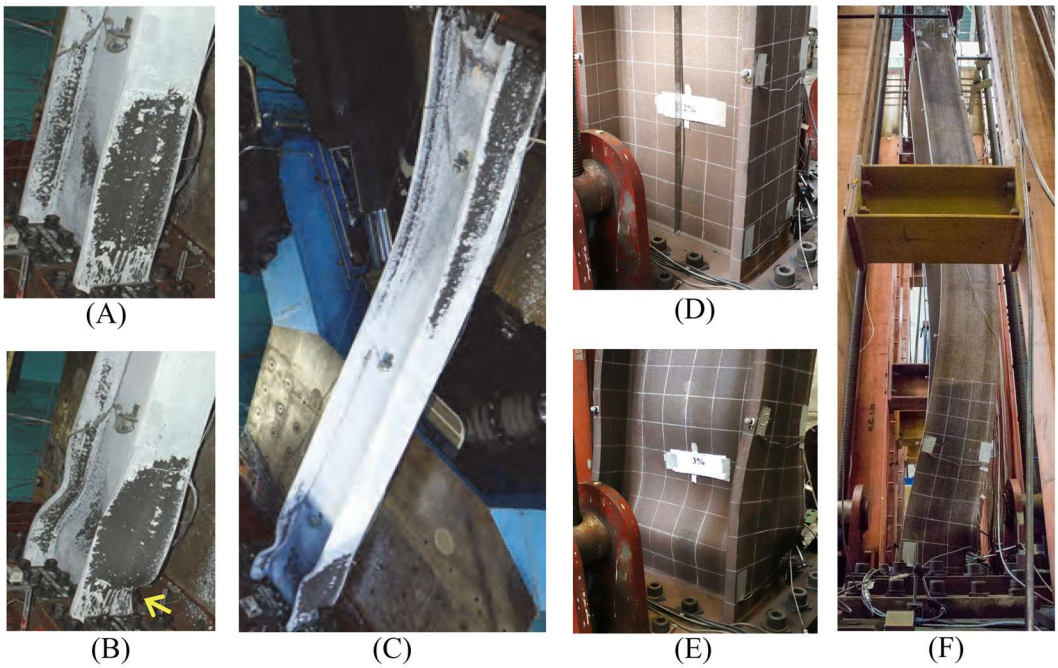

Figure 3.36: Section W24x176: (A) Column test at 2% drift; (B) Column test at 3% drift; (C) Column test at 3% drift (lateral view); (D) Subassembly test at 2% drift; (E) Subassembly test at 3% drift; (F) Subassembly test at 3% drift (lateral view).

Comparing the column moment vs drift ratio behavior (Figure 3.37A and Figure 3.38), both tests provide similar envelopes and levels of degradation. The effect of boundary conditions on the initial stiffness is also evident in these tests. Axial shortening is also almost identical in these two tests having a closer loading history in terms of drifts and applied axial loads.

Note that during member-level tests, the longitudinal force was defined constant regardless on the deformed configuration of the specimen. Conversely, the steel rods applying the axial forces

within the subassembly followed the deformed position of the column, which could modify the local P-Delta effect in presence of global buckling. Further investigation should quantify the impact of this assumption in the out-of-plane column deformation.

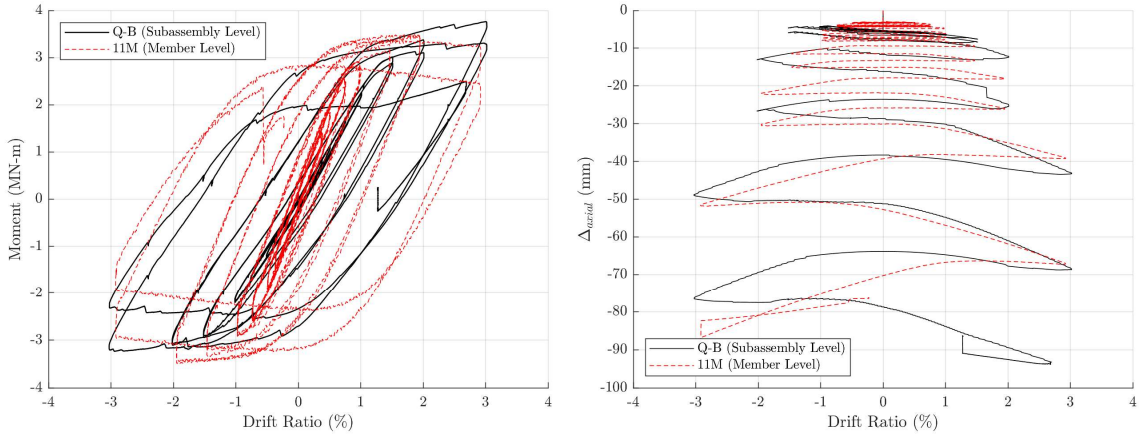

Figure 3.37: Section W24x176: (A) Moment vs Drift; (B) Axial shortening vs drift.

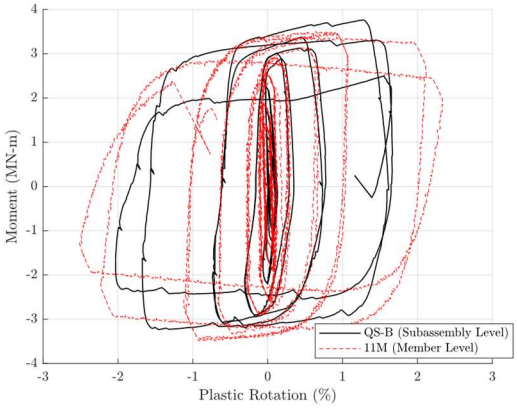

Figure 3.38: Section W24x176 - Moment vs plastic rotation.

3.7. Acknowledgements

Chapter 3, in part, is currently being prepared for publication of the material as it may appear in “Full-scale quasi-static and hybrid simulation of steel moment frame with deep and

slender columns", C. Sepulveda, G. Ozkula, G. Mosqueda, C.M. Uang, C.C. Chou, K.J. Wang, C.W. Huang, P.C. Huang, S. El-Tawil, J. McCormick. *Earthquake Engineering and Structural Dynamics*. The dissertation author was the primary researcher and author of this paper.

Chapter 4 Hybrid Simulation Framework with Mixed Displacement and Force Control for Fully Compatible Displacements

This chapter presents a new framework for hybrid simulation with mixed displacement and force control using a controller-based displacement-to-force transformation for stiff DOFs. The equivalent force concept was first presented in Sepulveda et al. [65] through purely numerical simulation and implemented by Wang et al. [61] using PISA3D [66] as the computational model for a HS involving a full-scale steel beam-column subassembly. This previous application used twin numerical models running in parallel to estimate the equivalent nodal force applied in the numerical model. Considering the horizontal-vertical coupling of fiber-based element used in HS presented here, the overall framework is formalized for nonlinear problems through a controller-based approach that minimizes the difference between the measured and numerical model displacements. The framework is first presented and evaluated by virtual hybrid simulations. Then, its performance is analyzed in the context of its application to the HS of this study.

4.1. Mixed Displacement and Force Control Framework

The mixed displacement and force control framework was developed to be applied within the displacement-based time integration schemes typically used for nonlinear time history analysis. The numerical model essentially sends displacement parameters and receives effective nodal forces. Figure 1 illustrates the framework for a simple frame with a 2DOF experimental substructure. The lateral loading of the specimen is applied using displacement control as typical, while the vertical axial load is applied in force-control due to the high stiffness of this DOF. The axial load on the column is obtained using a linear elastic beam-column element that functions as a *numerical load cell*, by sending its nodal displacements to obtain the element axial deformation. The force F_2^{cmd} can then be calculated for the element and used as the force commanded for the vertical actuator. The linear elastic *numerical load cell* element should be located in a section of the column expected to remain linear. An element length equal to or larger than the sectional depth is recommended considering that the resolution of the element deformation can be captured with sufficient accuracy. Previous HS applying time-varying force commands have used this approach [29,67,68] that can be readily applied in most displacement-based structural analysis software. There may be more direct ways to extract the numerical column force from the numerical substructure depending on the software options available.

In past applications of axial load force-control, an elastic truss element (labeled *ghost* element) has been used to replace the experimental substructure in the numerical model to maintain force equilibrium in the vertical direction. The *numerical load cell* and *ghost* elements are depicted in Figure 4.1. The *load cell* element requires the same cross-section and material properties of the element section that it substitutes in the numerical substructure. It is recommended for the *ghost*

element to have identical elastic axial properties to that of the physical element, however, the properties can be modified in the mixed control approach as described in more detail later.

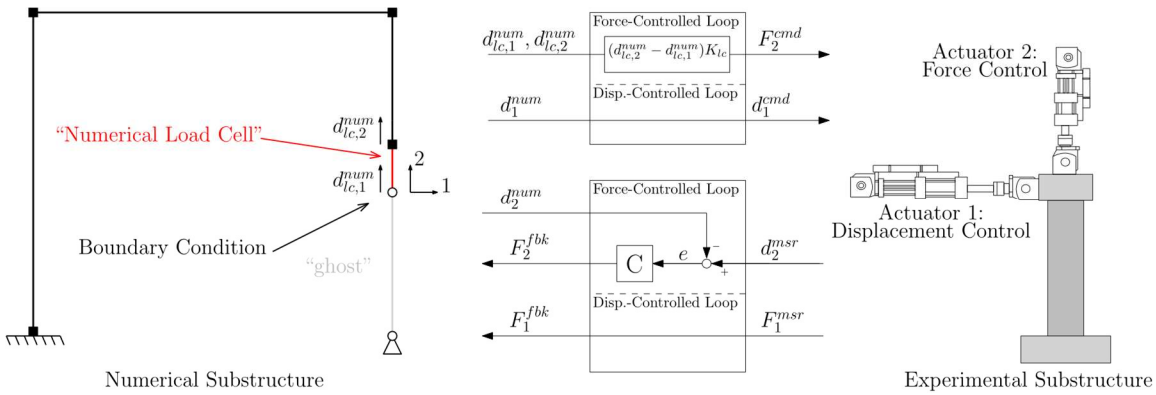

Figure 4.1: HS Framework with communication signals.

4.1.1. Equivalent feedback force calculation

The feedback to the numerical model for force controlled DOFs is an equivalent nodal force F_2^{fbk} with the objective of achieving a compatible displacement in the frame numerical model including the *ghost* element. The force is calculated based on the approximate stiffness of the numerical frame and the measured vertical displacement of the column, d_2^{msr}. Considering the high axial stiffness of the *ghost* element and potential nonlinear contributions from the frame, the equivalent force F_2^{fbk} is calculated through a controller-based algorithm. The relationship between displacement and equivalent force examined for the applications here is mildly nonlinear and can be achieved with a simple controller. A more advanced controller can be selected for more complex applications.

4.1.2. Closed-loop feedback controller transformation

The nonlinearity in the displacement-to-force transformation is due to the coupling of the vertical DOFs with the numerical model and the nonlinear behavior of numerical elements. A closed-loop feedback controller is applied to adjust the equivalent feedback force to arrive at a compatible displacement with measured column response. The input signals include the measured displacement of the physical specimen, d^{msr}, and the displacement of the numerical substructure computed in the last committed integration step d^{num}. The difference between these two inputs is the displacement error, e, to be minimized by the controller algorithm denoted as block C in Figure 4.1. The output is the required force, F^{fbk}, aiming to bring this displacement error to zero and therefore enforce displacement compatibility. In this study, the forward Euler discrete form of a proportional-integral (PI) controller is used:

$$F^{fbk}[k] = K_p \cdot e[k-1] + K_i \cdot \sum_{n=0}^{k-1} e[n]\Delta t \tag{4.1}$$

where K_p and K_i are the proportional and integral gains, respectively, Δt is the time-integration step of the numerical simulation, and the displacement error $e[n]$ is calculated as:

$$e[n] = d^{msr}[n] - d^{num}[n] \tag{4.2}$$

The initial controller gains K_p and K_i, are obtained using the Ziegler–Nichols heuristic method [69]. This method requires the definition of two parameters: ultimate gain, K_u, and ultimate period, T_u. In this study, the following relationships were used as initial trial gains K_p^0 and K_i^0:

$$K_p^0 = 0.45K_u \qquad \& \qquad K_i^0 = 1.2\frac{K_p}{T_u} \tag{4.3}$$

Controller tuning should also consider measured displacement noise to prevent high-frequency force feedback. Since the transformation is employed to imposed certain displacement within the numerical substructure, K_i and K_p can be defined beforehand through pure numerical simulation.

4.1.3. Initial Definition of Controller-Transformation Parameters

According to Ziegler–Nichols heuristic method, to estimate the ultimate gain K_u, a purely proportional controller needs to be used first to control the plant. Starting with a small value, the proportional gain is increased until the system becomes unstable. The gain used right before the instability is defined as K_u and the period of the oscillation of the system is defined as T_u.
In the context of the mixed displacement and force control framework, the plant is the numerical substructure. The gain K_u has units of stiffness. To carry out this initial tuning process, an additional script needs to be added to the numerical model to apply an external force (the output signal of the controller) at the DOF where the measured displacement needs to be imposed, and update that force every integration-step based on:

$$F^{fbk}[k] = K_u \cdot (d^{msr}[k-1] - d^{num}[k-1]) \tag{4.4}$$

In this study, the calculated feedback force is then applied as an external load at the boundary condition node by updating a previously defined load pattern using the OpenSees function *updateParameter* [26]. After the feedback force is updated, the next time-integration step is computed.

In order to induce oscillations, a perturbation has to be added to the structure. This can be done by imposing certain new displacement d^{msr}, or another external excitation like a ground

motion that produce displacements in the DOF being controlled. A simple ground acceleration impulse is enough to trigger oscillations in a dynamic analysis model. Due to the high stiffness of the *ghost* element (K_{ghost}), the gain K_u has the same order of magnitude than the *ghost* stiffness. Therefore, it is recommended to define K_u relative to K_{ghost}:

$$K_u = \gamma K_{ghost} \tag{4.5}$$

Figure 4.2 depicts the response of the DOF 2 of the structure shown in Fig. 1 when there is instantaneous measured vertical displacement of 1 mm. Two different values for γ are used. For $\gamma = 1.0$, the response of the structure is damped out due to its inherent damping. When γ is increased up to 1.7 in this example, the structure starts to have an unstable response, with a growing amplitude over the time. Therefore, in this case the ultimate gain is defined equal to 1.7 times K_{ghost}, and the period of the unstable oscillation corresponds to $T_u = 0.01425$ sec. Note that γ depends on the structural model, therefore for a different structural, the value of γ will differ from the one obtained here.

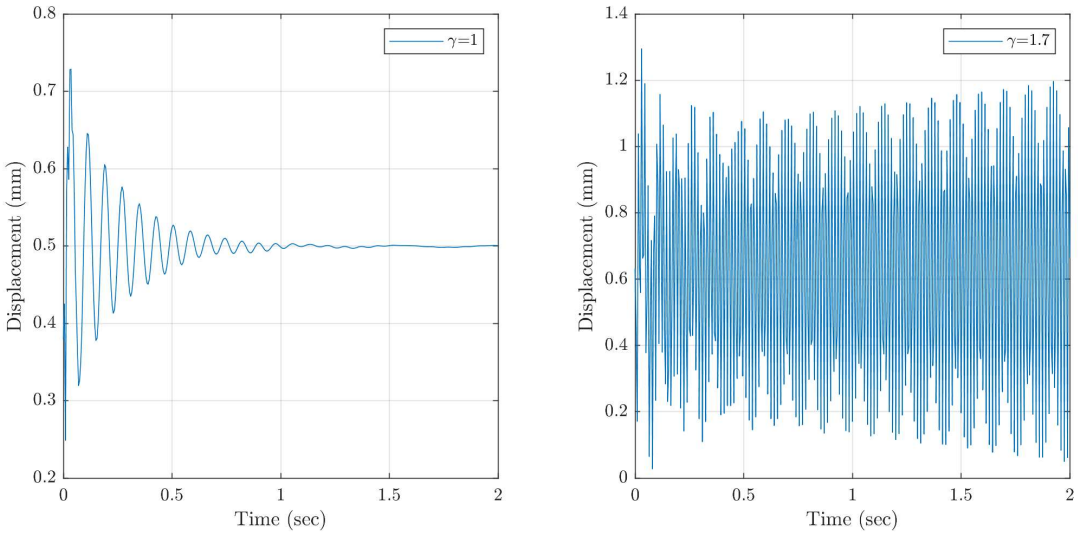

Figure 4.2: HS Displacement history of the controlled DOF for two different γ values

It is worth mentioning that if the gravity loads are applied through a static analysis, the "plant" for the controller is different due to the absence of a mass and damping matrix in the analysis. Therefore, a different K_u and T_u has to be defined for the gravity load application. Having K_u and T_u computed, the initial PI initial controller can be defined as:

$$K_p^0 = 0.45K_u = 0.45\gamma K_{ghost} = 0.765K_{ghost} \tag{4.6}$$

$$K_i^0 = 1.2\frac{K_p^o}{T_u} = 0.54\gamma\frac{K_{ghost}}{T_u} = 64.4K_{ghost} \tag{4.7}$$

4.2. Verification Through Virtual HS of Moment Frames Subassembly with Column Shortening

HS of steel moment frame buildings including a full-scale cruciform subassembly with deep section members were conducted. The columns were expected to experience both local and global buckling under the combined axial and lateral loads [2]. It is the expected column axial shortening that motivated the proposed framework with mixed displacement and force control. The details of the implementation are described including preliminary validation and parameter tuning through a virtual HS. The focus of this chapter is on the presentation and performance of the HS framework, with more details on the archetype buildings, HS setup, and behavior of the steel moment frame structures previously described in Chapter 3.

The proposed framework is first verified through a virtual hybrid simulation using Prototype Building B subjected to the Mw 6.9 Kobe Earthquake, scaled to MCE level by a factor of 0.99. The experimental substructure is simulated as a separate structure in OpenSees and coupled with the numerical substructure through OpenFresco and an *Adapter Element* in the virtual specimen model [70]. The virtual model as limited by current modeling capabilities in OpenSees is not able to simulate axial shortening due to column buckling. Instead, the measured vertical

displacement signal for the vertical DOF is artificially modified to simulate column shortening by adding a half-cycle cosine shape function with a maximum of 20 mm. The force command variation and vertical displacement are plotted in Figure 4.3. It can be observed that the method successfully enforces the displacement compatibility between simulated shortening (target) and the vertical displacement in the numerical model.

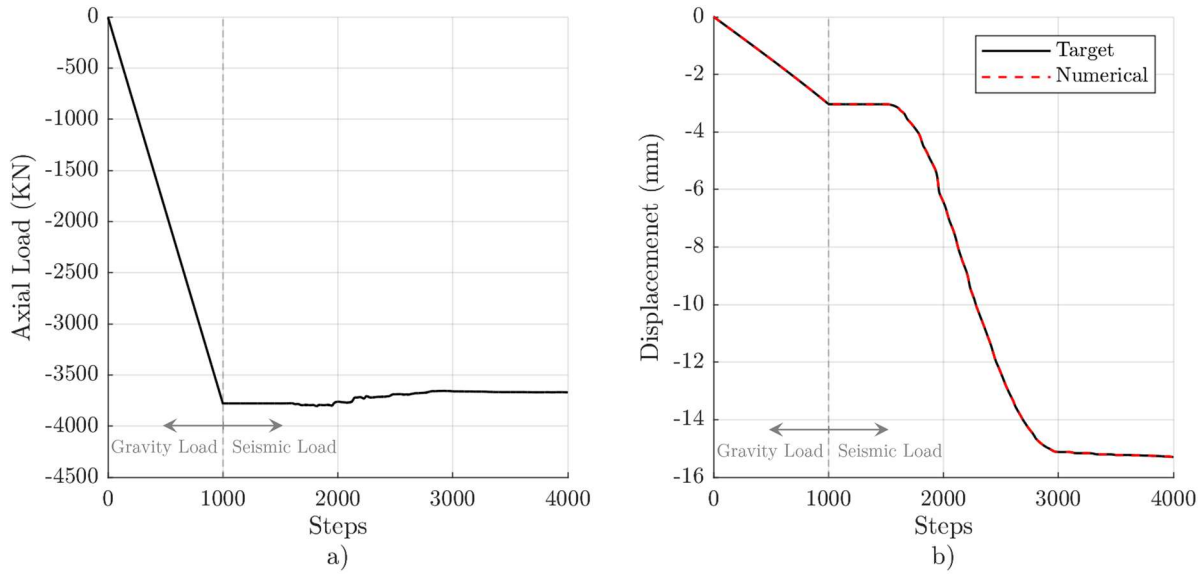

Figure 4.3: Axial response for initial controller: (a) Axial force command; (b) simulated shortening (target) and numerical (committed) column vertical displacements.

To account for the presence of noise in the measured displacement signal, zero-mean Gaussian noise with a standard deviation of 0.02 mm is artificially introduced. Measurement data using the same instruments and digital filtering showed that the displacement feedback contains noise with amplitude in the range of 0.01 to 0.02 mm, comparable to expected noise in the experimental setup. The virtual simulations are also used to refine the initial gains obtained from the Ziegler-Nichols heuristic considering the influence of measured noise on the system response. This modification is carried out with the aim of also minimizing the controller delay. It was found

that by employing $K_p=K_p^0/10$ and $K_i=10K_i^0$, the performance improved for the analyzed model. An amplified view of the noisy response for both controllers are shown in Figure 4.4.

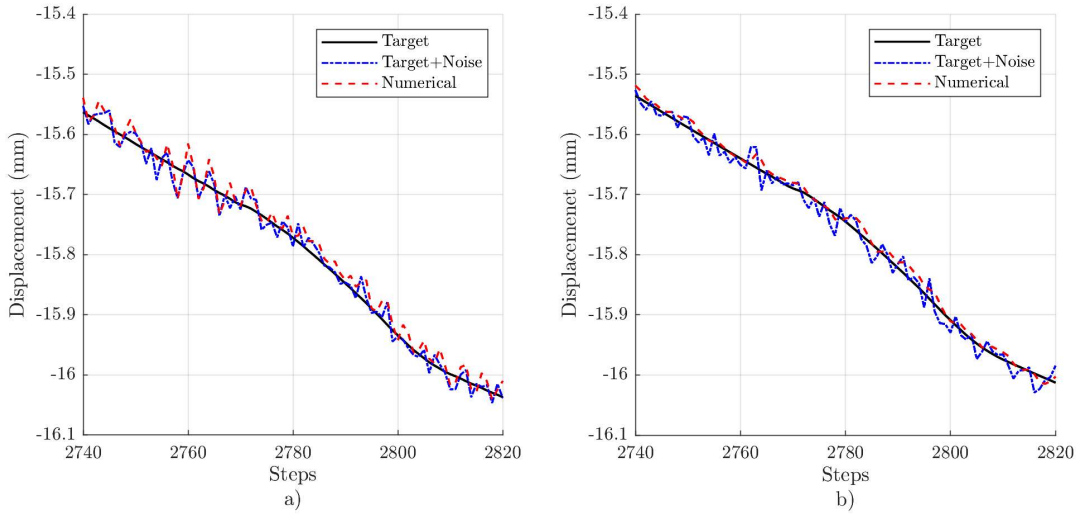

Figure 4.4: Close up view of vertical displacement response: a) Initial controller; b) Tunned controller.

The performance of the trial gains was also assessed by comparing the Normalized Root Mean Square (NRMS) of the tracking error resulting from the controller transformation defined as:

$$NRMS = \sqrt{\frac{\sum_{i=1}^{N}\left[Y_{target,i} - Y_{num,i}\right]^2}{\sum_{i=1}^{N}\left[Y_{target,i}\right]^2}} \tag{4.8}$$

The delay was estimated based on the lag that minimized the NRMS error. Additionally, the noise in the committed displacement signal was extracted via a high-pass filter, and its standard deviation was computed to quantify the transmitted noise. Lastly, the noise transfer ratio, defined

as the ratio between the noise standard deviation in the output and input signals, was calculated to further evaluate the performance of the system. Table 4.1 summarizes the results obtained.

The comparative analysis of the controllers reveals that there exist similar levels of error and delay in both cases. However, the noise introduced by the initial controller into the numerical model is comparable to the feedback noise. In contrast, the refined controller successfully reduces the noise, with a transmission of approximately one-third of the feedback noise and therefore was selected to be used in the actual HS. More details about the sensitivity of the controller-transformation can be found in Sepulveda and Mosqueda [71].

Table 4.1: Controller performance parameters

Parameter	Initial Controller	Tunned Controller
NRMS error (for noiseless signal)	0.09%	0.09%
Delay (for noiseless signal)	1.13Δt=0.0056s	1.28Δt=0.0064s
Transmitted Noise	0.0189 mm	0.0073 mm
Noise Transfer ratio (O/I)	94.60%	36.40%

4.3. HS with Full Scale Experiment Experiencing Axial Shortening

The HS of this study were conducted using the framework described previously. Figure 4.5 shows the experimental setup at the end of one of the tests. Results of the hybrid test with emphasis on the performance of the HS framework are described here.

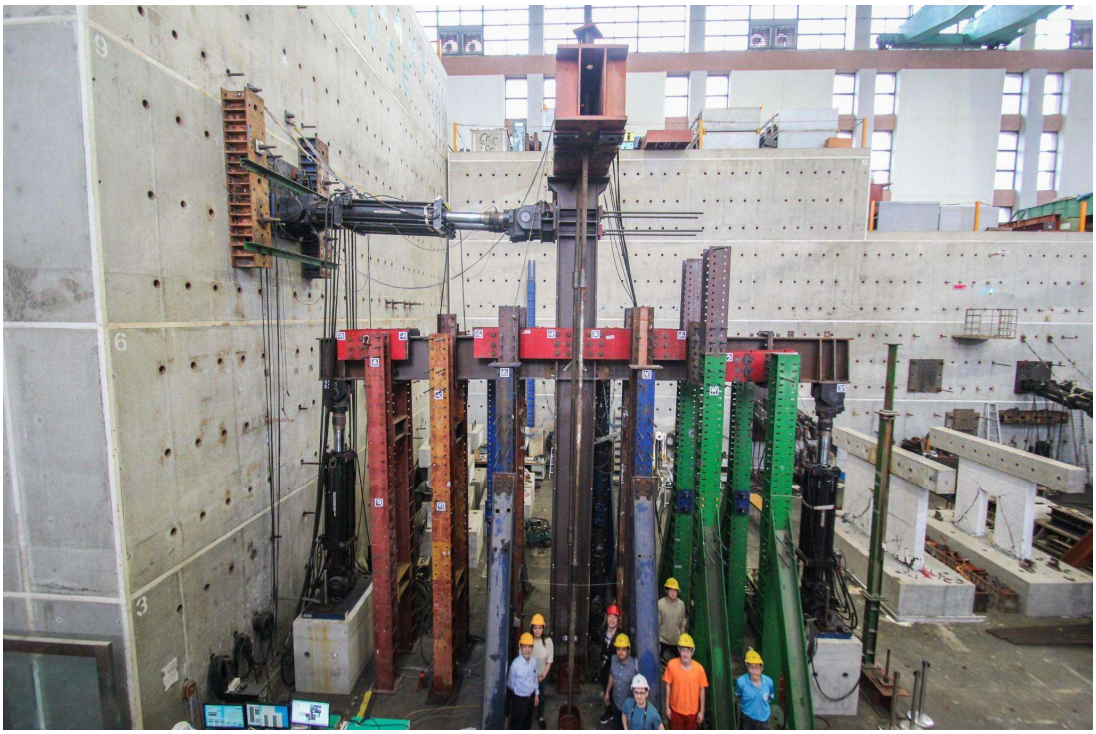

Figure 4.5: Experimental setup.

Models of both archetype buildings (A and B) and their corresponding experimental substructures were subjected to the testing sequence described in Table 3.2. The gravity load was first applied through static analysis. An elastic-level ground motion was then applied to verify the experimental setup, followed by two sequential ground motions scaled to DBE and MCE intensity. Subsequent tests were carried out following the two simulations if sufficient capacity remained in the specimen to gain experimental data and the progress of damage towards failure. Importantly, the structural specimen incurred damage after the second hybrid test, while the numerical substructure started from an undamaged state in the subsequent simulations.

The performance of the mixed control framework is evaluated in detail for Test HS-B, which had the most shortening. Figure 4.6 presents the first story drift obtained from the sequence of motions for the HS-B tests. The maximum drift ratio obtained were 0.15% for the elastic level test and 5% for the two-sequence motion in HS-B2. The specimen was recentered with actuator

forces close to zero and the software restarted for HS-B3. The state of the column base after HS-B2 and HS-B3 tests are illustrated in Figure 4.7. After HS-B2, vertical displacement and strain gauge measurements suggest the initiation of local buckling. However, local buckling is visually detectable after HS-B3.

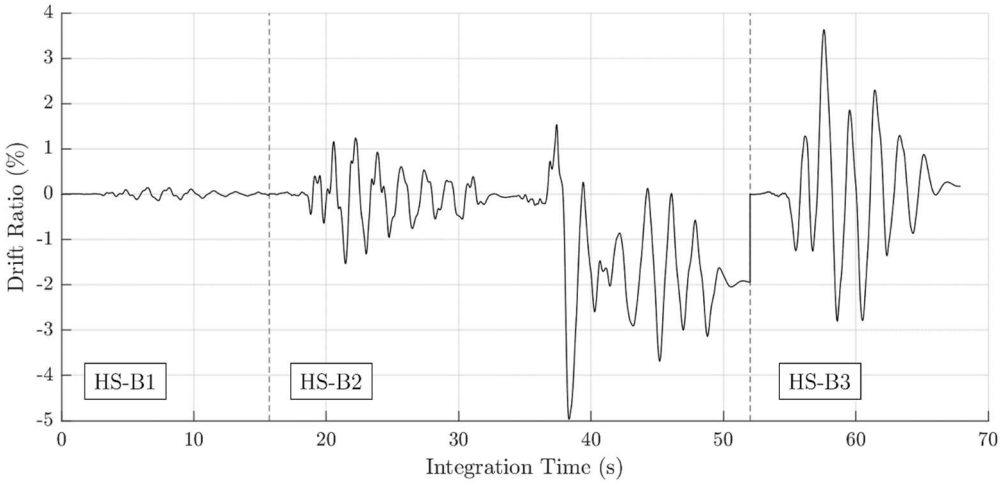

Figure 4.6: First story drift ratio for tests HS-B1, HS-B2, and HS-B3.

a) b)

Figure 4.7: Photo of column base: a) After HS-B2; b) After HS-B3.

Figure 4.8 to Figure 4.10 shows the axial load command and vertical displacement responses of the structure for the three HS-B tests. As expected, the vertical displacement and axial load remain almost constant for HS-B1 test (elastic level). During HS-B2, the column, experienced 10 mm-axial shortening, mainly during the MCE intensity motion. For HS-B3 with increase in seismic intensity and column axial load, a cyclic pattern of vertical displacement is observed with a cumulative residual of approximately 20 mm. Notably for HS-B2 and HS-B3, the column axial shortening is correlated with its decrease in the axial load command from the numerical substructure capturing the redistribution of loads. Minor local buckling occurs near the column base (Figure 4.7).

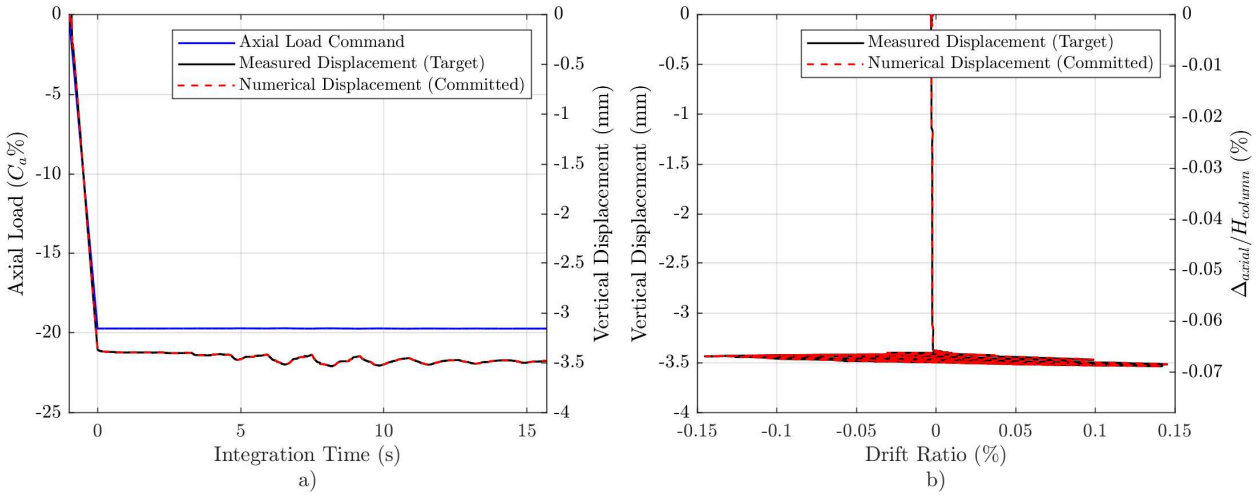

Figure 4.8: Test HS-B1: a) Axial load command and displacement tracking time-history; b) Vertical displacement versus drift ratio.

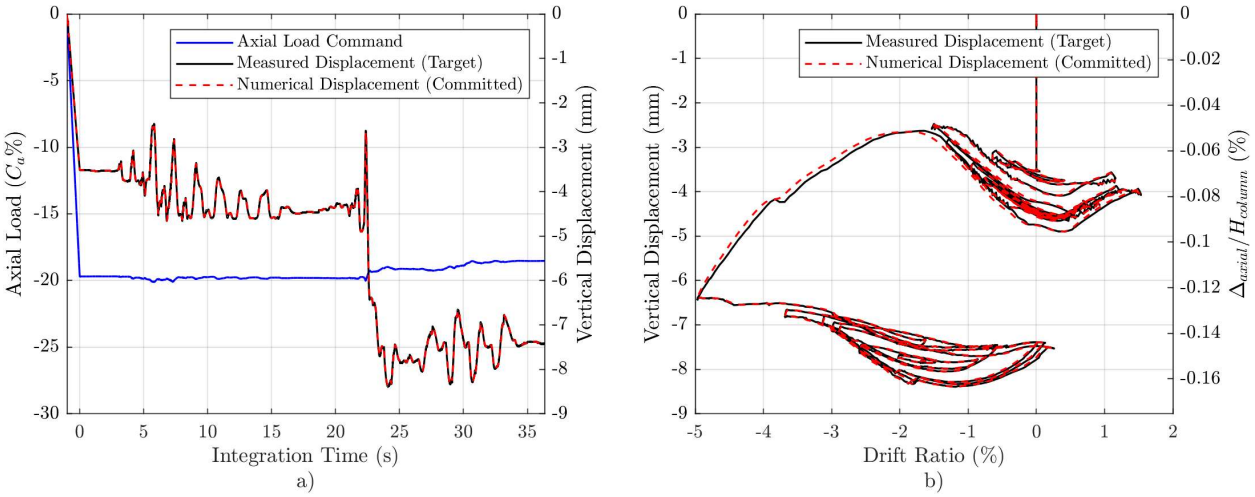

Figure 4.9: Test HS-B2: a) Axial load command and displacement tracking time-history; b) Vertical displacement versus drift ratio.

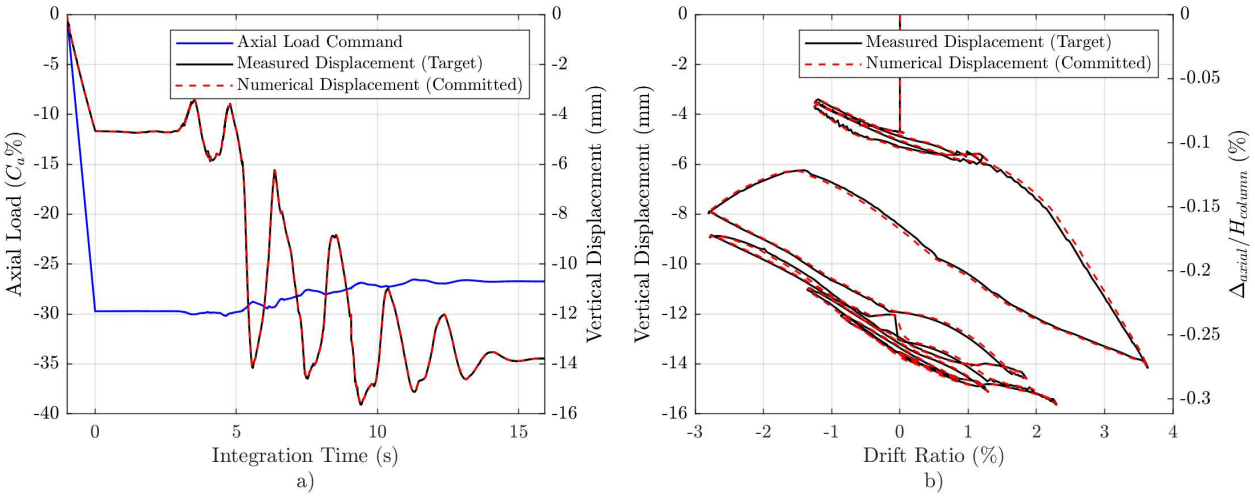

Figure 4.10: Test HS-B3: a) Axial load command and displacement tracking time-history; b) Vertical displacement versus drift ratio.

4.4. Discussion of Results

4.4.1. Performance of the controller-based transformation

This section presents an analysis of the performance of the HS framework including effects of errors. The delay and NRMS error of the numerical displacement for both the gravity load and

dynamic analyses are presented in Table 4.2. Different controller transformations are used for the gravity load application (static) and time-history analysis (dynamic). The controller functions effectively during the gravity phase with minimal delay, even having a lead for HS-B3. The *ghost* element captures the axial behavior of the experimental subassembly effectively, leaving minimal corrections for the controller. Furthermore, with no horizontal motion, the system is linear in the vertical direction, making it easier to handle by the controller-based transformation. In contrast, during the dynamic motion, although the *ghost* element cannot account for vertical deformation resulting from rocking of the flexible base plate, column yielding, and buckling, such nonlinear characteristics are compensated by the controller, with a delay in achieving the desired displacements in the numerical model. For the dynamic simulations, the three tests have similar performance, meaning that the effectiveness of the controller transformation does not have a direct relationship with the amplitude of the signal.

Table 4.2: Performance measures for full-scale hybrid tests

Gravity Load Analysis			
Parameter\Test:	HS-B1	HS-B2	HS-B3
Average Delay	0.05Δt=0.00025s	0.06Δt=0.0003s	-0.1Δt=-0.0005s
NRMS error	0.11%	0.09%	0.09%
Time-History Analysis			
Parameter\Test:	HS-B1	HS-B2	HS-B3
Average Delay	1.44Δt= 0.00072s	1.48Δt=0.0074s	1.49Δt=0.00745s
Maximum Delay	1.47Δt = 0.00735s	1.51Δt=0.00755s	1.54Δt=0.0077s
Maximum Disp. Rate	0.00231mm/s	16.7mm/s	27.0mm/s
NRMS error	0.03%	0.36%	0.49%

Figure 4.11 presents a close-up view of the vertical displacement to examine the noise during test HS-B2. It can be observed that the controller transformation reduces the noise in the

measured to numerical displacement with the improved tunning. Additional noise in the applied equivalent force can lead to oscillations and potential amplification by the numerical integration.

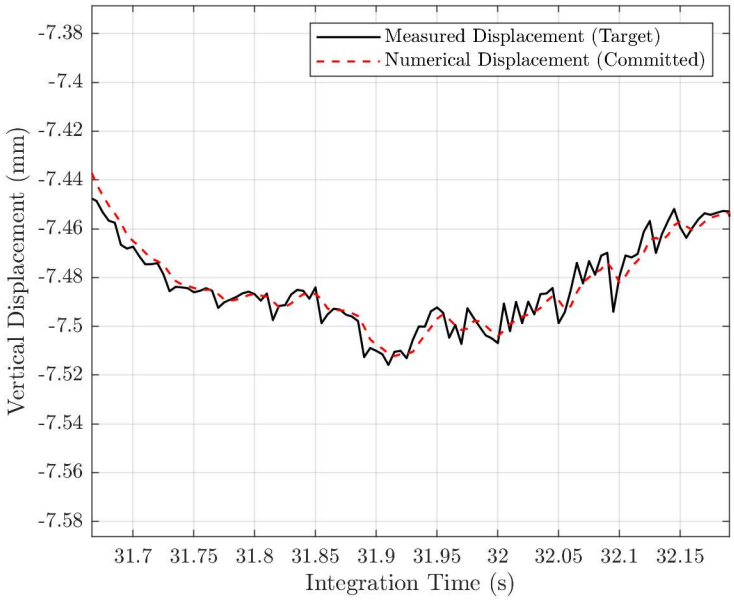

Figure 4.11: Test HS-B2: Close up view of displacement tracking performance.

4.4.2. Effect of the delay in a force-based HS

Delays in the force controlled DOFs and its potential effects on the stability of the simulation are examined. It is well known that for displacement controlled DOFs, a delay in the feedback force has a negative damping effect that can results in instability of the numerical simulation [72]. Similarly, a lead or overshoot can give a positive damping effect [73]. In force-control mode, the effect is the opposite: a delay in the force application produces a lag in the measured displacement, leading to a positive damping effect and vice versa. A similar effect results when the proposed controller transformation produces a lag/lead in the committed displacement in the numerical model. As shown in Figure 4.12(a), assuming a perfect force command application on the specimen, a lag in the numerical displacement produces a positive damping

effect. Conversely, a lead in the committed displacement leads to a negative damping effect (Figure 4.12(b)).

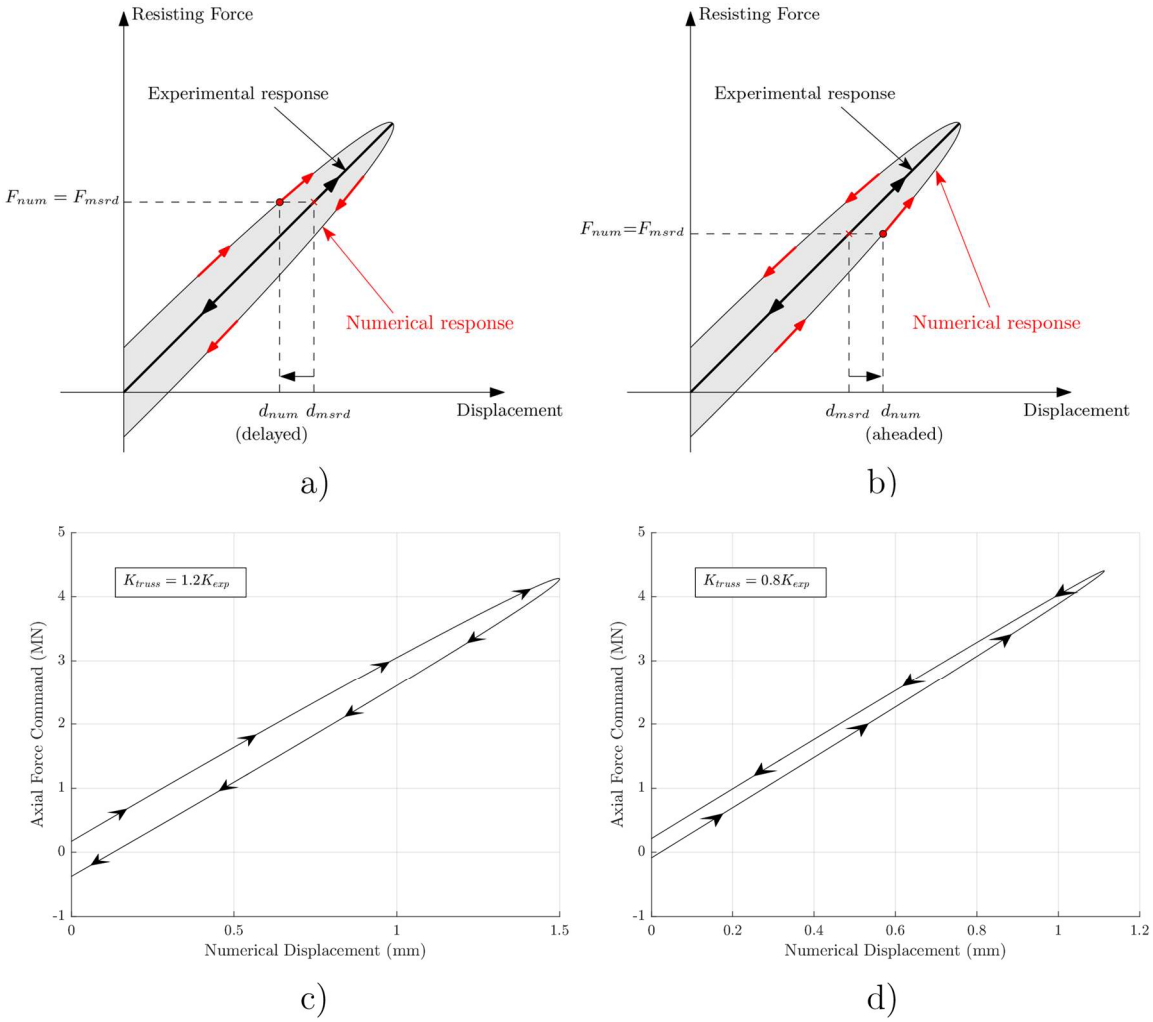

Figure 4.12: Damping effect of controller transformation: a) lag in the numerical displacement; b) numerical simulation for ghost element with larger axial stiffness; c) lead in the numerical displacement; d) numerical simulation for ghost element with smaller stiffness.

The effects of delay in the application of the displacements to the numerical model also depends on the stiffness of the *ghost* element. If the *ghost* element is stiffer than the physical specimen, a force needs to be applied in the same direction as the displacement increment, resulting in a delay in the committed numerical displacement and therefore a positive damping effect. In

contrast, if the *ghost* element is more flexible than the experimental stiffness, the controller must compensate for the stiffness insufficiency and provide the required resisting force acting in the opposite direction of the desired displacement increment. This leads to a committed displacement ahead of the target value and hence a negative damping effect. Therefore, if numerical stability during elastic testing is a concern, an upper bound for the axial stiffness of the specimen is recommended as the *ghost* element stiffness. A virtual hybrid simulation using the structure of Figure 4.1 is carried out employing a *ghost* element stiffness equal to 1.2 and 0.8 times the experimental stiffness to verify this observation. Figure 4.12(c) depicts one cycle of the stiffer *ghost* element case showing the mentioned delay, while Figure 4.12(d) depicts the corresponding cycle for the more flexible *ghost* element exhibiting a lead.

4.4.3. Monitoring of numerical stability

The use of numerical models with high levels of nonlinearity can have a risk for numerical stability. Hashemi et al.[74] observed that a numerical instability in a hybrid simulation (HS) can be correlated with a large unbalance force in the numerical integration scheme. This finding holds significance as an abrupt change in the measured displacement translates to a sudden change in the force superimposed by the proposed method. To monitor the unbalance force during the HS, a stability margin index was computed for every integration step. The calculation of the index was carried out in accordance with

$$I_s = Log_{10}\left(\frac{PU_{Limit}}{PU_i}\right) \tag{4.9}$$

where PU_i is the unbalance force of the time integration i, and PU_{Limit} is an estimation of the unbalance force that generates numerical instability based on virtual HS conducted beforehand.

Consequently, a value of I_s near 0 signifies a narrow margin for stable simulation, whereas a negative value indicates an impending instability concern.

Figure 4.13(a) illustrates a close view of the displacement tracking in test HS-B3. The displacement history indicates a substantial displacement change of around 1 mm from one integration step to the next, presumably attributed to a temporary obstruction and subsequent release of a component within the displacement measurement setup. Since the time-integration step is 0.005 seconds, this velocity for the numerical component is equivalent to 200 mm/s. Hence, the controller-based transformation imposed a new equivalent force with a large increment of ΔF as observed in Figure 4.13(b).

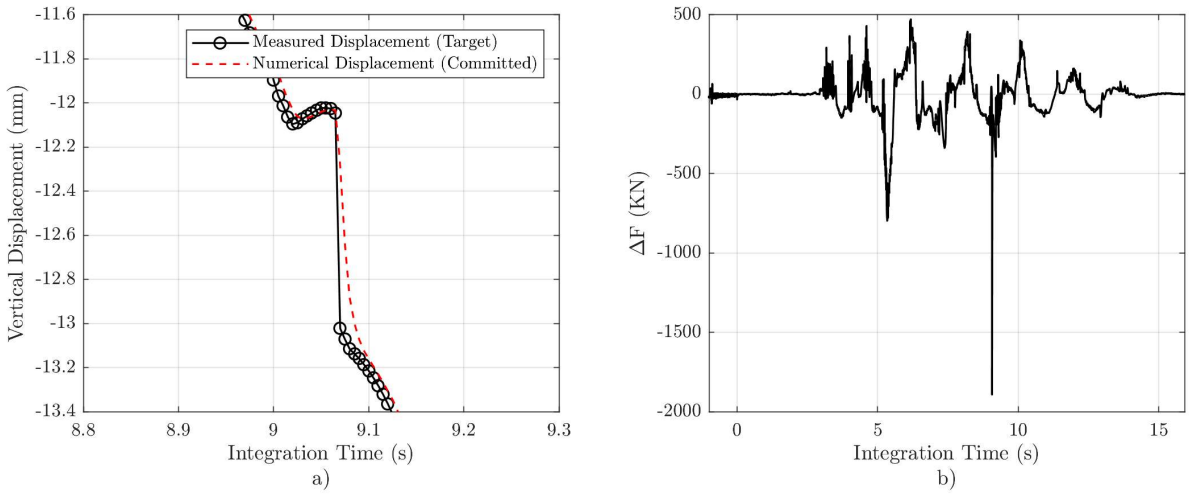

Figure 4.13: Test HS-B/3: a) Zoom-in to a sudden measured displacement increment; b) Force increment from the controller-based transformation, ΔF, every time-integration step.

A spike in the unbalance force history can be seen in Figure 4.14(a), along with the corresponding margin index in Figure 4.14(b). Notably, the stability margin index can be observed to drop from peaks around 3 to 2. This finding highlights the benefits of utilizing a controller-based transformation tuned to minimize noise. While a larger proportional gain can result in

reduced delay, it can also increase the unbalance force in the integration scheme with the potential for instability.

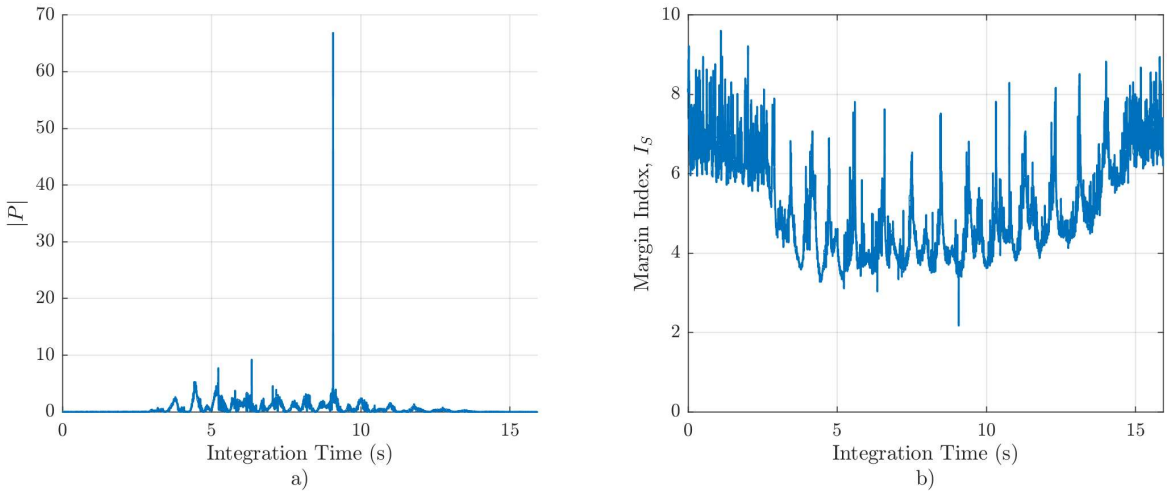

Figure 4.14: Stability statistics during HS-B3: a) Norm of unbalanced force; b) Stability margin index.

4.5. Acknowledgements

Chapter 4, in part, is a reprint of the material as it appears in "Hybrid simulation framework with mixed displacement and force control for fully compatible displacements." C. Sepulveda, G. Mosqueda, K.J. Wang, P.C. Huang, C.W. Huang, C.M. Uang, C.C. Chou (2023). *Earthquake Engineering and Structural Dynamics*. https://doi.org/10.1002/eqe.4048. The dissertation author was the primary researcher and author of this paper.

Chapter 5 Selective Online Model Updating in Hybrid Simulation of a Full-Scale Steel Moment Frame

RBS connections are prone to cyclic deterioration caused by steel yielding and local buckling that contribute towards the challenges in modeling the seismic performance of steel special moment frames. Pure numerical simulations of the archetypes of this study showed variations in the beam plastic hinges demands, providing a unique opportunity to apply OMU, taking full advantage of the data measured during the experiment and improving column boundary conditions. Importantly, beam fracture was observed in some of the experiments, which prompted a selective update feature since updating all connections to this data would indicate simultaneous fracture of all connections. This conditional feature ensures that the simulation remains physically meaningful to capture the expected propagation of failure. The focus of this chapter is on the development and full-scale application of the OMU with more details on the overall experimental program available in Chapter 3.

5.1. Numerical Substructure for OMU

Beams were modeled using an elastic beam-column element for the middle section, while each end was equipped with rigid offsets and a lumped plasticity spring. Starting from the third story, the response of the RBS was simulated using the Ibarra-Medina-Krawinkler (IMK) model [53], with the initial properties based on the recommendations of Lignos & Krawinkler [54]. The IMK hinge properties were calibrated from quasi-static cyclic tests on the experimental substructure conducted prior to the HS. For the RBS hinges located on the second story, an updatable material model was employed to implement the OMU proposed in this study. Since the beam design does not include studs for the composite slab at the RBS region, composite action is only considered in the central elastic beam element. Figure 5.1A depicts a scheme of the frame model and Figure 5.1B illustrates the modeling scheme for the beam-to-column connections. Figure 5.1C shows RBS rotation for the eight second-story hinges from a numerical simulation, emphasizing that odd and even ID hinges are out of phase, but with similar load pattern and peak absolute values. Note that the exterior hinges (ID 1 and 8) have a slightly larger demand, and will have properties updated from internal hinges as part of the OMU since they are not physically tested.

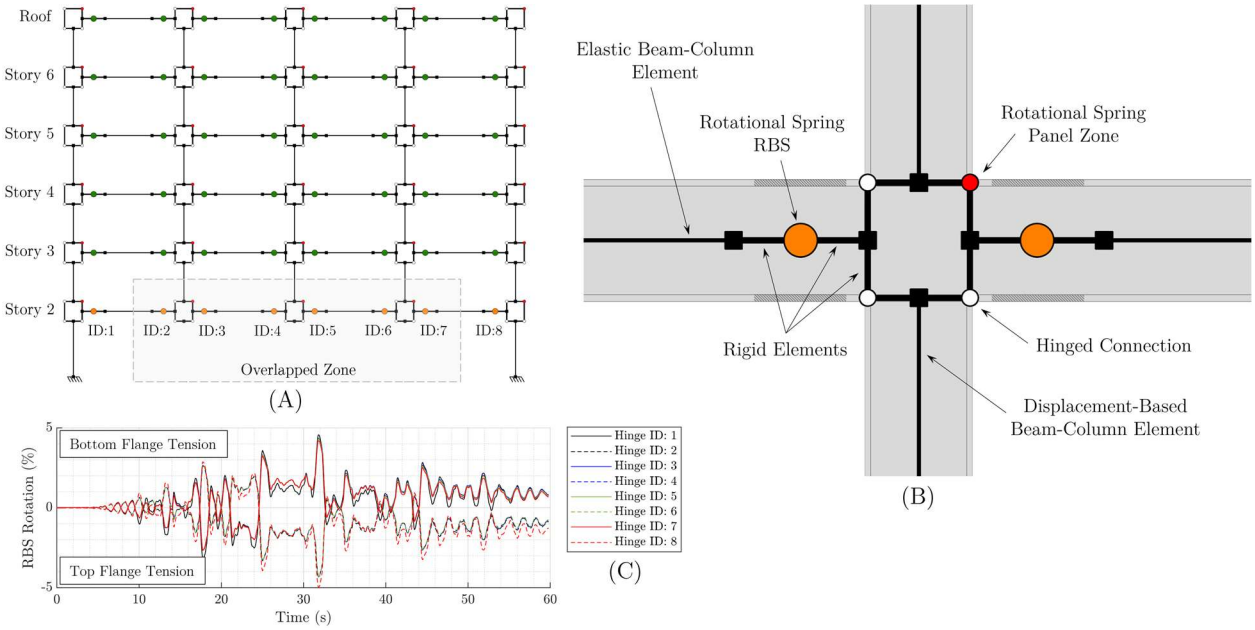

Figure 5.1: Numerical substructure: (A) Frame model with beam IDs; (B) Beam-to-column connection; (C) Beam rotation history from numerical simulation.

5.2. Setup for OMU

One of the RBS connections was instrumented to obtain the experimental moment-rotation behavior. The moment was derived using the force measured by the actuator load cell at the end of the beam. The relative rotation along the considered plastic hinge length in agreement with the numerical model was obtained using the instrumentation depicted in Figure 5. Two extension poles attached to the shear tab spanned the plastic hinge on top and bottom and were connected at the other end to the beam web. The relative deformation of each pole was measured by displacement transducers (CDP-50) with a resolution of 0.005 mm. The rotation of the RBS zone can be defined as:

$$\theta_{RBS} = \frac{d_{Bottom} - d_{Top}}{D_{up}} \tag{5.1}$$

where d_{Bottom} and d_{Top} are the deformation measurement for the bottom and top CDP, respectively, and D_{up} is the vertical distance between them.

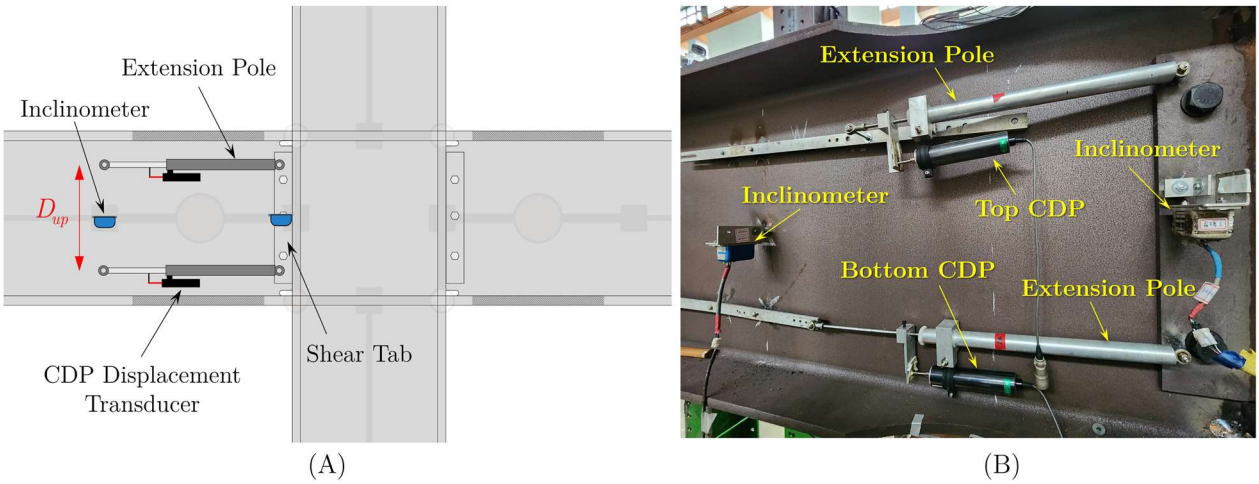

Figure 5.2: RBS rotation measurement setup scheme: (A) Diagram; (B) Photo of the test.

As an alternative, inclinometers were also fixed to both the shear tab and the end of the RBS section (see Figure 5) for a redundant measurement of the relative rotation. However, CDP setup provided cleaner data and was deemed the most reliable method for the rotation calculation. Figure 6 depicts a comparison of the raw data measured using the two sets of instruments. The feasibility of using string potentiometers as an alternative to CDP transducers was also explored, however, it was observed that string potentiometers exhibited a stagnant response under load reversal conditions and did not properly capture peak rotation values.

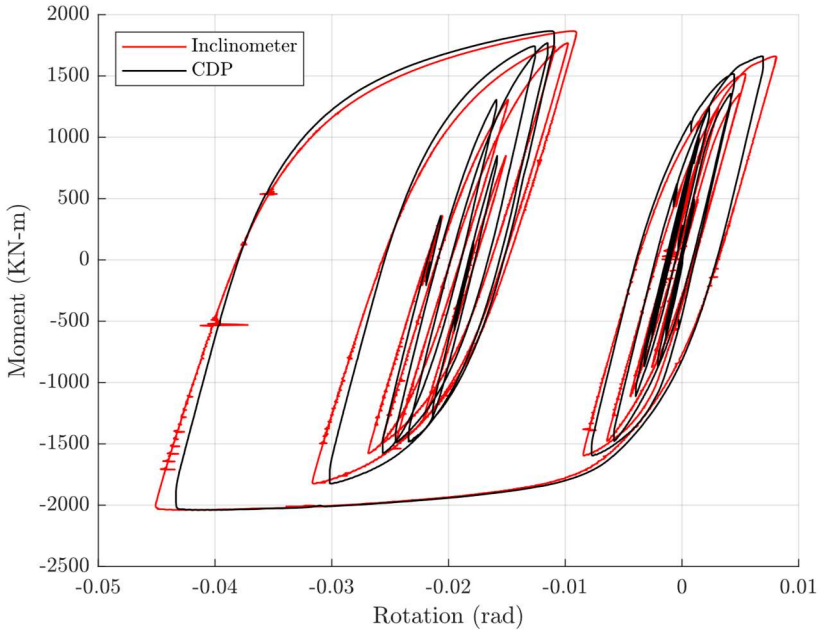

Figure 5.3: RBS rotation measurement for one of the tests comparing CDP setup and inclinometers.

5.3. Model Updating Methodology

During the HS, the Python-based OMU algorithm runs in parallel on the same computer as OpenSees and uses the measured beam response to improve the numerical model throughout the simulation (see Figure 3.10). The hysteretic RBS experimental response is characterized by the local rotation, velocity, and moment. OpenFresco computes the RBS rotation following Eq. (5.1), and the beam moment is calculated by multiplying the actuator force by the distance to the center of the RBS region, L_{RBS}. Given that both the RBS rotation (θ_{RBS}) and moment (M_{RBS}) are not part of the hybrid loop feedback, those signals are sent to OpenSees through a customized OpenFresco *Experimental Setup* as feedback forces and applied over dummy elements for further handling. Subsequently, the RBS response is transferred from OpenSees to the OMU algorithm each "updating step", defined as every other integration-step to avoid reaching the maximum buffer size

of the hardware used. The measured data is sent to the OMU algorithm via a web socket, which assures stability and high speed of the data transmission. This data is fed into the numerical hinge model for prediction of the moment response. Then predicted moment and the experimental data are compared, resulting in a successive refinement of parameters. The updated parameters, X, are then returned to OpenSees and used to update the numerical hinge model for all first-floor beams through the *updateParameter* OpenSees command[75].

5.3.1. Numerical hinge model

The numerical hinge models to be updated require the use of material models in OpenSees with updatable parameters. Two such material models were considered: the *IMKBilin* (IMK) and *BoucWen* (BW) uniaxial material models. Each model provides distinct advantages and limitations which impact their suitability for this specific application. The IMK model has the ability to capture more diverse features present in RBS behavior, such as stiffness and strength cyclic degradation or a sudden drop in the resisting force due to hinge fracture behavior. However, there are some drawbacks that limit its adaptability for OMU. For instance, the model is characterized by multiple linear segments that make it more difficult for the updating algorithm to converge at a consistent set of parameters. Additionally, as the error between measured data and the fitted model increases, the updating algorithm may not distinguish between a change within multi-linear segments or discrepancies between the existing numerical model and new data points. Moreover, the high number of parameters (24) and sensitivity of the model response to certain parameters (e.g. plastic rotation capacity) may limit the model from achieving a stable set of parameters.

In contrast, the BW model is continuous, and has less parameters that are more sensitive to the produced behavior. This model is capable of effectively capturing yielding, hysteresis

damping, and nonlinearity in the moment response. However, it does not inherently capture cyclic degradation behavior and sudden stiffness changes. Fortunately, some of these limitations can be overcome by the updating capabilities of the used algorithm. More importantly, it allows the OMU program to work on less parameters. Therefore, BW model is considered more suitable for implementing online model updating for the RBS in this study. This decision was supported by the results from initial quasi-static tests, where the limited strength and stiffness degradation was found well tracked by the model updating algorithm in the numerical simulations performed after the test.

The moment response of the BW model for this application is given by

$$M = \alpha K u + q_d z \tag{5.2}$$

$$\dot{z} = \frac{A\dot{u} - \beta|\dot{u}|z|z|^{n-1} - \gamma\dot{u}|z|^n}{u_y} \tag{5.3}$$

$$u_y = \frac{q_d}{K} \tag{5.4}$$

where u and M are rotation and moment of the element, K is the initial stiffness, q_d is the yielding moment, u_y is the yielding rotation, α is the ratio of the post-yield and elastic stiffness, and z is the hysteretic displacement. A, β, γ, n are shape factors. Setting A equal to 1 can reduce the redundancy in the model [76]. In this study, K, q_d, and α are selected as the updatable parameters, while A, β, γ, n , were considered less sensitive in capturing important changes in behavior and kept constant to avoid overfitting issues. The values for β and γ are 0.5 and 0.5. Therefore, the set of parameters to be updated every updating step is:

$$X = \{K, q_d, \alpha\} \tag{5.5}$$

5.3.2. Unscented Kalman Filter

The model updating is executed through the WACUKF [44] algorithm. This algorithm enhances the conventional unscented Kalman filter by embedding constraints in the unscented transformation, integrating weighting functions in the measurement transformation, and integrating adaptive noise matrix calculation in the state correction. The constraints curtail the parameter values to the physical range. In this test, the stiffness and yielding moment are assumed to be positive, and so constraints $K > 0$ and $q_d > 0$ are included. The weighting functions modulate the learning rate contingent on the load levels, promoting behavioral learning under larger rotations while maintaining existing features under smaller ones.

The covariance matrix $\boldsymbol{P}$, which signifies the uncertainty in the system's estimated states or parameters, is used in the UKF to generate new parameter samples. It is defined as a diagonal matrix where the first value represents the variability of the state variable z, while the remaining three values represent the variability of the parameters K, q_d, and α, respectively. The first entry in P is related to the calculated state z which has no uncertainty, as such it is given a small but non-zero value of 0.0001 for algorithm stability. Based on the experimental data obtained from the quasi-static test and experimental data from the literature, it was observed that parameters K and q_d may vary roughly 30% from their initial values. Parameter α may have values up to 0.01 and even in the negative range; since the initial guess α^o used in this study was smaller than such an expected variation, α^o was not used for the definition of matrix P. Thus, the initial covariance matrix P was defined as

$$P = diag\{0.0001, (0.3K^o)^2, (0.3q_d^o)^2, (0.01)^2\} \tag{5.6}$$

at the beginning of the simulation and was updated throughout.

The adaptive noise calculation bolsters the robustness of the UKF by fine-tuning the measurement and prediction covariances throughout the test. Thus, if larger noise is detected, the learning rates decrease, while if a larger discrepancy between predicted and measured forces is detected, the learning rates increase. This lessens the impact from the initial UKF parameter selection. A more detailed explanation of the WACUKF can be found in Cheng and Becker [44].

5.4. Selective Updating

In this study, OMU is applied in the HS of a full-scale moment frame structure with experimental data measured from one beam plastic hinge used to update eight representative elements in the numerical model. It is important to consider anomalies that can occur in the experiment and how the updated parameters for all numerical elements will be affected. For example, in one of the hybrid tests using a specimen A that already experienced yielding and local buckling at the column base and RBS zone, the beam bottom flange weld fractured resulting in a sudden drop in the moment capacity of around 30%. Similar strength reduction and slight post-fracture hardening are consistent with observations from other studies [77]. The parameter identification process captured this change through an abrupt adjustment. Figure 5.4 shows the weld fracture at 4 sec in the HS, the resulting RBS hysteretic behavior and the parameters identification during this test. Considering the unlikely occurrence that all beam bottom flanges would fracture at the same instance, it would not be appropriate to apply the updated parameters post-rupture to all second-floor beam hinges in the numerical model. Further, the weld fracture is less likely to occur when the top flange is in tension based on the better quality of the groove weld and the presence of composite slab [78]; thus, the direction of loading in the hinges (Figure 5.1C) should also be considered. To address this issue, a selective updating concept is proposed to

account for potential failure or other unexpected changes in the measured response not explicitly simulated in the element model. Selective updating is applied here to account for beam flange fracture during the OMU though the conceptual framework holds potential for broader applications.

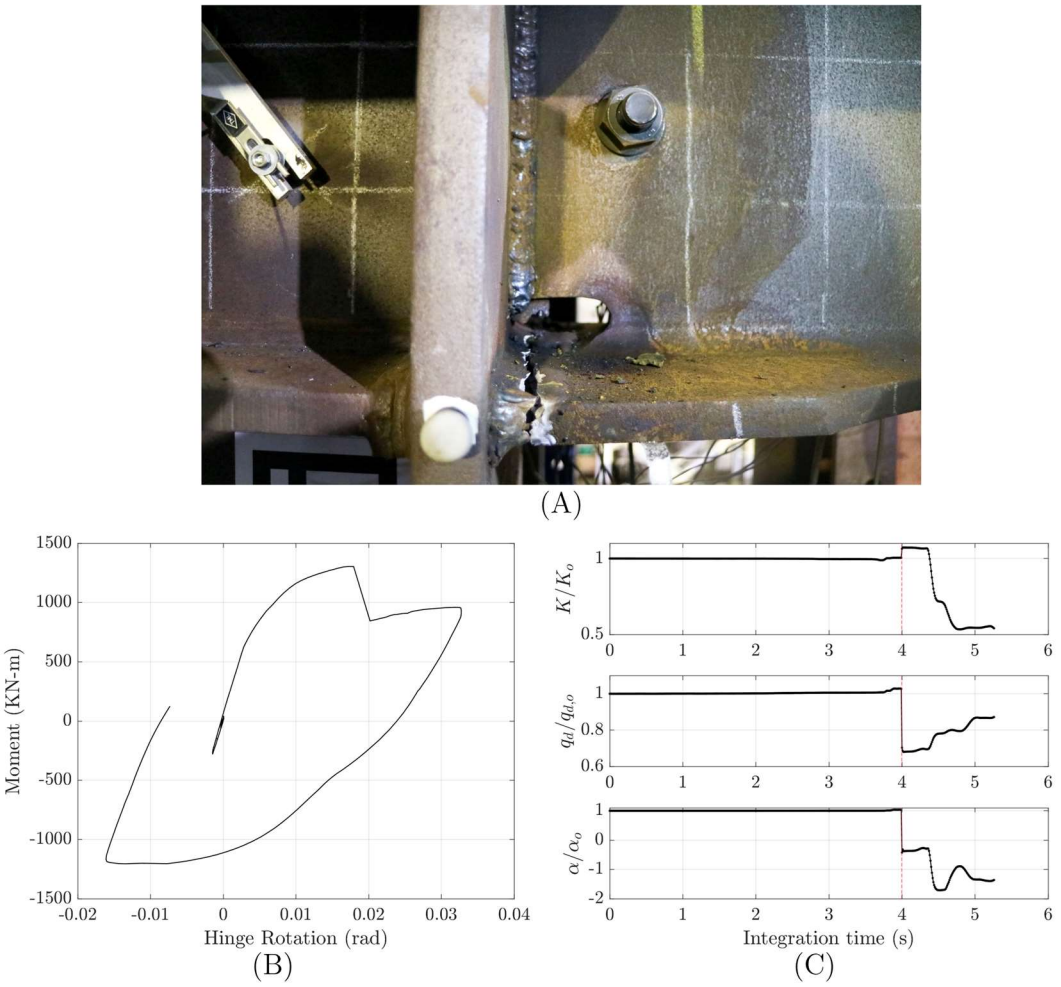

Figure 5.4: Beam flange fracture: (A) close-up to weld fracture; (B) RBS hysteretic response; (C) Identified parameters normalized by the initial value.

The primary objective of selective model updating is to update the numerical elements based on their individual demands. To achieve accurate fitting under heterogeneous element

demands, selective model updating preserves multiple sets of parameters to track various element states. At the beginning of the test, the experimental data can be used for model updating across all updating elements. The experimental element should experience the largest demands in order to update parameters to the level of loading experienced by the numerical models. Selective updating can initiate when damage is detected in the physical specimen. Conditions can be defined to trigger damage in the numerical elements and update properties accounting for the observed damage. Triggering rules can be deformation or force-related thresholds, for instance, the rotation at which fracture is expected to occur based on current measurements or previous data including a statistical distribution to vary response. Conditions based on measured data rely on detecting abrupt changes in behavior. A combination of both types of conditions is recommended to avoid "false-positive" damage detection. Numerical elements that have not reached the identified damage threshold receive parameters identified prior to the observed experimental damage. Conversely, numerical elements that have exceeded the threshold can be updated with post-damage (current) identified parameters.

Figure 5.5 shows the workflow of the selective model updating framework employed for this HS. The abnormal damage to be accounted for is the fracture of the bottom flange of the measured beam. The concept can be delineated in three main stages: *Event, Selection, Updating*:

- *Event Stage:* In this study, the triggering rules were defined based on experimental observations for fractured beams. The experimental results presented in Figure 8 depict a 32% strength reduction at 0.018 rad rotation after the fracture occurred in one of the specimens tested as part of this study. Based on this, two conditions were defined to detect fracture:

- The change between two consecutive identified strength parameters, ${q_d}^i - {q_d}^{i-1}$, shows a reduction of at least 25% with respect to the initial estimate ${q_d}^o$.
- The measured rotation ${\theta^i}_{RBS}$ is greater than 0.01 (rad). This rule was added to avoid a false-positive for identifying fracture too early.

When the two conditions are met, fracture is determined, and selective updating is initiated. The parameters identified obtained prior to fracture, X^{NF}, as well as the associated measured rotation, ${\theta^F}_{RBS}$, are saved. It is worth noting that the conditions for fracture detection can consider additional measured data including strain gauges or could also be guided by cumulative stress damage based on fracture theory [79].

- *Selection Stage:* For this HS, two rules were defined to identify the numerical hinges to be updated with fractured properties:
  - Since the physical beam being measured is located at the right side of the column, the data can only be used to determine fracture in the numerical beams undergoing similar demands considering asymmetric behavior (e.g., other beams on right side of column). It is assumed that fracture is more likely to occur when the bottom flange is in tension.
  - Only beams with a current rotation demand ${\theta^i}_{num}$ greater than ${\theta^F}_{RBS}$ (defined later) are selected to be considered as fractured beams.

  Selection of elements to update is evaluated at every updating step.

- *Updating Stage:* Numerical beams that are selected as fractured are updated directly with the current parameters obtained from the OMU, X^i. Those parameters track the properties

of the damaged beam, thereby simulating the consequential capacity reduction that can be based on experimental data for the specimen type being considered. In contrast, for the beams deemed unlikely to have experienced damage, the model parameters retain the values obtained prior to the initiation of fracture, X^{NF}.

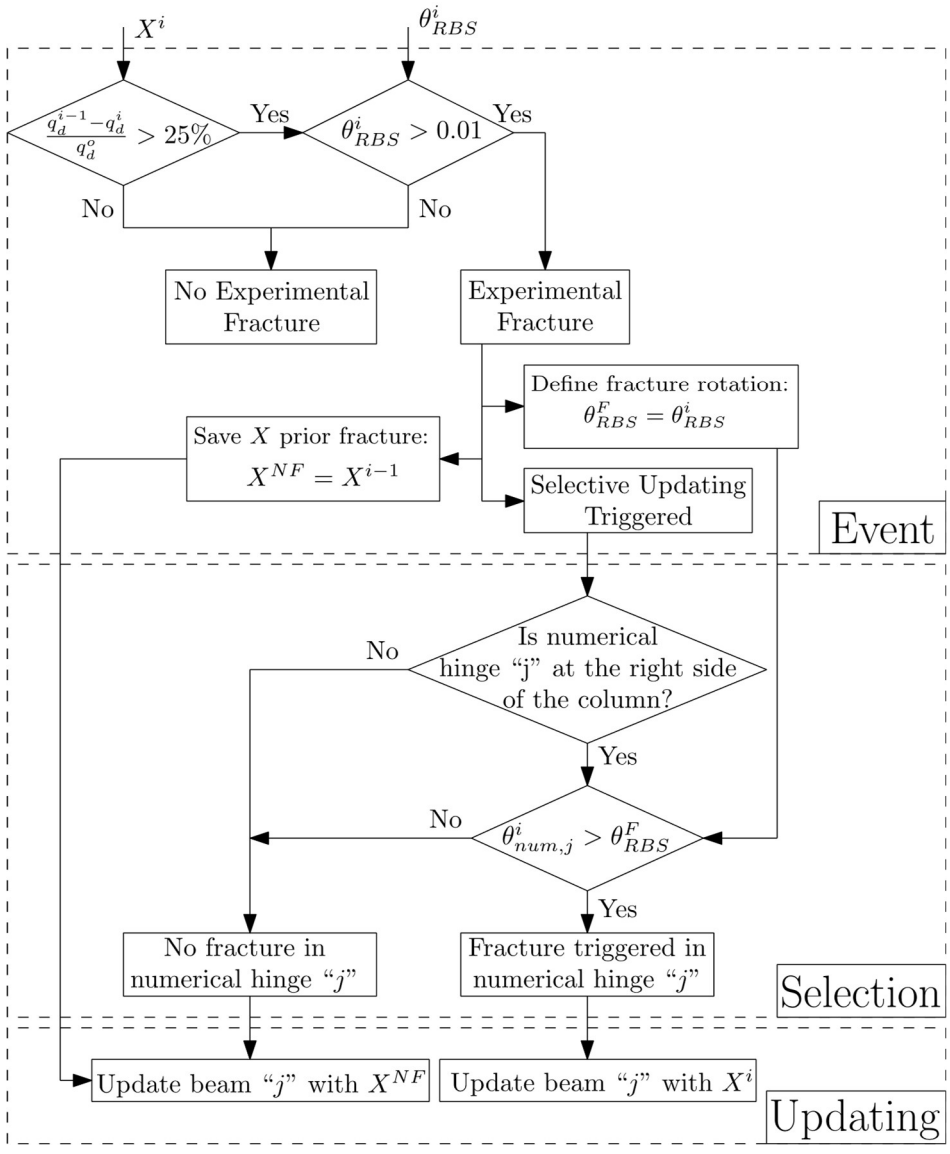

Figure 5.5: Workflow of the selective model updating.

Note that in this study, we propose a framework for selective updating, wherein the specific rules utilized at each stage are subject to potential improvement and modification. It is important to emphasize that these rules are specifically formulated for this particular test and should not be generalized. For instance, when considering the sampling rate of the updating process, the criterion based on the variation between two consecutive strength parameters might need to be reassessed. Additionally, depending on the particularities of the problem under study and the available measurements, more sophisticated rules could be implemented.

5.5. Experimental and Numerical Results

A series of four consecutive HS were conducted for each specimen A and B. The focus here is on the results of two hybrid tests and numerical studies using prototype building B (HS-B) to demonstrate the performance of the proposed OMU algorithm: Test "HS-B1" with one ground motion scaled for elastic level response; and test "HS-B2" conducted after HS-B1, with a loading sequence of two ground motions scaled first to Design Basis Earthquake (DBE) then followed by Maximum Considered Earthquake (MCE) intensity. After implementation of selective model updating, fracture was not observed in the experiments and the proposed method is further evaluated through virtual hybrid simulations.

5.5.1. Initial parameters selection

The initial parameters used for the BW model, called default parameters, were obtained following the recommendations of Lignos & Krawinkler [54] for the IMK model. The parameter

α was computed as the post-yielding stiffness ratio in the IMK model. Quasi-static tests of identical experimental subassemblies were performed prior to the HS with the data used to define "calibrated" parameters for the BW model. The parameters are summarized in

Table 5.1. The hybrid tests were conducted using the calibrated parameters for OMU, while the default parameters were employed for preliminary analysis and virtual HS performed afterward.

Table 5.1: Default and calibrated parameters for BW model

Parameter	Default	Calibrated
K (MM-m/rad)	300.19	400
q_d (MN-m)	2.178	2
α (%)	3.753	0.15

5.5.2. Experimental observations

Experimental results of the implementation of OMU within tests HS-B1 (elastic) and HS-B2 (DBE-MCE) are described in this section. Calibrated parameters were used as the initial parameters in the OMU. Figure 5.6 shows the measured RBS response with identified parameters, and Figure 5.7 depicts the numerical response of one of the updated numerical beam hinges. During test HS-B1, hysteretic behavior was observed (Figure 5.6A) mainly resulting from friction of the specimen against the lateral support and at the actuator swivels. Despite that, the identified parameters (Figure 5.6C) did not show significant variations from the initial parameters. This was because of the minimal difference observed between the measured and predicted values, coupled with the small range of rotational displacement in the specimen. These factors led the algorithm to

conclude that the hysteretic loop in the experimental data holds negligible importance and can be disregarded. Therefore, numerical updated hinges exhibited mainly linear behavior. Figure 5.7A illustrates the hinge response for HS-B1 test of the numerical beam located at the right side of the numerical center column (Hinge 5).

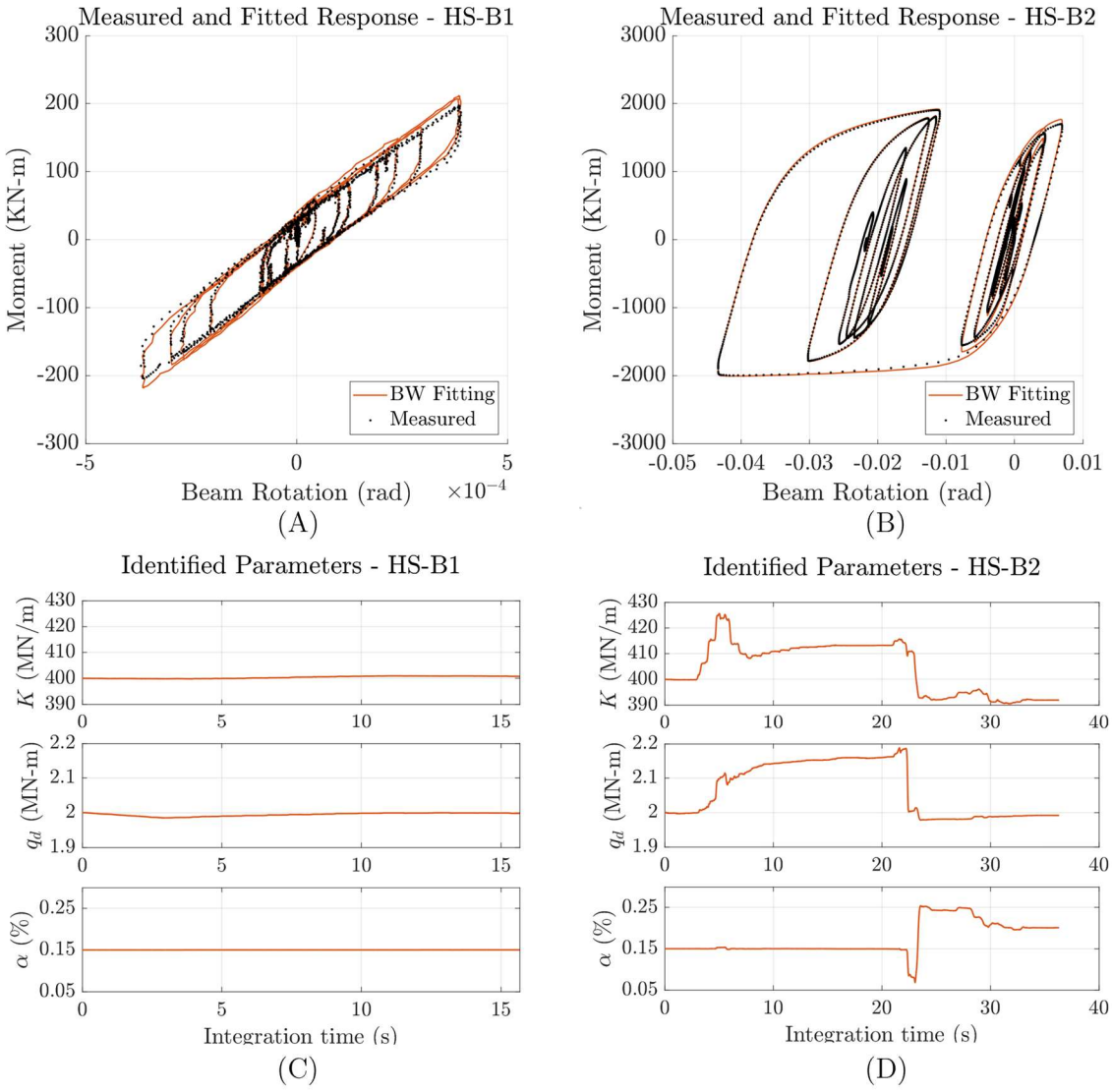

Figure 5.6: Model updating experimental results: (A) Measured and fitted response for test HS-B1; (B) Measured and fitted response for test HS-B2; (C) Parameters for test HS-B1; (D) Parameters for test HS-B2.

For HS-B2, the measured hinge response showed a well-defined hysteretic loop due to yielding at the RBS (Figure 5.6B). The model updating algorithm was able to track the hinge response by using the parameters observed in Figure 5.6D. Although the identified parameter q_d changed quickly during HS-B2 (up to 11% of q_d^o), the selective updating algorithm was not activated, as the instantaneous delta was below the 25% q_d^o threshold. Figure 5.7B illustrates the response of the numerical hinge 5 updated with the identified parameters. The updated hinge exhibits a behavior similar to the measured response.

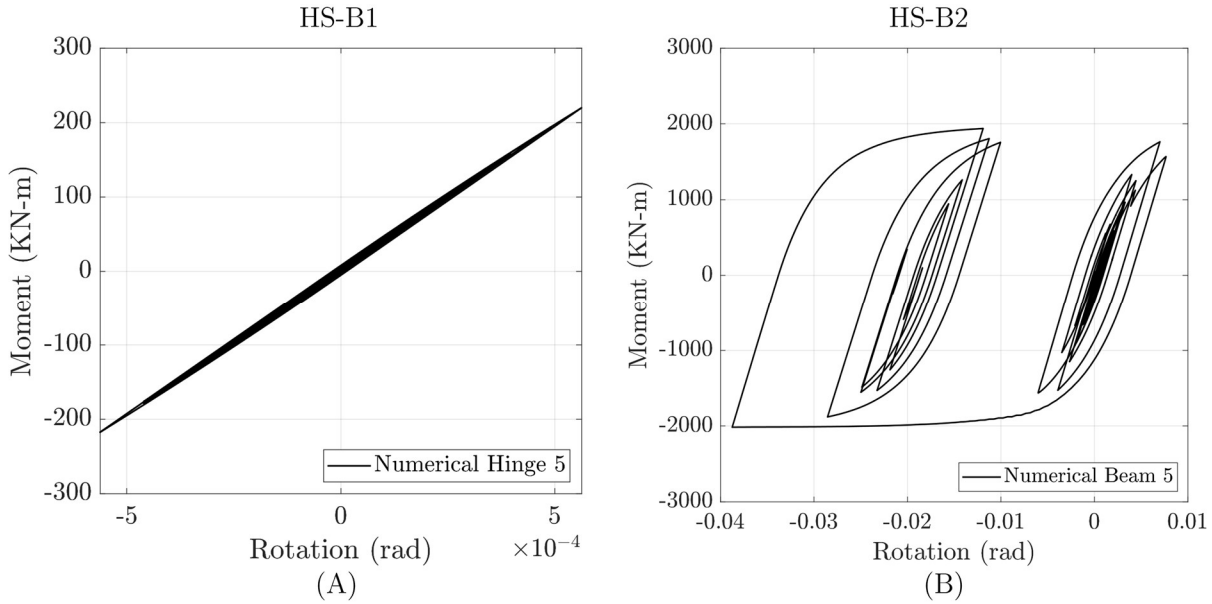

Figure 5.7: Updated hinge results during the HS: (A) Hinge 5, test HS-B1; (B) Hinge 5, test HS-B2.

5.5.3. Initial parameters sensitivity

The initial parameters used during the tests were obtained from model calibration using data from quasi-static tests performed on nominally identical specimens before the HS. Especially for large scale testing, similar data may not always be available. To assess the sensitivity of the

OMU algorithm to the initial parameter selection, the BW model is used to replicate the measured response by applying both the default and calibrated parameters listed in Table 5.1 as the initial parameters in the OMU. The comparisons that follow include cases in which the default or calibrated parameters are maintained throughout the simulation (labeled as *Default* and *Calibrated*, respectively) and where both are used as the initial parameters in the OMU algorithm (labeled as *Default+OMU* and *Calibrated+OMU*, respectively).

Figure 5.8 shows the measured and calculated response using BW with the four parameter sets listed in Table 3 summarizing their performance. The performance is quantified using the NRMS error defined in Eq.(4.8), where Y_{target} represents the measured moment, and Y_{num} is the computed value of the moment from the simulation using the selected parameter cases.

Comparing both cases without updating, the calibrated parameters provided better tracking of the measured response as expected. Nevertheless, when OMU is employed, both cases provided enhanced tracking performance regardless of the initial parameters (see Table 5.2). As seen in Figure 5.8A and C, when the rotational demands are very small, there is very little change in the model parameters. However, with OMU, there is significantly more energy dissipation. This is because during OMU, the calculated state z is also updated to account for discrepancies between the loading on the experimental element and the numerical element. Figure 5.8D shows that both OMU cases converge to different parameter sets, yet they provide similar performance. Therefore, even when it is desirable to account for calibrated values, the use of parameters obtained from the literature nonetheless provides a satisfactory response when using the proposed OMU algorithm.

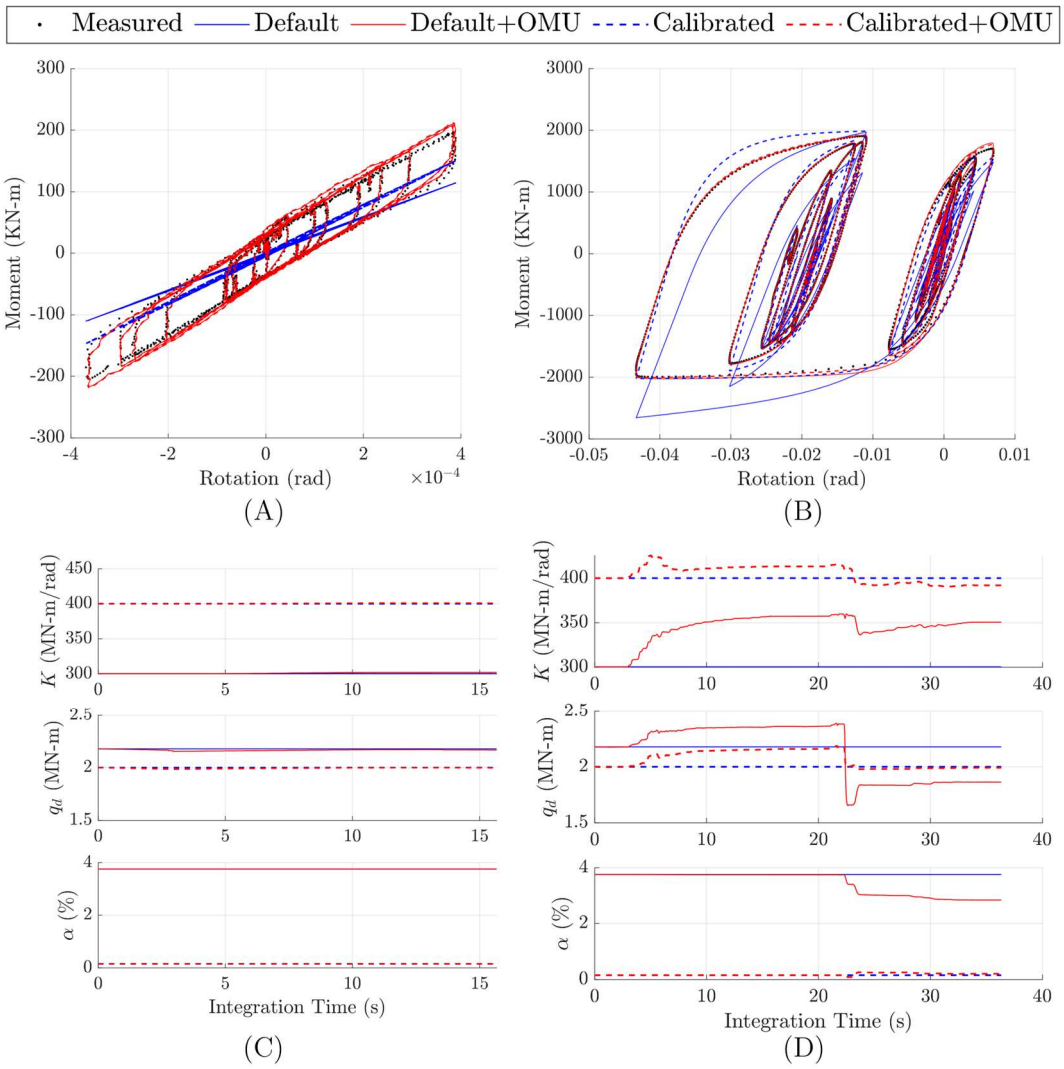

Figure 5.8: Parameter sensitivity: (A) Beam response for HS-B1 test; (B) Beam response for HS-B2 test; (C) Parameter history for HS-B1 test; (D) Parameter history for HS-B2 test.

Table 5.2: NRMS error between measured and simulated response: parameter sensitivity

Case\Test	HS-B1	HS-B2
Default	50.60%	37.50%
Default+OMU	7.50%	3.50%
Calibrated	38.80%	13.40%
Calibrated+OMU	7.70%	3.00%

5.5.4. Hinge models with and without OMU

The previous section assessed the agreement between the measured hinge response with BW model using different initial parameters. To more clearly assess if OMU improves the reliability of a simple BW model in capturing the plastic hinge response compared to the IMK model with fixed parameters, further numerical studies are carried out. In Figure 5.9, the measured hysteretic response from test HS-B2 is compared with the results from the OMU algorithm with calibrated initial parameters, the IMK model employing the default parameters, and the IMK applying calibrated parameters obtained from the quasi-static tests. Additionally, the response of one of the updated beams of the numerical substructure is compared with the IMK responses using the same rotation history to represent what the numerical beam response would be if OMU had not been used.

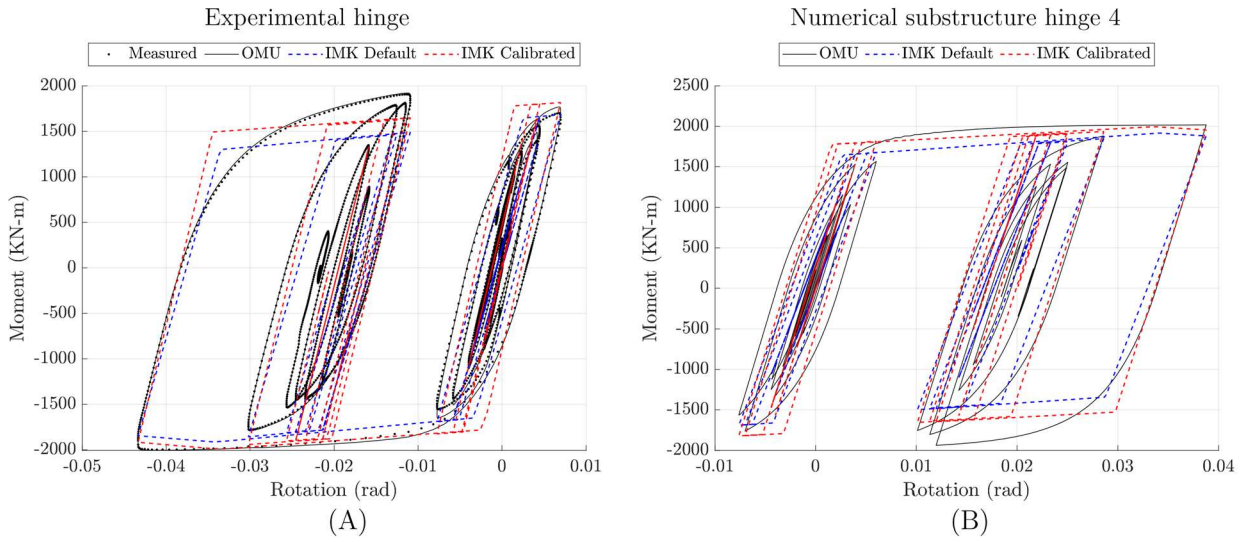

Figure 5.9: Comparison between OMU and IMK with default and calibrated parameters under HS-B2: (A) Measured hinge response; (B) Numerical substructure hinge 4 response.

From Figure 5.9A it can be inferred that the calibrated IMK parameters improve the ability to capture the RBS response compared with the default parameters, as expected, for this specific specimen. Nonetheless, despite the complexity of the IMK model, the BW model using only 3 updatable parameters provides a better response compared to the measured behavior. This difference is most evident in the positive moment near -0.015(rad) of rotation, after unloading from the peak negative rotation. The corresponding NRMS errors respect to the measured response are 3%, 50.2%, and 41.8%, for OMU, IMK with default parameters, and IMK with calibrated parameters, respectively. For the hinge in the numerical substructure (Figure 5.9B), although there is no experimental value to validate against, the OMU response follows the trend between the default and calibrated IMK models which all align with the behavior pattern seen in the experimental substructure. Overall, the Bouc-Wen model with 3 updatable parameters provided better tracking of the measured response compared with the offline IMK, even in presence of strength changes due to a combination of cyclic degradation and isotropic hardening.

5.5.5. Effects of selective updating on element behavior

The selective updating approach was developed and implemented following the beam fracture during the fourth consecutive hybrid test carried out on prototype A, called “HS-A4” test. However, fracture was not observed in the tests that followed the HS-A4 test to be able to evaluate this framework in an actual HS. Post-test simulations and analysis are used to demonstrate the features of selective updating. Figure 5.10 plots the measured data of the fractured beam from test HS-A4, the identified response (OMU), and the response of two beam hinges being updated within the numerical substructure. Numerical “Hinge 5” is located at the right side of the column,

corresponding to the same location the measured beam hinge, and “Hinge 4” located at the opposite side, as shown in Figure 5.10B. As can be seen, both Hinges 4 and 5 modeled the loss in strength seen in the physical specimen where the bottom flange fractured. However, only numerical Hinge 5 had the bottom flange in tension when the specimen is deformed towards the right side, while Hinge 4 had the bottom flange in compression, and thus, not likely to fracture. Therefore, the selective updating rules were applied to the measured data of HS-A4 in postprocessing, after the test was conducted (dashed line in Figure 5.10).

Figure 5.11 shows the time history of the parameters for both Hinges 4 and 5 from HS-A4 (X^i) and the set obtained in postprocessing from virtual HS with selective updating. An identified drop in strength of 32.4% triggered the selective updating algorithm. At this instance, there is a clear difference between Hinge 4 updated with the set X^i and the response obtained by applying selective updating that considers asymmetric behavior. For this case highlighted here, Hinge 4 is not likely to fracture at the same instance as Hinge 5 and does not reach a comparable rotation in the opposite direction that would lead to similar tension demands on the lower flange. If selective updating was applied during the actual test, the rotation history of Hinge 4 should change due to the coupling between the global and local response.

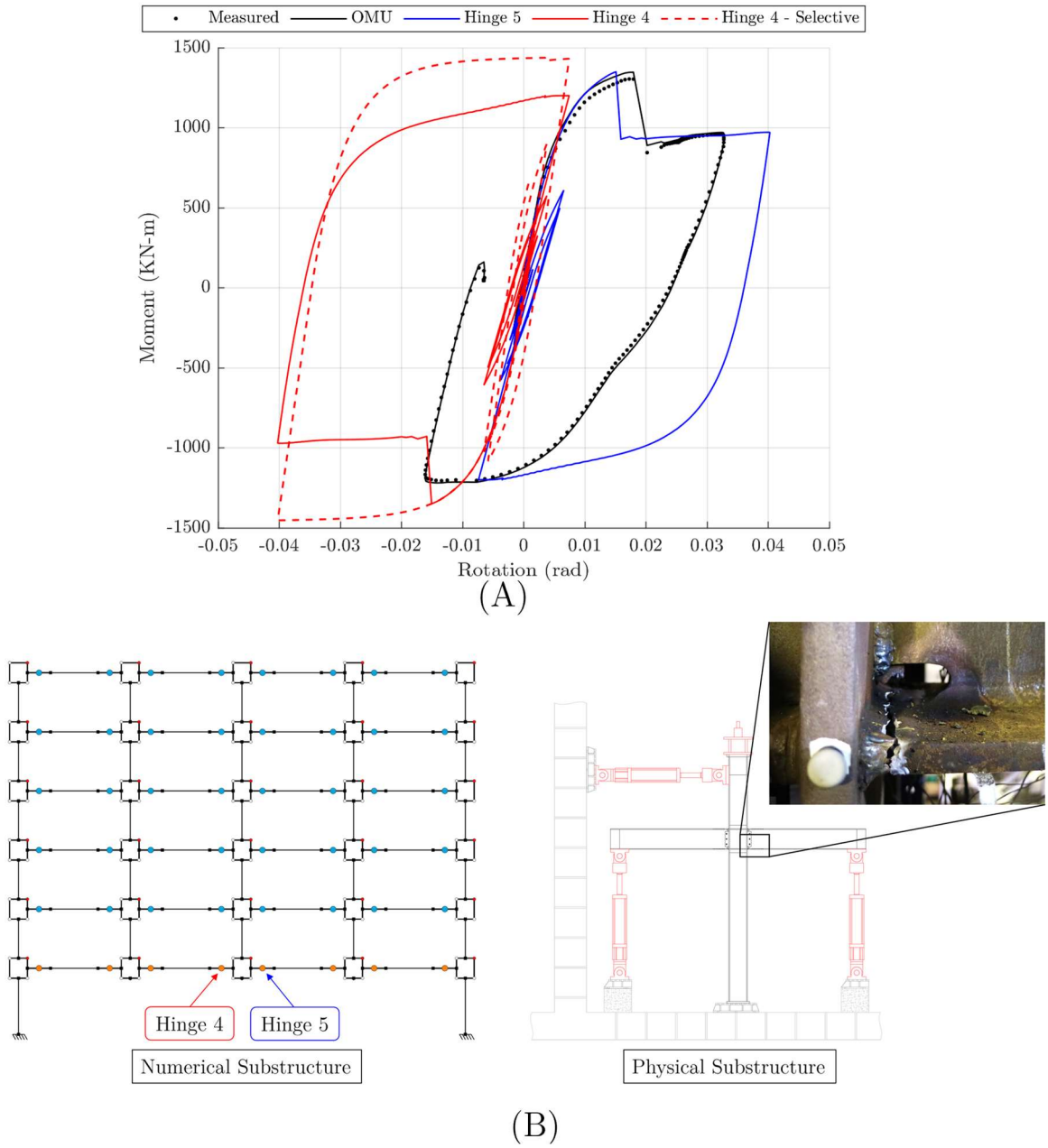

Figure 5.10: Selective model updating results from the numerical simulation test.

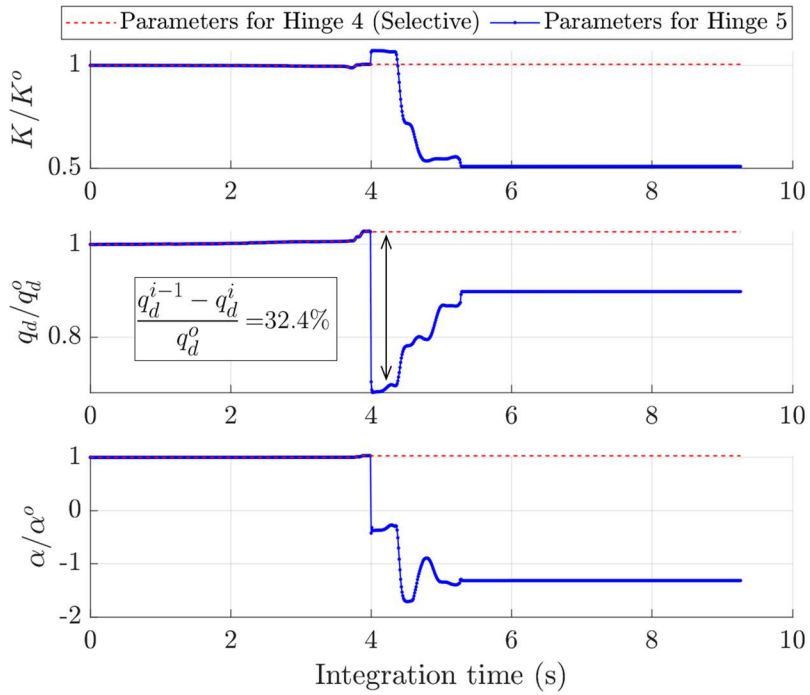

Figure 5.11: Normalized parameters with and without selective update approach.

5.5.6. System level response sensitivity

The numerical beam hinge models with the OMU algorithm affect the distribution of forces to the surrounding elements and the global level response. This section presents additional numerical studies to further evaluate the effects OMU and selective updating on the system level behavior of the frame. Virtual hybrid simulations, (also known as "FE-Software Coupling" [80]) were conducted using Prototype B with the same numerical substructure model used in the actual HS, but with the physical specimen replaced with a separate representative model in OpenSees [18]. In the virtual specimen, the modeling approach was similar to the numerical substructure (see Figure 3.10B), utilizing a BW model with constant parameters obtained at the end of HS-B2 test for the virtual beam hinges.

For the first comparison, the difference of the first and second story drift response with and without OMU was assessed. For the case without OMU, all beam hinges in the numerical substructure were simulated using the calibrated IMK model, since this model is able to capture the complex behavior of the frame using constant parameters. For the case with OMU, the procedure described in Section 5.5.3, using the initial parameters, was used. The first and second story drift ratio of the frame are illustrated in Figure 5.12. A minor difference between the two analyzed cases can be observed for both stories, having NRMS error of 6.8% and 12.3% for first and second story, respectively.

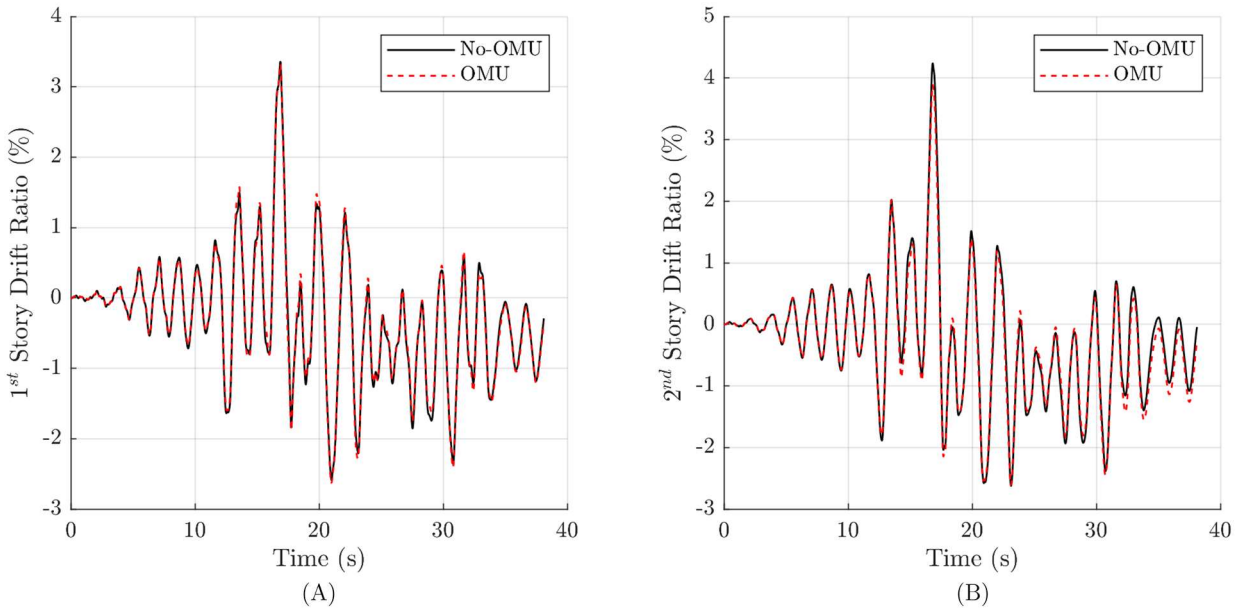

Figure 5.12: Story drift of the frame with and without OMU: (A) First floor; (B) Second floor.

One of the key aspects to be assessed in this study was the column behavior. Therefore, a good agreement at the boundary conditions of the first story column is desirable between the numerical and experimental substructures. Since an overlap substructuring method was employed

for these tests, the overlapped DOFs between both substructures are similar, but not necessarily identical. In this regard, the first story horizontal displacement and axial load over the column were enforced to be the same between the numerical and experimental substructure [59], while the rotation of the top end of the first story column was not controlled. In light of this, OMU improves the experimental and numerical column boundary conditions by having the numerical beam behavior resemble the experimental beams. Figure 5.13 compares the local beam response and column rotation within the virtual-experiment and numerical substructures. The beam hysteresis presents a better agreement when OMU is implemented. Such improvement has an impact on the boundary conditions of the column, which exhibits a better agreement in terms of the column rotation history (Figure 5.13C and D). Particularly, the NRMS errors for the column rotation are 25.9% without OMU, and 11.7% when OMU is employed. In terms of the maximum rotation, the ratio of the numerical over the experimental is 1.22 and 1.06, with and without OMU, respectively.

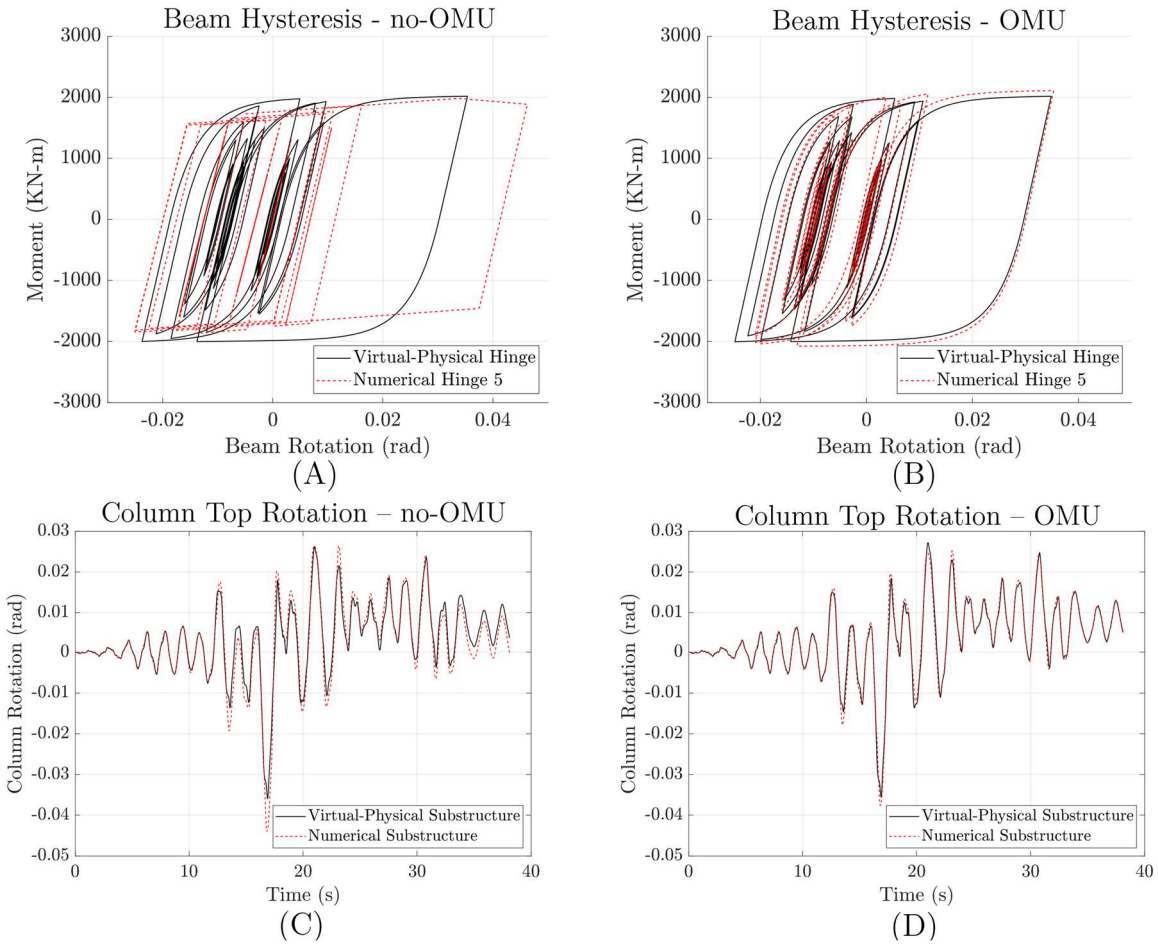

Figure 5.13: Local response in the virtual-experiment and numerical substructure: (A) Beam hysteresis without OMU; (B) Beam hysteresis with OMU; (C) Top-end column rotation without OMU; (D) Top-end column rotation with OMU.

To assess the impact of the selective updating over the system level response, virtual HS is carried out simulating a fractured hinge, called "virtual hinge". The BW virtual hinge parameters are updated at 0.02 rad rotation, reducing the strength and stiffness by 35% to simulate bottom flange fracture. Three cases are compared: with and without OMU as before, and with OMU and selective updating. The virtual hinge experiencing fracture and numerical hinge hysteresis are depicted in Figure 5.14 for the three cases. When OMU was not included, the IMK did not consider any change due to fracture. When conventional OMU is employed (Figure 5.14(b)), all beam

hinges experienced a change in the identified parameters due to the fracture phenomenon. Since updated hinges experienced a slightly smaller rotation demand compared to the physical beam, numerical beams simulate fracture at a rotation smaller than 0.02 rad. When the selective update approach is incorporated (Figure 5.14C), only the Hing 5 (the right hinge) is updated with the current parameters, while Hing 4 (the left hinge) kept using the parameters obtained prior to fracture was triggered. Furthermore, Hinge 5 employed the parameters related to fracture only after a rotation of 0.02 rad, which corresponds to the predetermined threshold for initiating the simulated fracture. From Figure 5.15 it can be observed that there is a change in the first and second-story drift ratio depending on which approach is employed. Table 5.3 presents the difference in the peak story drift of each case normalized by the peak observed when selective update is included. Values are shown for the first and second story. It can be observed that by including the selective update approach there was a difference of around 7% for the first story. A more important effect can be observed at the second story with up to 15% difference.

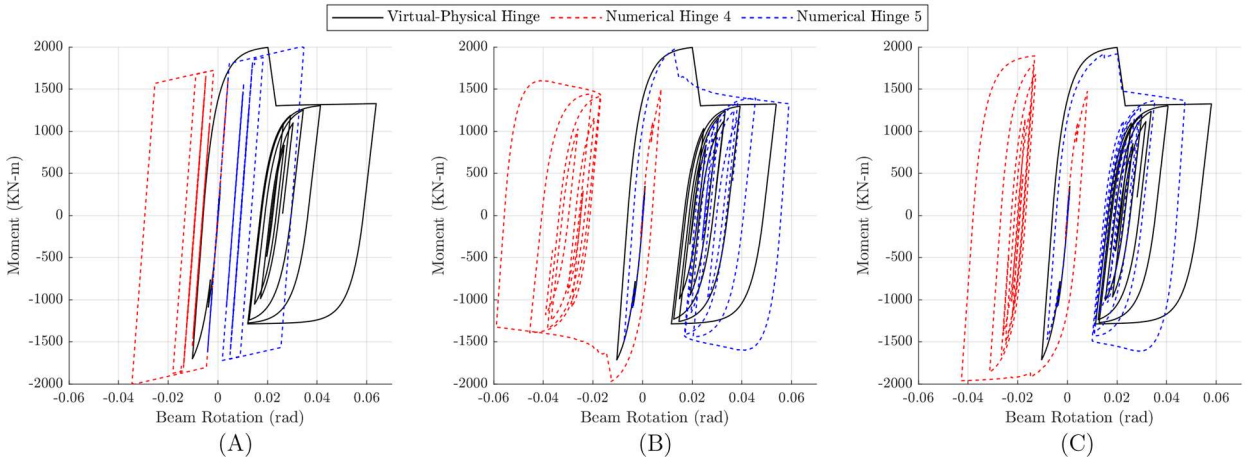

Figure 5.14: Hinge response of virtual-physical fractured and numerical beams: (A) No-OMU; (B) OMU; (C) OMU including Selective update.

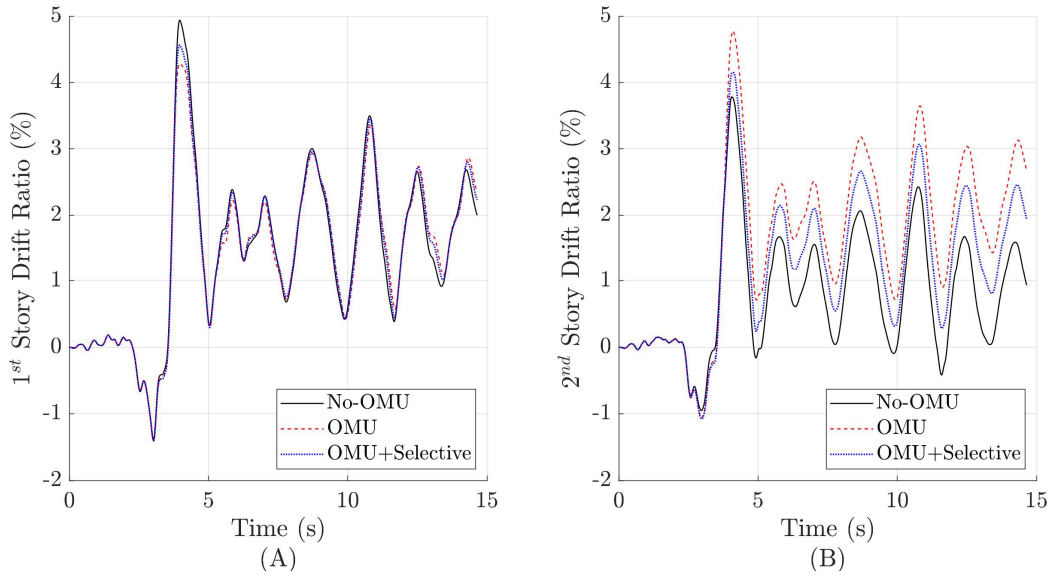

Figure 5.15: Global frame response by implementing no-OMU, OMU, and OMU plus Selective updating: (A) 1st story drift ratio; (B) 2nd story drift ratio.

Table 5.3: Peak drift ratio normalized by the peak found using OMU plus selective updating.

Case	1st Story	2nd Story
No-OMU / OMU+Selective	8.0%	-8.9%
OMU / OMU+Selective	-6.2%	+15.0%

5.6. Acknowledgements

Chapter 5, in part, has been submitted for publication of the material as it may appear in "Selective online model updating in hybrid simulation of a full-scale steel moment frame" C. Sepulveda, M. Cheng, T. Becker, G. Mosqueda, K.J. Wang, P.C. Huang, C.W. Huang, C.M. Uang, C.C. Chou: *Earthquake Engineering and Structural Dynamics*. The dissertation author was the primary researcher and author of this paper.

Chapter 6 Column Hinge Macro-Element with Shortening

This chapter presents the development of a column section macro-element to simulate column shortening by building on the commonly used plastic hinge zone with fiber-based elements to simulate both moment response and column buckling using an effective material. In the axial direction, shortening is modeled utilizing an empirical expression based on experimental observations. These two components are packaged in a hinge macro-element and included in an OpenSees frame model to assess the structural response for different ground motions.

6.1. Empirical Models for Axial Shortening

Axial shortening due to column buckling is a complex phenomenon that cannot be easily predicted. Different studies have shown that deep wide flange column buckling can be simulated through high fidelity finite element (FE) models [81–83]. However, its computational cost has limited applications to simulations of whole frame structure especially to observe response under various ground motions records and intensities. Previous studies have proposed expressions to assess the expected axial shortening (Δ_{axial}) of steel columns experiencing buckling in a more

efficient manner via empirical formulas. MacRae [62] proposed one of the first expressions assuming a linear relationship between the Δ_{axial} and the cumulative plastic rotation (θ_{lp}), axial load (P), and web-to-gross area ratio (A/A_w):

$$\begin{aligned} \Delta_{axial}[mm] &= 0.446\frac{P}{2.54P_y}\frac{A}{A_w}L_p\sum\theta_{lp} \qquad for\ \frac{P}{P_y} \le \frac{2.54A_w}{A} \\ \Delta_{axial}[mm] &= 0.446L_{PH}\sum\theta_{lp} \qquad for\ \frac{P}{P_y} > \frac{2.54A_w}{A} \end{aligned} \tag{6.1}$$

However, later studies showed that this relationship is not linear [4,63]. Elkady and Lignos [63] developed a nonlinear expression using a regression method, calibrated against a dataset of Δ_{axial} derived from high fidelity FE models:

$$\Delta_{axial}[mm] = 13.62 \cdot \Sigma\theta_{lp}^{1.596}\left(\frac{h}{t_w}\right)^{0.769}\left(1-\frac{P_g}{P_y}\right)^{-1.819} \tag{6.2}$$

This expression includes the cumulative plastic rotation, column web slenderness ratio, h/t_w, the effect of axial load due the gravity-induced forces and adding nonlinearity through individual exponent to each term. Ozkula et al. [64] proposed another formula following a similar approach but employing the cumulative hysteretic energy dissipated at the plastic hinge zone. The formula was obtained using a dataset of Δ_{axial} from both member tests on full-scale specimens, and simulated data using high fidelity FE models [11]:

$$\Delta_{axial} = \frac{PL_p}{EA}e^{\beta\eta} \tag{6.3}$$

The expression uses the elastic deformation of the plastic hinge length (L_p), multiplied by an exponential function that account for sectional properties and axial load effect through the coefficient β, and the hysteretic energy dissipated at the hinge zone, η, defined as:

$$\beta = C\left(\frac{h}{t_w}\right)^{1.56}\left(1-\frac{P_u}{P_y}\right)^{-2.1} \tag{6.4}$$

$$\eta = \frac{1}{M_p}\int M d\theta \tag{6.5}$$

where the parameter C account for the buckling mode, taken as 0.028 for anti-symmetric local buckling, and 0.022 for coupled buckling [83]. The parameter η is called "normalized energy" since it computes the dissipated energy through the integral of the column moment along the column drift ratio and normalized by the plastic moment M_p. The advantage of this formula is the use of experimental data and expanding the applicability to not only local buckling but other buckling modes. Nonetheless, there are some limitations to extend this expression for use within a model of a frame structure. For instance, all these formulas are meant to be used for constant axial forces. Therefore, any force variation due to axial force redistribution after differential column settlement needs to be addressed.

6.2. Empirical Model for Axial Shortening with Time-Varying Input Parameters

Building on the previous studies, an alternative empirical expression is proposed to predict axial shortening due to column buckling suitable for time-varying input parameters. The formula proposed by Ozkula et al. [64] is taken as baseline since it was derived from an extensive experimental program of full-scale deep columns of around one story height, together with the additional factor C that accounts for different buckling modes. The factor β that considers the axial load and web slenderness remain the same, but with the axial load varying over the time:

$$\beta_i = C\left(\frac{h}{t_w}\right)^{1.56}\left(1-\frac{P_i}{P_y}\right)^{-2.1} \tag{6.6}$$

The concept of normalized dissipated energy is maintained, with the plastic moment replaced by the reduced plastic moment, M_{pc}, dependent on the axial load [83]:

$$M_{pc} = 1.18\left(1 - \left|\frac{P_i}{P_y}\right|\right) F_y Z_x \tag{6.7}$$

with Z_x the plastic section modulus and F_y the nominal steel stress. To better quantify the loading history, the terms M_{pc} and β_i are included inside the integral to weight each energy increment. Then, the total weighted energy is quantified with the term E_t defined as

$$E_t = \int \beta_i \frac{M_i}{M_{pc}} d\theta \tag{6.8}$$

where M_i is the column moment at each analysis step, and θ the hinge rotation assumed equal to the story drift angle. To remove the elastic stored energy from the total weighted energy E_t, the original normalized hysteretic energy η is redefined as the total weighted energy minus the elastic stored energy weighted by the current β_i:

$$\eta_i = E_t - \frac{M_i^2}{2K_e M_{pc}} \beta_i \tag{6.9}$$

where K_e is the elastic loading/unloading bending stiffness of the column consistent with M_i and θ, and the subindex i is added to refer a "time-varying normalized and weighted dissipated energy", η_i. For simplicity, from now on η_i can be referred to as "normalized dissipated energy". The parameter K_e can be taken as constant for simplicity, neglecting any cyclic degradation. Figure 6.1 illustrates both the total energy and elastic stored energy.

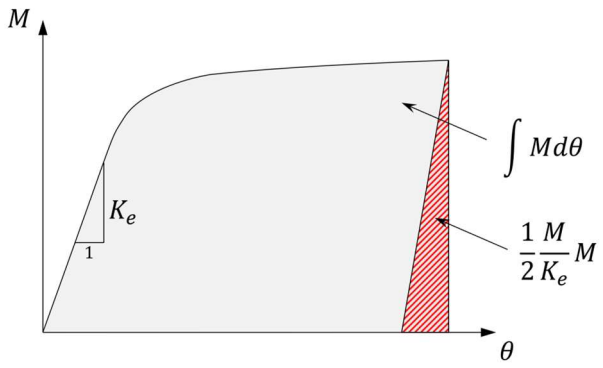

Figure 6.1: Total energy and elastic stored energy.

Note that in Eq. (6.9) only E_t is being accumulated every analysis step, while the elastic stored energy is an instantaneous value. Finally, the exponential function of Eq. (6.3) is replaced by the following expression, representing the inelastic shortening:

$$\Delta_{axial} = \alpha \eta_i^{1.7} \tag{6.10}$$

with constant α obtained from linear regression. The exponent 1.7 was defined since it optimized the linearity between measured Δ_{axial} and computed η_i from the experimental data described later. It is difficult separate the Δ_{axial} components attributable to steel yielding and column buckling from the experimental data. Therefore, this expression accounts for both inelastic sources of shortening. While the column remains within the elastic range, the normalized dissipated energy $\eta_i = 0$, and the inelastic shortening $\Delta_{axial} = 0$.

Subassembly and member level tests were used to obtain the parameter α. Subassembly data is obtained from the quasi-static and hybrid test presented in this study. Isolated column tests data are obtained from the experimental program conducted in 2017 [4,11]. Note that among the member level test data available, only W24x131 and W24x176 columns were considered to focus on the column sections studied herein. Nevertheless, the expression could be generalized for more

sections in future studies. Test ID for subassembly tests are listed in Table 3.2. For member level tests, the term "Iso" refers to isolated column test; the next term specifies the axial force, being "L" for low, "M" for medium and "Var" for varying axial load; and the last letter denotates the column section. Since test ID IsoM-B was conducted twice (defined as "1M" and "11M" in the original reference [4]), de second one was denotated as IsoM-B(r). Table 6.1 details the information of each test used in this chapter, including load pattern, axial load (based on Eq. (3.2)), and reference.

Table 6.1: Test data used for the empirical expression calibration.

Column Section	Test ID	Test Type	Load Pattern	Axial Load (C_a)	Reference
W24x131	Q-A	Subassembly	Quasi-static	0.2	Chapter 3
W24x131	HS-A	Subassembly	Hybrid Simulation	0.2	Chapter 3
W24x131	IsoL-A	Isolated	Quasi-static	0.16	Ozkula et al. [4]
W24x131	IsoM-A	Isolated	Quasi-static	0.33	Ozkula et al. [4]
W24x176	Q-B	Subassembly	Quasi-static	0.4	Chapter 3
W24x176	HS-B	Subassembly	Hybrid Simulation	0.2-0.4	Chapter 3
W24x176	IsoM-B	Isolated	Quasi-static	0.33	Ozkula et al. [4]
W24x176	IsoM-B(r)	Isolated	Quasi-static	0.33	Ozkula et al. [4]
W24x176	IsoVar-B	Isolated	Quasi-static	0.27-0.54	Ozkula et al. [4]

For each test, the parameter η_i was computed at every time step. Figure 6.2 illustrates the η_i history of test IsoL-A as example. Then, a linear regression was used to obtain the α value that best represent the trend. A weighting vector equal to Δ_{axial} was added to the linear regression to prioritize the larger values and minimize the importance of nearly-zero values. The rigid body component of the measured deformation was removed from all tests. The column-end moment was computed including the second order effect due to the axial force for member-level tests. Axial load was not included to compute column-end moment for subassembly since the axial force is

aligned with the column rotated position. Figure 6.3 illustrates the range of the available data, having both column sections, axial loads ranging from C_a=16.4% up to 54%, drift ratio up to 4%, and axial shortening up to 120 (mm).

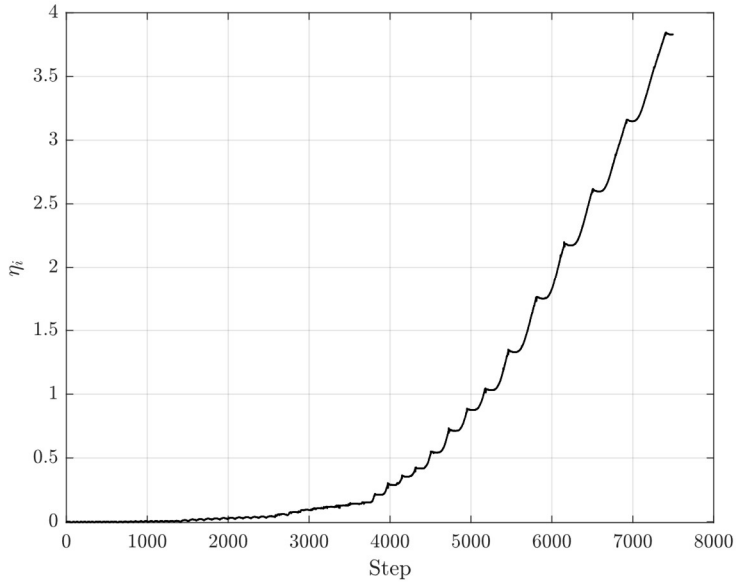

Figure 6.2: η_i history of test IsoL-A.

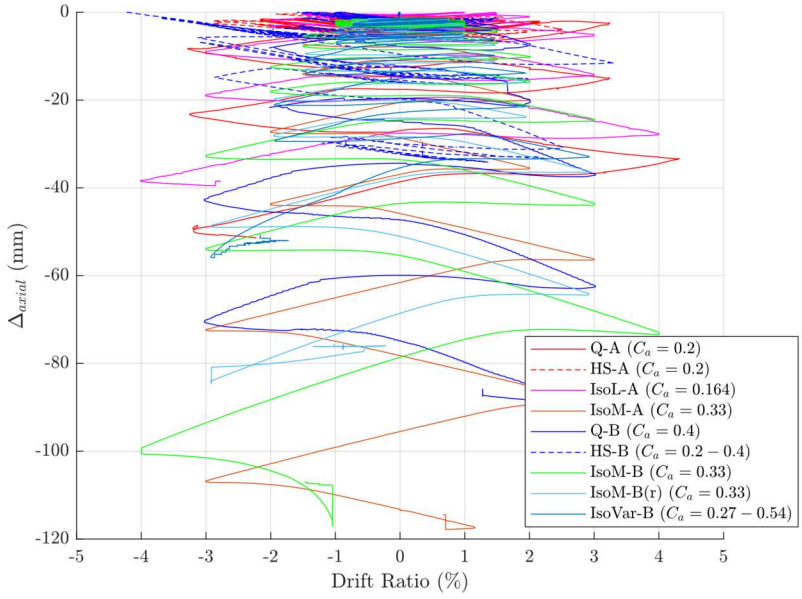

Figure 6.3: Axial shortening versus drift ratio for the analyzed test.

The weighted linear regression provided a factor $\alpha = 4.13$ (mm) for Eq.(6.10). A separated coefficient of $\alpha = 2.84$ (mm) was estimated for test IsoVar-B that had variable cyclic axial load imposed. The smaller α value suggests that the cyclic axial load pattern delays the observed Δ_{axial} for the same energy dissipated and average axial load, as reported by other researchers as well [4,84]. The smaller coefficient can be used for columns with cyclic axial load variation like exterior columns in moment frames or columns of a braced frame. Nonetheless, further analysis is required to generalize this observation including more experimental and simulated data of specimens with varying axial load. Figure 6.4 illustrates the measured and estimated values of Δ_{axial}.

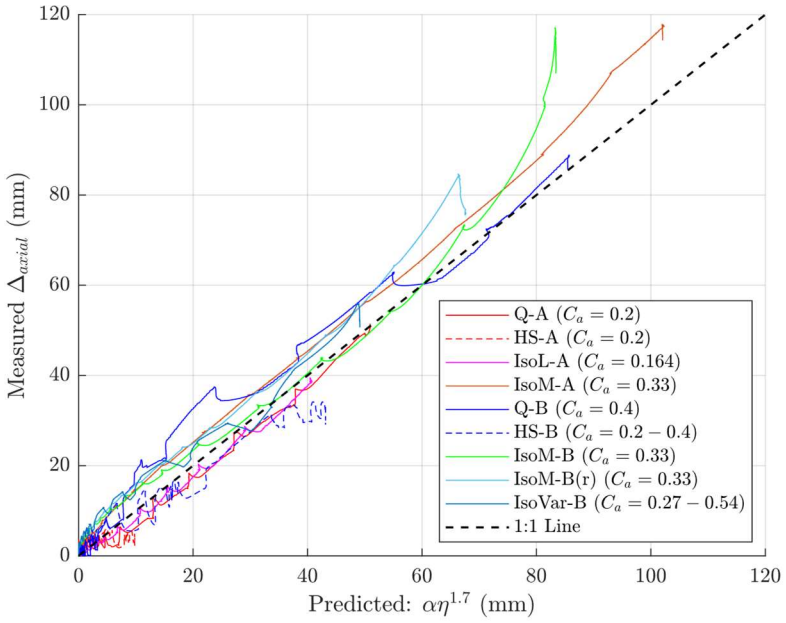

Figure 6.4: Linear regression fitting of measured Δ_{axial}.

6.3. Column Hinge Macro-Element

To implement the shortening expression defined in the previous section, the column element should be able to simulate the degrading response due to column buckling. Distributed

plasticity elements using fiber-based sections are commonly used to efficiently model frame structures using displacement-based (DB) or force-based (FB) elements. In DB elements, the element stiffness is computed by enforcing the deformation distribution along the beam-column element. In contrast, FB elements prioritizes force equilibrium along the beam-column element to calculate the element flexibility matrix [85]. Both formulations can capture the axial-flexure coupling including material nonlinearity. However, due to the assumption of "plane sections remain plane", only element-level geometric nonlinearity can be captured. Therefore, local buckling or lateral-tortional buckling cannot be explicitly simulated using the traditional formulations.

Previous studies have proposed alternatives to simulate local buckling with fiber-based elements utilizing effective materials. Kolwankar et al. [86,87] proposed the used of fiber-based elements to simulate the local buckling degrading response of wide-flange steel members through an effective material including a negative stiffness branch in compression. They propose relationships to compute the effective material constitutive law based on the geometry of the section and material properties. It is well-documented that the use of uniaxial material models with negative stiffness induce a nonobjective response due to localization issues [88,89]. To overcome this mesh-dependency problem, Kolwankar et al. proposed a new type of distributed plasticity element including a nonlocal formulation. The approach shows good agreement for axial-bending response and even axial shortening estimation. However, the authors mention that this formulation is meant to simulate only local buckling, with lateral-tortional or coupled buckling being out of scope. Maity et al. [90] proposed a displacement-based element to simulate coupled buckling using multiaxial fibers and additional kinematic relationships to capture the axial, flexural, shear, and torsional interactions at the sectional level. Although it provides promising results, it is still under

development, being tested for monotonic loads only, and using a symmetric plasticity model which is not consistent with the non-symmetric tension-compression nature of buckling phenomenon. While these previous studies proposed new element formulations that are actually developed within an opensource platform like OpenSees, they are not yet publicly available. A more accessible approach is proposed by Alghossoon and Varma [91] using the same idea of effective material but within a traditional displacement-based element. This method also matches well with the beam flexure response experiencing local buckling. However, they do not address the element response under combined bending and compression loads, nor does it evaluate the axial shortening. In this study, a more practical approach is proposed to capture the axial-flexure response of wide-flange beam-column elements using fiber-based elements, while the empirical expression proposed in the previous section is used to enforce the expected axial shortening. These components are packaged within a hinge macro-element for easy implementation.

To capture the required features of a wide-flange column response under combined axial-bending loads, the column member is separated into different elements, each one accounting for different aspect of the column behavior. Figure 6.5 illustrates a schematic of the modeling approach, with elements labeled as A, B and C. Element A represent the length of the column that may experience inelastic behavior without buckling. This zone can be modeled through a distributed plasticity element, or an elastic beam-column element if preferred. Element B represents the "plastic hinge zone" expected to exhibit buckling. It is composed by a displacement-based element with two Gauss-Lobatto integration points, effective uniaxial material with negative stiffness in compression described above, and a length equal to the plastic hinge zone, L_p. In this study L_p is defined equal to the column section depth, however a more refined expression can be used instead. Even though this approach has shown to struggle with localization problems, this

issue take place at element level for DB elements, and not at section level as for FB elements. Therefore, using one single DB element concentrates the degrading response within the expected plastic length, an approach demonstrated to provide good results by others [90,91].

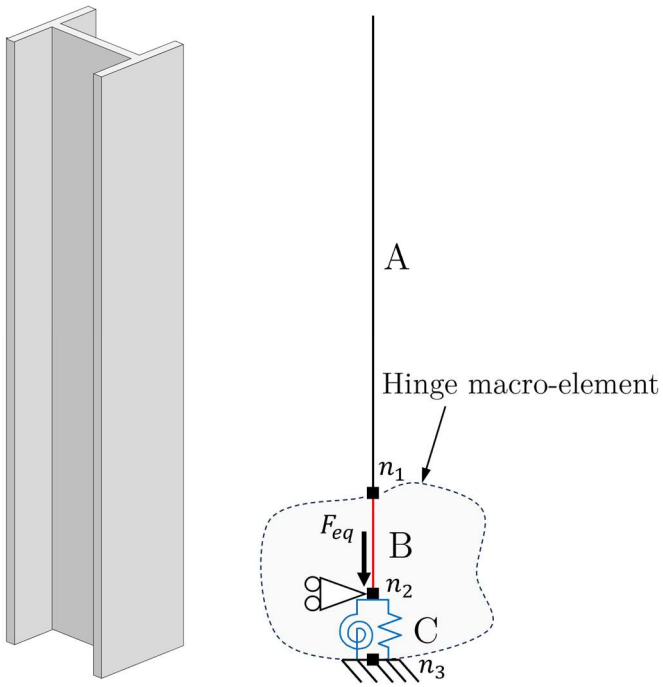

Figure 6.5: Macro-element scheme.

Element C is responsible for providing the buckling-related vertical displacement that element B does not capture. It is composed of a vertical stiffness, K_{sh}, to handle the vertical behavior, and a rotational stiffness, K_θ, in case the base plate or foundation flexibility needs to be included. Since there is no horizontal stiffness, this direction is constraint at node n_2 for a fixed node n_3.

An external nodal force F_{eq} is applied at node n_2 to enforce the desired vertical displacement. This approach follows the same concept of the equivalent force-control approach proposed by Wang et al. [61] and Sepulveda et al. [59] to enforce displacement compatibility in

hybrid simulation. In this method, a large stiffness is added at the constrained degree of freedom, which in this case is K_{sh} in the vertical direction. Then, a force is computed such that the nodal displacement converges to the target displacement, working in a similar way to the penalty method [92]. In this study, the equivalent force is computed as

$$F_{eq} = \left(\alpha\eta_i^{1.7} - \Delta_{p,B}\right)K_{sh} \tag{6.11}$$

The plastic deformation of the element B, $\Delta_{p,B}$, is subtracted because the empirical expression of Eq.(6.10) already account for it. The inelastic component of B can be estimated as the total deformation of B, Δ_B, minus the elastic component,

$$\Delta_{p,B} = \Delta_B - P_i\frac{L_p}{EA} \tag{6.12}$$

where L_p is the length of element B, EA it the elastic sectional stiffness, and P_i is the axial load taken by element B each integration step.

6.4. Implementation in a Building Model

The column hinge macro-element is implemented in the full frame model used for hybrid simulation of archetypes A and B in Chapter 3. A plastic hinge length is defined equal to the column section depth. A detailed definition of the model components are described next.

The hinge macro-element requires the definition of a material model with a negative stiffness branch for element B, and the stiffness coefficients K_{sh} and K_θ for element C. The material model Ibarra-Medina-Krawinkler (IMK) [53] was used as effective steel material to define the fibers of element B. A schematic of the effective material used in this study is shown in Figure 6.6. In the tension side, the material has a linear-elastic behavior until the yield point, with

yield strain ε_y, yield stress σ_y and Young's modulus of the steel E_s. After yielding the stiffness changes to bE_s, with b the post-yielding stiffness ratio, taken as $b = 0.01$. After reaching the ultimate stress, σ_u, defined as $1.3\sigma_y$, the stress remains constant. The compression side is composed by four branches. The material has an elastic behavior up to the yield point, after which it exhibits the same post-yielding stiffness as in tension. The material keeps hardening until reaching the capping stress, σ_{cap}, defined by Kolwankar et al. [87] as

$$\sigma_{cap} = 1.1\sigma_u - 2.17\frac{b_f}{2t_w} \quad \text{(MPa)} \tag{6.13}$$

Upon achieving this stress level, the effective material exhibits negative stiffness, leading to a decrease in stress until reaching the residual stress and strain values, σ_{res} and ε_{res}. This point is defined by Kolwankar et al. [87] as follows:

$$\sigma_{res} = Max\left(\sigma_y - 1.44\frac{b_f}{2t_w}; 0.0\right) \quad \text{(MPa)} \tag{6.14}$$

$$\varepsilon_{res} = Max\left(0.15 - 0.014\frac{b_f}{2t_w}; \frac{\sigma_y}{E_s} + \frac{\sigma_{cap} - \sigma_y}{bE_s}\right) \tag{6.15}$$

Beyond the point $(\varepsilon_{res}, \sigma_{res})$, Kolwankar et al. proposes another negative stiffness branch. Instead, Alghossoon and Varma [91] use a constant behavior. This study assumes a constant residual stress for the last branch, based on numerical simulations suggesting better agreement with the experimental data.

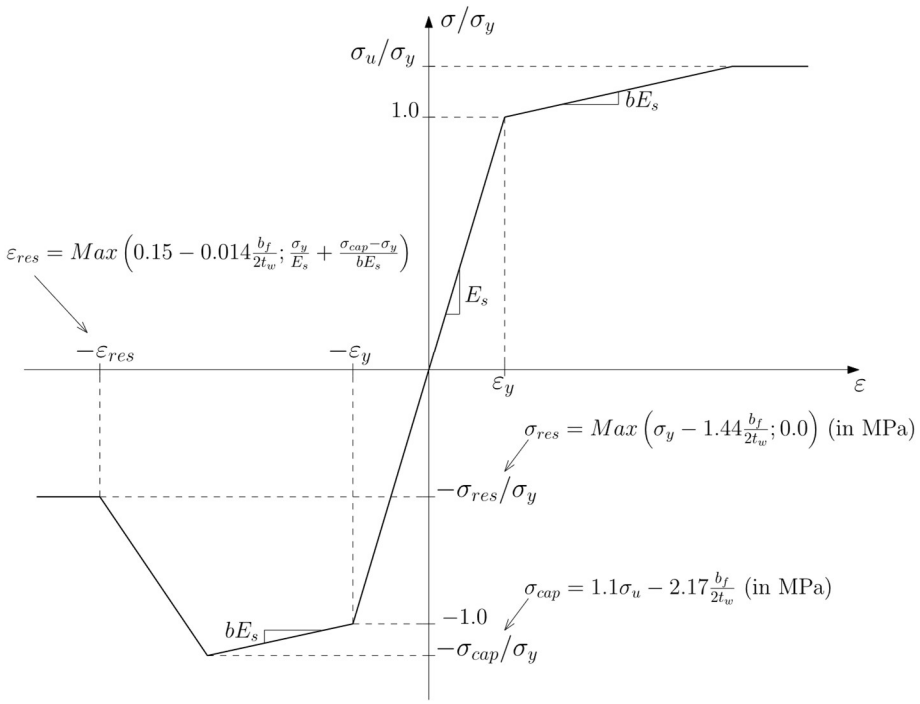

Figure 6.6: Effective material model.

The previous expressions are applied for column sections of archetype A and B considering the material properties σ_y and E_s measured from coupon tests. The backbone curves obtained for both columns are shown in Figure 6.7.

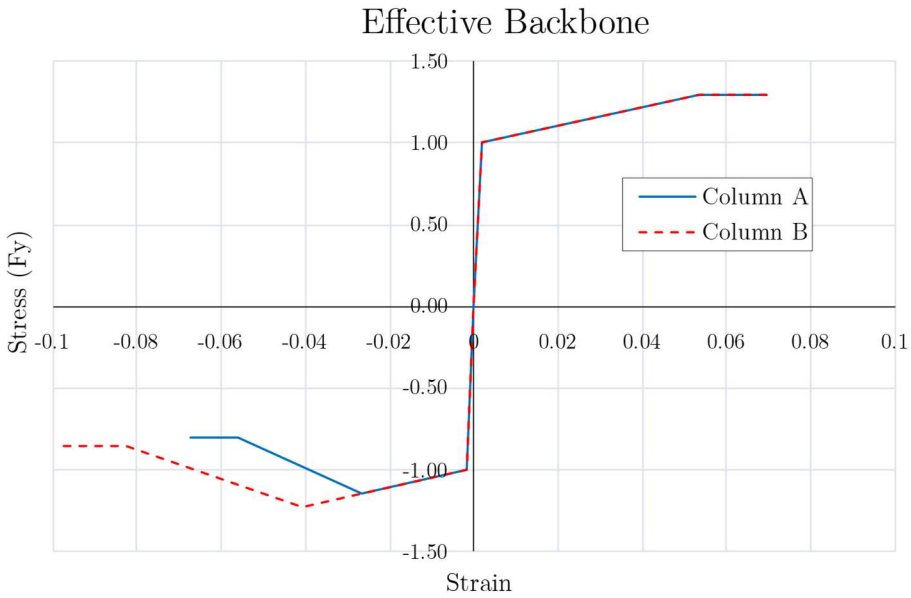

Figure 6.7: Effective material model for column A and B.

The stiffness coefficient K_{sh} is defined as 100 times the elastic axial stiffness of the column hinge,

$$K_{sh} = 100\frac{EA}{L_p} \tag{6.16}$$

considered sufficiently large compared to the stiffness of the rest of the elements.

The stiffness K_θ was obtained from experimental data. Figure 6.8A depicts the two displacement transducers located at the bottom of both column flanges, which were used to estimate the base rotation as

$$\theta_{base} = \frac{(u_{north} - u_{south})}{d_{col}} \tag{6.17}$$

with u_{north} and u_{south} the measured displacement for the north and south transducers, respectively, and d_{col} the horizontal distance between them equal to the column depth. Figure 6.8B

shows the moment-rotation plot of the base plate during test QS-B, including a linear fit to represent the response. The stiffness obtained was $K_\theta = 370$ MN-m/rad. Since the base plate was nominally the same for all specimens, the stiffness K_θ for both archetypes is computed from test QS-B. Both K_{sh} and K_θ were incorporated to the hinge macro-element using a *zerolegth* OpenSees element [17].

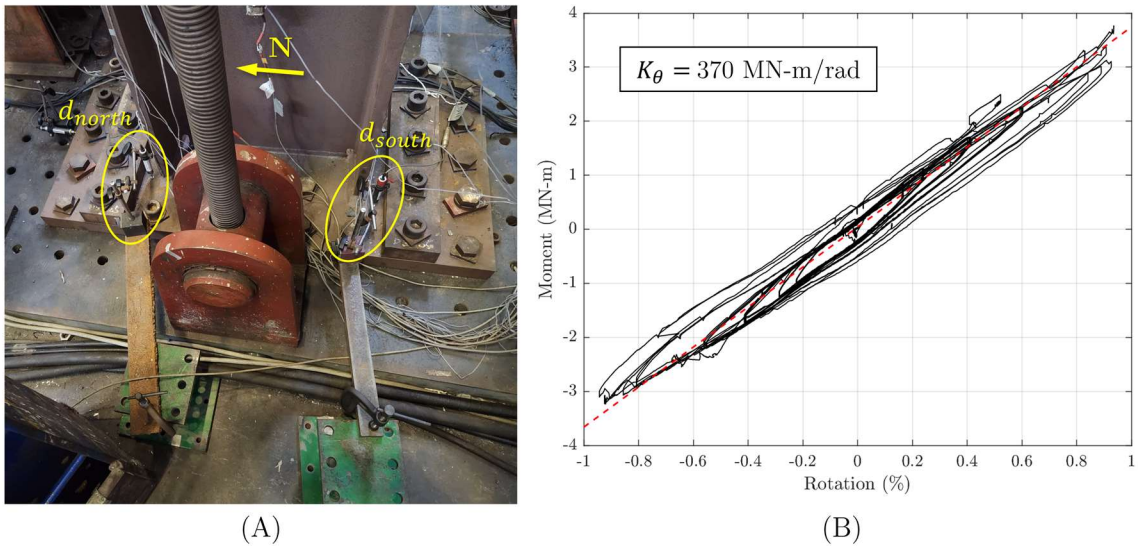

(A) (B)

Figure 6.8: Base plate rotation: (A) Measurement setup; (B) Moment-rotational response (test QS-B).

Once the material properties were defined, the numerical models used for the hybrid tests were modified to replace the plastic hinge length at the base of the first story column elements with hinge macro-elements. Figure 6.9 illustrates the frame building model including the hinge macro-elements.

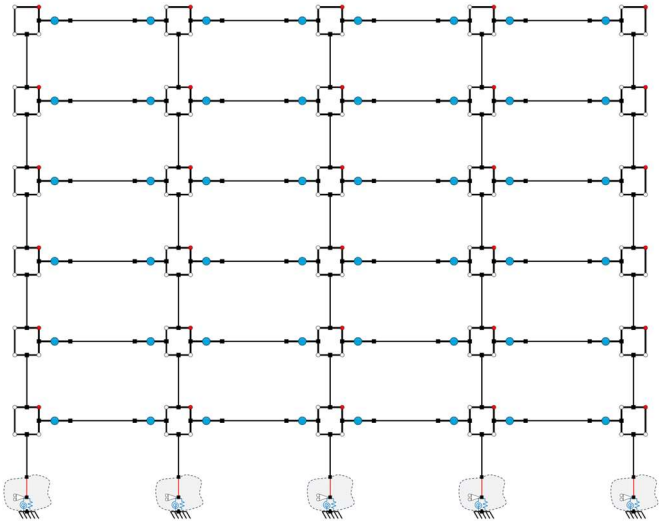

Figure 6.9: Nonlinear model of the frame building including hinge macro-elements.

The experimental response of tests HS-A2 and HS-B2 is compared to the results from a purely numerical simulation that includes the hinge macro-element. The numerical simulation effectively captured the essence of the experimental response.

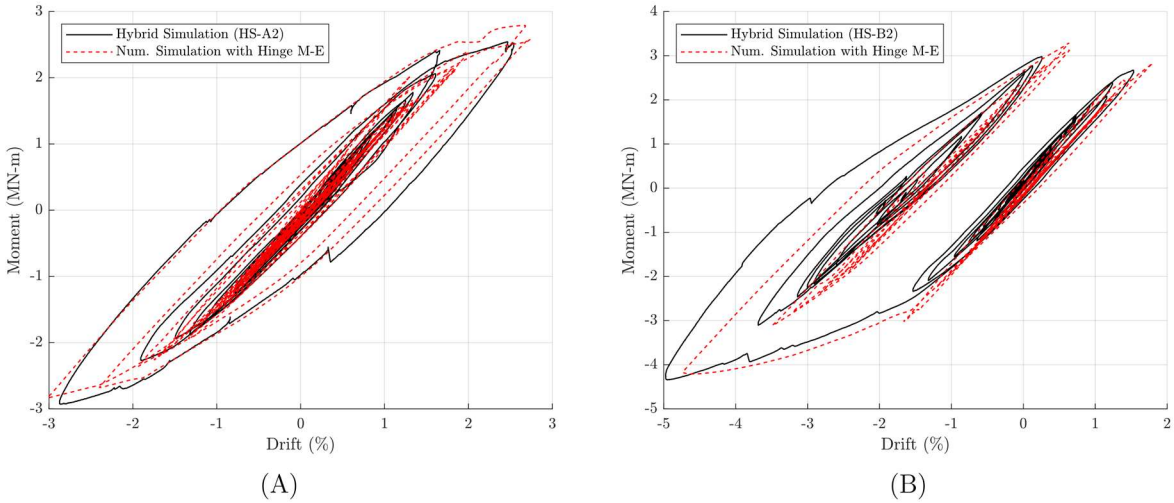

Figure 6.10: Column moment response from hybrid tests and numerical simulation: (A) HS-A2; (B) HS-B2.

As it can be seen from Figure 6.4, the proposed empirical formula provides larger relative errors for small values of Δ_{axial}. Since Δ_{axial} measured during HS-A2 and HS-B2 were small, the empirical expression cannot accurately predict them, as observed in Figure 6.11. However, since buckling-related scenarios are associated to large values of Δ_{axial}, this aspect is not seen as an issue. Further analyses with different ground motion and axial load levels are shown in the next section.

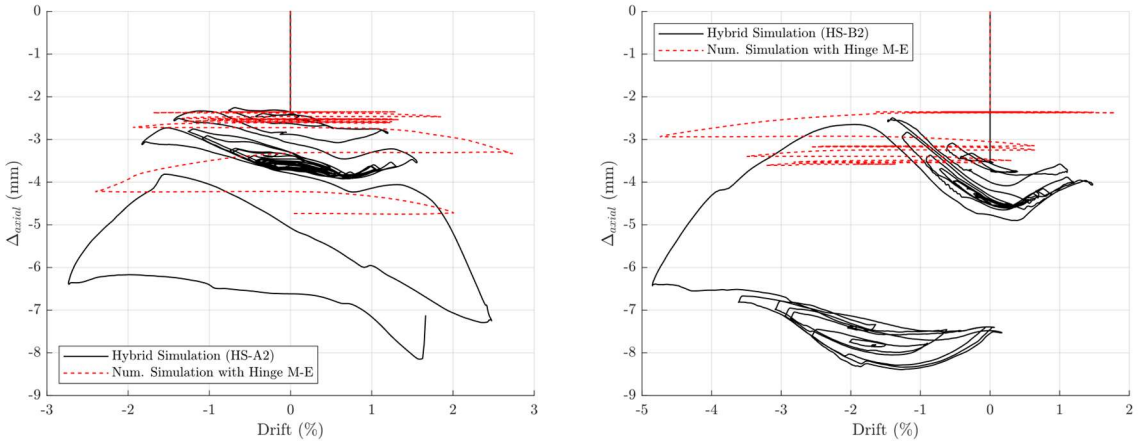

(A) (B)

Figure 6.11: Comparison of Δ_{axial} from hybrid tests and numerical simulation: (A) HS-A2; (B) HS-B2.

6.5. Assessment of Axial Shortening in Building Structures

The frame building models for archetypes A and B were used to perform a probabilistic assessment of the expected axial shortening for a set of ground motions scaled to MCE level. A suite of 30 ground-motions obtained from the NGA-WEST database [93] was selected and scaled following the conditional mean spectrum method [94,95], using the Matlab tool developed by Baker [96]. Figure 6.12 shows the response spectrum of the 30 scaled ground motions.

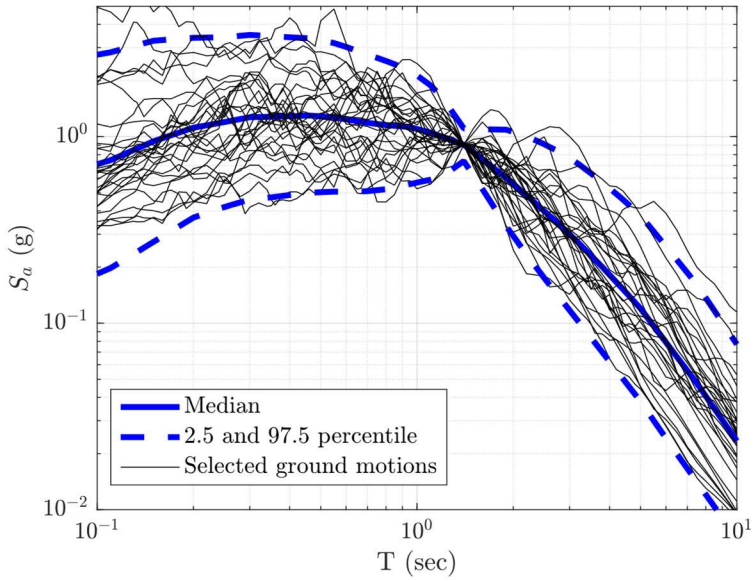

Figure 6.12: Response spectra of the selected ground motions.

Following the original design, the gravity forces of interior columns for archetypes A and B are equivalent to C_a=8.5% and 6.5%, respectively. Additionally, gravity loads were modified to target C_a coefficient of 20%, 30%, and 40% to examine more critical cases. Select cases are examined in this study.

First, the effect of far-field and near-fault ground motions is analyzed using archetype building A with an axial load level equivalent to C_a=20%. Figure 6.14 shows the response for the 1999 Chi-Chi Earthquake station CHY015 as an example of a far-field record. The first story drift response shows several large and relatively symmetric cycles, with a peak of 4%, and minor residual drift. The Δ_{axial} obtained for this case is similar between the interior columns, reaching a maximum of around 20 mm. Axial loads in interior columns are similar, with minor variations observed over time. A slight axial load redistribution can be observed for interior columns with the center column maintaining the largest load. Column 2 and 4 starts with an axial load of C_a=20%, and shift to around 18.4% by the end of the simulation. Although columns 2 and 4 are

located next to the exterior columns, the cyclic variation due to overturning effects is negligible. Exterior columns show smaller Δ_{axial}, with limited differences between them. Axial loads present significant oscillations, reaching up to C_a=33% in compression, and C_a=11% in tension.

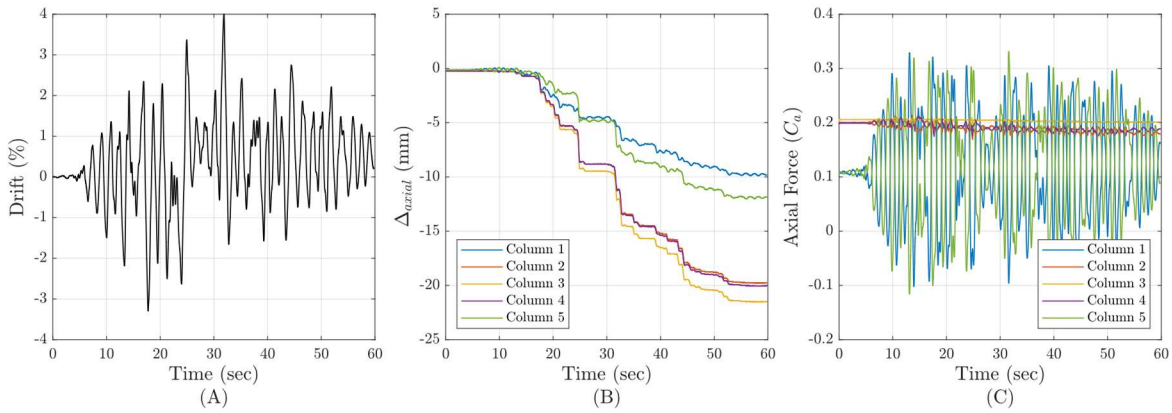

Figure 6.13: Response of archetype building A, axial load C_a=20%, Chi-Chi earthquake (1999): (A) First story drift; (B) Δ_{axial} of the five columns; (C) Axial force history for the five columns.

Figure 6.13 shows the response of archetype A subjected to the 1994 Northridge Earthquake, taking station "Jensen Filter Plant Administrative Building" as an example of near-fault record. The first story drift shows a large pulse leading to a peak of 5.2% and significant residual deformation of about 2%, which is larger than the previous ground motion. The Δ_{axial} in interior columns exhibit similar values as for the previous ground motion. Axial load levels also present small variations over time. There is a reduction in the axial load taken by the interior columns from C_a=20% to 15.7% when the peak lateral deformation occurs, then the initial axial load level is recovered after the peak. Exterior columns present an important difference in terms of Δ_{axial}. Despite the axial load variation, column 1 presents a vertical displacement similar than the one observed for interior columns. This could be attributed to the pulse-like motion causing a large displacement reversal leading to the peak response and concentrating most of the dissipated

column hinge energy within a small period of time. During this time, Column 1 sustained an increased axial load of around C_a=30% while column 5 is in tension.

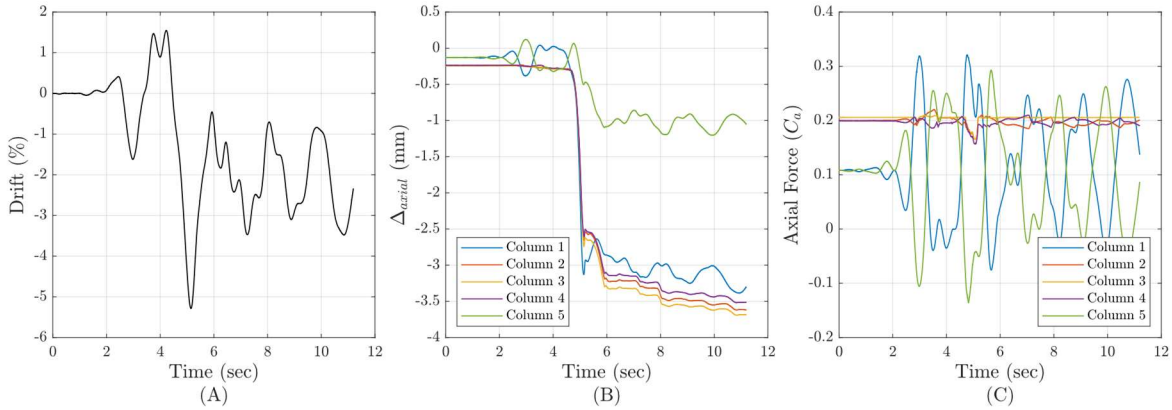

Figure 6.14: Response of archetype building A, axial load C_a=20%, Northridge earthquake (1994): (A) First story drift; (B) Δ_{axial} of the five columns; (C) Axial force history for the five columns.

The far-field motion provided more significant Δ_{axial} compared to the near-fault ground motion with a larger peak drift. Both ground motions produce small axial load variations in axial loads and column shortening for the three interior columns. A similar axial load variation was observed during test HS-B2, which was also a near-fault ground motion that produced 5% peak story drift. Furthermore, the similar behavior between interior columns supports the assumption of representing the three interior columns with a single specimen in the hybrid simulations.

Archetype A and B were subjected to the 30 ground motions for four different gravity force levels. Figure 6.15 shows the cumulative distribution of the Δ_{axial} obtained at the end of each simulation for the middle column. Columns of archetype A exhibit larger Δ_{axial} compared to archetype B for all the axial load levels. Considering the axial load levels obtained from the design, both column sections experienced a median value (cumulative probability of 0.5) less than 2 mm.

Based on the experimental observations of this study, such magnitude is likely related to steel yielding and not column buckling.

For axial load equivalent to C_a=20%, the median values for column sections A and B are 4.0 mm and 1.3 mm, respectively. Both quasi-static and hybrid tests induced Δ_{axial} greater than 4.0 mm on archetype A, but only the quasi-static protocol provoked local buckling initiation by this level. Although hybrid test may be considered more realistic, conclusions about expected buckling need further investigation. On the other hand, the Δ_{axial} of 1.3 mm estimated as median value for column section B is unlikely to be related to column buckling based on both quasi-static and hybrid simulation observations.

Axial loads of C_a=30% and 40% are considered more extreme cases. In archetype A these axial load levels induced median values of Δ_{axial} of 10 mm and 33 mm, respectively, while for archetype B they produced shortening of 3 mm and 8.5 mm, respectively.

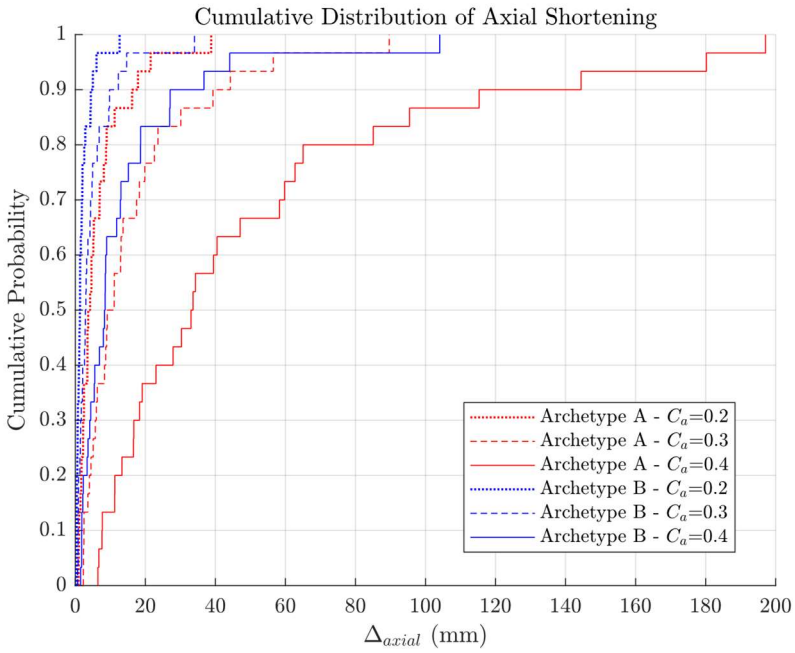

Figure 6.15: Cumulative distribution of Δ_{axial} for both archetypes and four gravity force levels.

Given the complexity of judging whether the expected values fall within an acceptable range, the definition of thresholds is desirable. Elkady et al. [5] conducted an international survey to determine limits for Δ_{axial} that could lead to irreparable column damage due to buckling, potentially resulting in the demolition of a steel frame building. Results were categorized into three geographical regions: "North America," "Europe," and "Japan and New Zealand," with median limits of 24 mm, 11 mm, and 10 mm, respectively. For this study, only the values from "North America" (NA) and "Europe" (EU) are utilized, given the similarities between "Europe" and "Japan and New Zealand" limits. Figure 6.16 depicts the cumulative distribution of Δ_{axial} in a semi-log plot and the limits mentioned above. Median shortening for archetype A with C_a=40% exceeds both limits, while C_a=30% induces a median Δ_{axial} exceeding the NA limit only, but close to EU limit. Median values of shortening for archetype B does not exceed any limit.

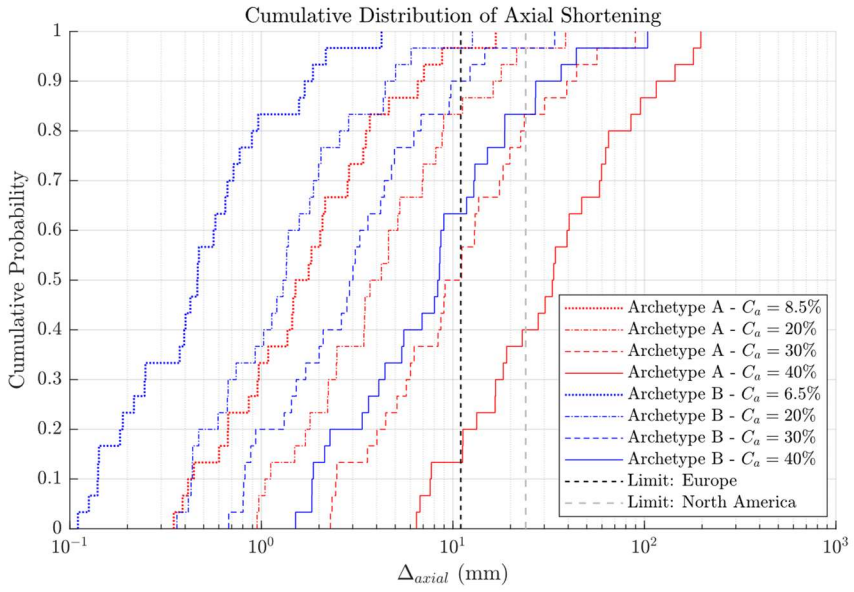

Figure 6.16: Semi-log cumulative distribution of Δ_{axial} including demolition limits.

The severity of the expected residual shortening for each case was evaluated by calculating the percentage of ground motions resulting in Δ_{axial} exceeding both NA and EU limits. Figure 6.17 depicts the results obtained together with the slenderness limit requirements for highly ductile members of AISC 341-16 [47] and AISC 341-22 [48]. With lower axial loads, there is a reduced number of records exceeding the NA and EU shortening limits, as expected. Furthermore, upon complying with the AISC 341-22 requirement, both archetypes exhibit no records surpassing the NA limit, and only one record exceeds the EU limit (3.3%). The analysis of these archetypes indicates that complying with AISC 341-22 slenderness requirement for highly ductile members significantly lowers the risk of building demolition due to column buckling in an MCE scenario.

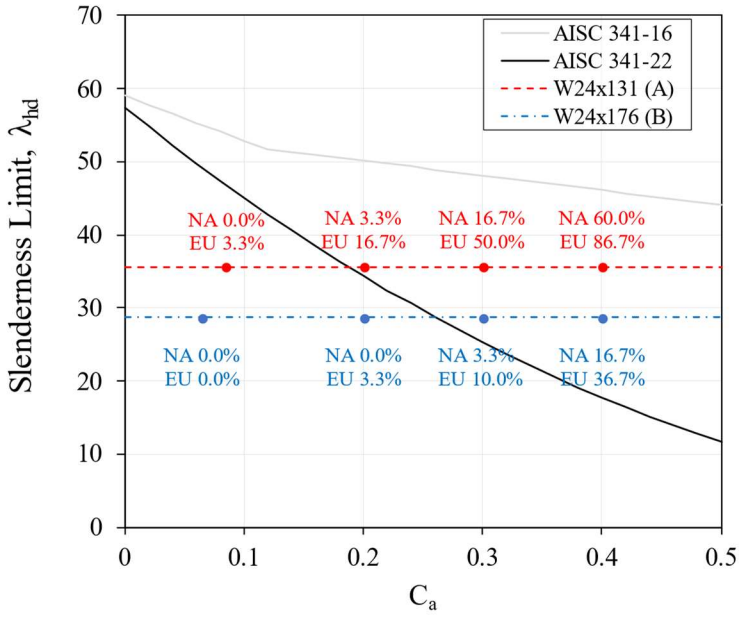

Figure 6.17: Highly ductile slenderness limits and ground motions exceeding Δ_{axial} limits.

Chapter 7 Summary and Conclusions

7.1. Summary of research work performed

A series of quasi-static tests (QS) and hybrid simulations (HS) of four full-scale beam-column subassembly were performed to study the seismic behavior of steel moment frames with deep and slender column sections. This study complements previous experimental studies carried out on individual column members. The testing was conducted on two different column sections: W24x131 and W24x176, each paired with beams following code compliant design. Each size of column was subjected to a standard QS loading protocol and the second specimen was subjected to HS that included a sequence for four ground motions ranging from DBE to MCE. The data obtained can support numerical model development and calibrations for both columns and beams with RBS.

A new framework to conduct hybrid simulations in mixed displacement and force control mode is proposed. Within a displacement-based integration scheme, select DOFs can be driven in force-control, to apply loads on stiff DOFs, and the measured displacement is fed back to the numerical substructure. Using linear control theory, an equivalent external force is applied to the

numerical model to enforce displacement compatibility between the numerical and experimental substructures that had previously been neglected.

Online model updating (OMU) was implemented to improve the numerical modeling of RBS hinges and have better agreement with the measured response of the experimental substructure. Data collected from one experimental beam RBS hinge was used to update several instances of numerical hinges in the model and the use of selective model updating concept was proposed to account for sudden failure such as fracture.

The experimental data collected from this and previous studies was used to propose a numerical hinge macro-element that can capture both: i) the degrading moment response of a wide-flange column due to buckling, and ii) the expected axial shortening (Δ_{axial}) simulated through an empirical expression. The element was implemented within the prototype building frame models to assess the expected Δ_{axial} for a maximum-considered earthquake (MCE) scenario.

7.2. Main findings and contributions

The main findings about the behavior of the specimens are summarized below:

- Quasi-static protocols were shown to results in more damage for beams and columns compared to the loading history imposed by historical ground motions using HS. Specifically, strength degradation, buckling severity, and column shortening are the observed measurements impacted by the loading history. This suggests that damage induced by symmetric quasi-static protocols is a conservative estimate of the expected damage during earthquake-induced loads for the same maximum lateral deformation.
- The lower torsional stiffness of the column for archetype A and the tendency of RBS to experience local and lateral-torsional buckling led to increased instabilities at the beam-

column connection. This was also the case for the HS, when the column did not show significant buckling but had induced torsion by RBS buckling. This behavior should be further evaluated considering the constraints imposed by the presence of the diaphragm not included in this study. However, the composite action of the slab and beam may be limited since studs may not be present in the RBS region.

- Specimen B with lower slenderness showed a more stable behavior based on column and RBS response as expected. However, if the column is subjected to moderate to high axial loads, the column may not be able to sustain large deformations before experiencing local and global buckling.
- Axial shortening observed during HS seems more related to steel yielding than column buckling when axial loads up to C_a=20% are applied. In contrast, when the specimens were subjected to either a QS loading pattern or axial loads greater than C_a=20% for QS or HS, column buckling started to be the most critical source of axial shortening. Around 90% of the total axial shortening for QS-A and QS-B can be assumed as buckling-related, and 80% for HS-B.
- According to AISC 341-16 [47] a highly ductile member should handle at least 4% drift deformation with less than 20% strength degradation. Both quasi-static tests QS-A and QS-B did not comply with this requirement during this experimental program, which is consistent with the new proposed limits of AISC 341-22 [48].
- The buckling mode of archetype A during both quasi-static and hybrid simulation was antisymmetric local buckling, while for archetype B it was a combination of antisymmetric local, lateral-torsional and out-of-plane global buckling, called coupled buckling. This

trend is in agreement with observations of individual columns and expected behavior as proposed by Ozkula and Uang [2].

- Experimental observations of member-level quasi-static column tests agree well with the data obtained from QS and HS subassembly tests conducted in this study. Among the most important similarities are the overall column buckling modes depending on the column section, moment response envelope, level of axial shortening, and the level of deformation that triggers yielding and column buckling.

The key contribution and findings of the proposed mixed displacement and force control framework for hybrid simulation are summarized below:

- This method can be incorporated into a wide range of computational platforms. It only requires calculation of an equivalent nodal force at each time step based on the measured and numerical displacements. It is applied here using OpenSees with OpenFresco as the middleware. An earlier version of this approach was implemented by Wang et al. [61] using PISA3D with NCREE-developed middleware [97].
- The axial load was successfully applied in force-control using hydraulic jacks. More accurate and expensive servo-controlled actuators are not necessary and this can extend the application of this approach to large scale specimens in more laboratories.
- The equivalent force transformation is based on closed-loop control theory applied here using simple algorithms. The performance of the method can be improved by using more complex controllers. This approach also avoids additional iterations withing the numerical integrator that are time consuming and computational expensive.
- The controller-based transformation can be tuned to improve tracking of the measured displacement within the numerical model, and should also consider stability by filtering

the measured noise. The reliability of the method will depend on the displacement measurement setup and the required tracking performance.

The key contributions of this study related to the Online Model Updating feature are summarized as follows:

- OMU was successfully implemented in the full-scale HS of a complex structural system and found to be stable without compromising the stability of the HS.
- The range of HS tests conducted, including HS-B1 and HS-B2, exhibited the performance of OMU in application from elastic level to large rotation nonlinear behavior. For the elastic level, the algorithm ignored the hysteresis from friction in the test setup. For larger demands the OMU was found capable to well capture the hysteretic behavior.
- Through a comparative analysis between distinct fitting strategies and numerical models, the model updating algorithm outperformed the static model parameters when the BW model is employed, in both calibrated and non-calibrated initial parameters cases.
- Further comparisons showed that updating only 3 parameters of BW model is enough to capture the RBS response, providing a better performance than IMK with 24 static parameters.
- The improvement in the accuracy of beam simulation through OMU produced minor differences in the system level behavior of the frame. However, it improves the local boundary conditions of the surrounding elements such as the first story column.
- The selective model updating was successfully implemented and tested through virtual hybrid simulation. This approach maintains the hysteretic features for both fractured and non-fractured hinges and provides a meaningful behavior depending on the state of each numerical element.

- Incorporating the selective model updating approach provides a more realistic simulation of the beam fracture within the numerical substructure. This proved to have an impact even at the global structure level, changing the story drifts by up to 15%.

The findings obtained from the development of column hinge macro-element with shortening and its application in numerical assessment of frames are detailed below:

- Experimental data of deep and slender columns on full-scale subassembly and member level tests was used to propose an empirical formula to predict the expected axial shortening due to column buckling.
- A macro-element was proposed to simulate the column response including the strength degradation and axial shortening. This approach enables the simulation of frame system behavior with deep and slender columns more efficiently than with high-fidelity finite element models.
- The numerical model of both prototype buildings studied in this work were subjected to 30 ground motions scaled to MCE. The simulations included gravity loads obtained from the design, and additional cases with increased axial loads.
- Numerical results showed that when the studied columns comply with the slenderness limit requirements for highly ductile members of AISC 341-22 [48], shortening under MCE ground motions is limited and likely to be less than proposed requirements triggering building demolition.

7.3. Recommendation for future research work

The series of tests provided herein are a valuable dataset on full-scale testing of SMF subassemblies. This study provides an overview of the testing program and highlights experimental observations. However, there are additional analysis that can be carried out to improve the understanding of deep and slender wide-flange columns. Some of these aspects are mentioned below:

- More detailed analyses are needed to fully compare different archetype buildings with deep and slender columns. This includes system level seismic assessment through experimental and numerical studies.
- The influence of slab constraints may impact the twisting of archetype A and global buckling of archetype B. While isolated column tests fixed torsional and out-of-plane rotations at the beam-column connection, subassembly tests allowed partial movement. Incorporating the slab could limit the severity of this behavior, but not necessarily prevent them. Further subassembly testing, including column axial load and slab presence, is essential to better assess the slab effects on the system buckling behavior.
- Even though most of the measured data was used to analyze the behavior of key sections of each specimen, there remains measurements that have not been analyzed in detail, such as the panel zone response, identification of global deformation through MoCap 3D positions measurements, among others.
- Most full-scale experimental data in the literature focuses on the behavior of interior columns, with constant axial load. Although there is experimental and numerical evidence indicating that axial load cycles delay column buckling, further studies are necessary to

address this aspect impacting exterior columns of moment frames, and columns of braced frames.

The proposed mixed displacement and force control framework for HS was applied with large-scale tests and further studies can be used to improve and expand HS capabilities including:

- The controller of the transformation can be more advanced and include delay compensation.
- The method was implemented for only one DOF driven in force-control. Further analyses are needed to expand the application of the framework for multiple coupled DOFs.
- To improve efficiency, the method could be implemented within the middleware or a real-time processor. Furthermore, currently the controller uses one step per integration-step to reduce the displacement error. The performance of the controller-based transformation can be improved by using sub-steps for the controller-transformation.
- The proposed framework was implemented in a full-scale HS with the time scaled to velocity limitations imposed by loading rate of the actuators. The numerical components had sufficient time for computation including the controller-based transformation. Further studies are needed to examine the potential use for real-time hybrid simulation.

This study provides compelling evidence that model updating can be a crucial tool to improve the reliability and precision of the HS. This approach helps foster the understanding of structural behavior under various conditions. Nevertheless, there are still areas that need further investigation, such as:

- The cyclic degradation of RBS response was simulated through the change in the identified stiffness and strength for a more stable simulation. Additional studies can include the cyclic degrading as a separated parameter into the hysteretic model.
- The selective model updating was proposed to trigger beam fracture for the numerical beams with a deterministic approach. Further studies should introduce the randomness and uncertainty of the fracture problem into the selective updating algorithm.
- Rules based on fracture theory and additional measured data can be included to the selective updating algorithm to improve the accuracy of fracture occurrence for the numerical beams.

Finally, a hinge macro-element is proposed to simulate the degrading moment response and expected axial shortening of the column sections studied herein. Future work should address the following aspects:

- A wider range of experimental and numerical data should be used to increase the applicability of the empirical expression for axial shortening estimation. The most important variables that need to be included are different column sections, and more data obtained from seismic load patterns instead of symmetric cyclic patterns.
- The empirical expression showed to be applicable for one test with varying axial load. More cases like this should be included to increase the reliability of the expression for exterior columns and columns of braced frames.
- Numerical simulations were performed to replicate the axial shortening measured during the hybrid tests. Since the axial shortening was limited on those tests, the expected

shortening did not present reasonable accuracy. Tests with larger shortening should be used to verify the accuracy of the hinge macro-element for more critical cases.

REFERENCES

[1] ASCE. ASCE/SEI 7-16 Minimum Design Loads and Associated Criteria for Buildings and Other Structures. American Society of Civil Engineers; 2016.

[2] Ozkula G, Uang C-M. Classification and Identification of Buckling Modes of Steel Columns under Cyclic Loading. Journal of Structural Engineering 2023;149. https://doi.org/10.1061/JSENDH.STENG-12156.

[3] Elkady A, Lignos DG. Analytical investigation of the cyclic behavior and plastic hinge formation in deep wide-flange steel beam-columns. Bulletin of Earthquake Engineering 2015;13:1097–118. https://doi.org/10.1007/s10518-014-9640-y.

[4] Ozkula G. Seismic Behavior, Modeling, and Design of Deep Wide-Flange Steel Columns for Special Moment Frames. Ph.D. Thesis. University of California San Diego, 2017.

[5] Elkady A, Güell G, Lignos DG. Proposed methodology for building-specific earthquake loss assessment including column residual axial shortening. Earthq Eng Struct Dyn 2020;49:339–55. https://doi.org/10.1002/EQE.3242.

[6] Islam A, Imanpour A. Stability of wide-flange columns in steel moment-resisting frames: evaluation of the Canadian seismic design requirements. Bulletin of Earthquake Engineering 2022:1591–617. https://doi.org/10.1007/s10518-021-01313-8.

[7] Stoakes CD, Fahnestock LA. Strong-Axis Stability of Wide Flange Steel Columns in the Presence of Weak-Axis Flexure. Journal of Structural Engineering 2016;142. https://doi.org/10.1061/(ASCE)ST.1943-541X.0001448.

[8] Fogarty J, Wu TY, El-Tawil S. Collapse Response and Design of Deep Steel Columns Subjected to Lateral Displacement. Journal of Structural Engineering 2017;143:04017130. https://doi.org/10.1061/(ASCE)ST.1943-541X.0001848/ASSET/14BBF54A-57B4-43DE-9BF1-7D85A823D9C4/ASSETS/IMAGES/LARGE/FIGURE15.JPG.

[9] Ozkula G, Uang C-M, Harris J. Development of Enhanced Seismic Compactness Requirements for Webs in Wide-Flange Steel Columns. Journal of Structural Engineering 2021;147:04021100. https://doi.org/10.1061/(ASCE)ST.1943-541X.0003036.

[10] Elkady A, Lignos DG. Full-Scale Testing of Deep Wide-Flange Steel Columns under Multiaxis Cyclic Loading: Loading Sequence, Boundary Effects, and Lateral Stability Bracing Force Demands. Journal of Structural Engineering 2017;144. https://doi.org/10.1061/(ASCE)ST.1943-541X.0001937.

[11] Chansuk P, Ozkula G, Uang C-M, Harris JL. Seismic Behavior and Design of Deep, Slender Wide-Flange Structural Steel Beam-Columns. Gaithersburg, MD: 2021. https://doi.org/10.6028/NIST.TN.2169.

[12] Chou C, Lai Y, Xiong H, Lin T, Uang C, Mosqueda G, et al. Effect of boundary condition on the cyclic response of I-shaped steel columns: Two-story subassemblage versus isolated column tests. Earthq Eng Struct Dyn 2022;51:3434–55. https://doi.org/10.1002/EQE.3730.

[13] Wu T-Y, El-Tawil S, McCormick J. Seismic Collapse Response of Steel Moment Frames with Deep Columns. Journal of Structural Engineering 2018;144. https://doi.org/10.1061/(ASCE)ST.1943-541X.0002150.

[14] Islam A, Imanpour A. Seismic stability of steel wide-flange columns in ductile moment-resisting frames: out-of-plane response and design recommendations. Bulletin of Earthquake Engineering 2023;21:3493–519. https://doi.org/10.1007/S10518-023-01653-7/FIGURES/12.

[15] MacRae GA, Urmson CR, Walpole WR, Moss P, Hyde K, Clifton C. Axial shortening of steel columns in buildings subjected to earthquakes. Bulletin of the New Zealand Society for Earthquake Engineering 2009;42:275–87. https://doi.org/10.5459/bnzsee.42.4.275-287.

[16] Suzuki Y, Lignos DG. Development of collapse-consistent loading protocols for experimental testing of steel columns. Earthq Eng Struct Dyn 2020;49:114–31. https://doi.org/10.1002/EQE.3225.

[17] McKenna F, Scott MH, Fenves GL. Nonlinear Finite-Element Analysis Software Architecture Using Object Composition. Journal of Computing in Civil Engineering 2009;24:95–107. https://doi.org/10.1061/(ASCE)CP.1943-5487.0000002.

[18] Schellenberg AH, Mahin SA, Fenves GL. Advanced Implementation of Hybrid Simulation. Berkeley, CA, USA: 2009.

[19] Mahin SA, Shing P-SB. Pseudodynamic Method for Seismic Testing. Journal of Structural Engineering 1985;111:1482–503. https://doi.org/10.1061/(ASCE)0733-9445(1985)111:7(1482).

[20] Takanashi K, Udagawa K, Seki M, Okada T, Tanaka H. Nonlinear earthquake response analysis of structures by a computer-actuator on-line system. Bulletin of Earthquake Resistant Structure Research Center 1975;8:1–17.

[21] Sivaselvan M V., Reinhorn AM, Shao X, Weinreber S. Dynamic force control with hydraulic actuators using added compliance and displacement compensation. Earthq Eng Struct Dyn 2008;37:1785–800. https://doi.org/10.1002/EQE.837.

[22] Bousias SN. Seismic Hybrid Simulation of Stiff Structures: Overview and Current Advances. Journal of Structures 2014;2014:1–8. https://doi.org/10.1155/2014/825692.

[23] Hashemi MJ, Mosqueda G, Lignos DG, Medina RA, Miranda E. Assessment of Numerical and Experimental Errors in Hybrid Simulation of Framed Structural Systems

through Collapse. Journal of Earthquake Engineering 2016;20:885–909. https://doi.org/10.1080/13632469.2015.1110066.

[24] Giotis G, Kwon O-S, Eng P, Sheikh SA. Weakly Coupled Hybrid Simulation Method for Structural Testing: Theoretical Framework and Numerical Verification. Journal of Structural Engineering 2020;146. https://doi.org/10.1061/(ASCE)ST.1943-541X.0002492.

[25] Chen Z, Xu G, Wu B, Sun Y, Wang H, Wang F. Equivalent force control method for substructure pseudo-dynamic test of a full-scale masonry structure. Earthq Eng Struct Dyn 2014;43:969–83. https://doi.org/10.1002/eqe.2382.

[26] Woods JE, Lau DT, Erochko J. Evaluation by Hybrid Simulation of Earthquake-Damaged RC Walls Repaired for In-Plane Bending with Single-Sided CFRP Sheets. Journal of Composites for Construction 2020;24. https://doi.org/10.1061/(ASCE)CC.1943-5614.0001085.

[27] Wu AC, Tsai KC, Yang HH, Huang JL, Li CH, Wang KJ, et al. Hybrid experimental performance of a full-scale two-story buckling-restrained braced RC frame. Earthq Eng Struct Dyn 2016;46:1223–44. https://doi.org/10.1002/eqe.2853.

[28] Pan P, Nakashima M, Tomofuji H. Online test using displacement-force mixed control. Earthq Eng Struct Dyn 2005;34:869–88. https://doi.org/10.1002/eqe.457.

[29] Del Carpio M, Mosqueda G, Hashemi MJ. Large-Scale Hybrid Simulation of a Steel Moment Frame Building Structure through Collapse. Journal of Structural Engineering 2015;142. https://doi.org/10.1061/(ASCE)ST.1943.

[30] Chae Y, Lee J, Park M, Kim CY. Real-time hybrid simulation for an RC bridge pier subjected to both horizontal and vertical ground motions. Earthq Eng Struct Dyn 2018;47:1673–9. https://doi.org/10.1002/EQE.3042.

[31] Imanpour A, Tremblay R, Leclerc M, Siguier R, Toutant G, Balazadeh Minouei Y, et al. Development and application of multi-axis hybrid simulation for seismic stability of steel braced frames. Eng Struct 2022;252:113646. https://doi.org/10.1016/J.ENGSTRUCT.2021.113646.

[32] Whyte C, Stojadinovic B. Use of a High-Precision Digital Displacement Encoder for Hybrid Simulation of Seismic Response of Stiff Specimens. Exp Tech 2016;40:677–88. https://doi.org/10.1007/s40799-016-0069-x.

[33] Wu B, Wang Q, Benson Shing P, Ou J. Equivalent force control method for generalized real-time substructure testing with implicit integration. Earthq Eng Struct Dyn 2007;36:1127–49. https://doi.org/10.1002/eqe.674.

[34] Kim HK. Development and implementation of advanced control methods for hybrid simulation. Ph.D. Thesis. University of California, Berkeley, 2011.

[35] Takahashi Y, Fenves GL. Software framework for distributed experimental–computational simulation of structural systems. Earthq Eng Struct Dyn 2006;35:267–91. https://doi.org/10.1002/EQE.518.

[36] Ahmadizadeh M, Mosqueda G. Hybrid Simulation with Improved Operator-Splitting Integration Using Experimental Tangent Stiffness Matrix Estimation. Journal of Structural Engineering 2008;134:1829–38. https://doi.org/10.1061/(ASCE)0733-9445(2008)134:12(1829).

[37] Carlson NN, Miller K. Design and Application of a Gradient-Weighted Moving Finite Element Code I: in One Dimension. SIAM Journal on Scientific Computing 1998;19:728–65. https://doi.org/10.1137/S106482759426955X.

[38] Kim HK, Whyte C, Stojadinovic B. Force, Mixed And Switch Degree-Of-Freedom Control In Hybrid Simulation. 9th U.S. National and 10th Canadian Conference on Earthquake Engineering, 2010.

[39] Du C, Wang T, Qie Y, Marino · Edoardo, Zhou · Huimeng. Staggered coordination in substructure online hybrid test on a RC frame retrofitted by BRBs. Bulletin of Earthquake Engineering 2019;17:4141–67. https://doi.org/10.1007/s10518-019-00636-x.

[40] Kwon OS, Kammula V. Model updating method for substructure pseudo-dynamic hybrid simulation. Earthq Eng Struct Dyn 2013;42:1971–84. https://doi.org/10.1002/EQE.2307.

[41] Hashemi MJ, Masroor A, Mosqueda G. Implementation of online model updating in hybrid simulation. Earthq Eng Struct Dyn 2014;43:395–412. https://doi.org/10.1002/EQE.2350.

[42] Wan EA, Van Der Merwe R. The unscented Kalman filter for nonlinear estimation. IEEE 2000 Adaptive Systems for Signal Processing, Communications, and Control Symposium, Lake Louise, AB, Canada: Institute of Electrical and Electronics Engineers Inc.; 2000, p. 153–8. https://doi.org/10.1109/ASSPCC.2000.882463.

[43] Al-Subaihawi S, Ricles JM, Quiel SE. Online explicit model updating of nonlinear viscous dampers for real time hybrid simulation. Soil Dynamics and Earthquake Engineering 2022;154:107108. https://doi.org/10.1016/J.SOILDYN.2021.107108.

[44] Cheng M, Becker TC. Performance of unscented Kalman filter for model updating with experimental data. Earthq Eng Struct Dyn 2021;50:1948–66. https://doi.org/10.1002/EQE.3426.

[45] Dertimanis VK, Zürich E, Betti M, Giagopoulos D, Ou G, Yang G, et al. Investigation of Hybrid Simulation With Model Updating Compared to an Experimental Shake Table Test. Front Built Environ 2020;6:103. https://doi.org/10.3389/fbuil.2020.00103.

[46] Wang K, Chuang M, Tsai K, Li C, Chin P, Chueh S. Hybrid testing with model updating on steel panel damper substructures using a multi-axial testing system. Earthq Eng Struct Dyn 2019;48:347–65. https://doi.org/10.1002/eqe.3139.

[47] AISC. ANSI/AISC 341-16 Seismic provisions for steel structural buildings. American Institute of Steel Construction; 2016.

[48] AISC. ANSI/AISC 341-22 Seismic provisions for steel structural buildings. American Institute of Steel Construction; 2022.

[49] AISC. ANSI/AISC 358-16 Prequalified connections for special and intermediate steel moment frames for seismic applications. Chicago, IL: American Institute of Steel Construction; 2016.

[50] AISC. ANSI/AISC 360-16 Specification for Structural Steel Buildings. American Institute of Steel Construction; 2016.

[51] Gupta A, Krawinkler H. Seismic Demands For Performance Evaluation Of Steel Moment Resisting Frame Structures. Blume Earthquake Engineering Center, 1999.

[52] Krawinkler H, Bertero V V, Popov EP. Shear Behavior of Steel Frame Joints. Journal of the Structural Division 1975;101:2317–36. https://doi.org/10.1061/JSDEAG.0004206.

[53] Ibarra LF, Medina RA, Krawinkler H. Hysteretic models that incorporate strength and stiffness deterioration. Earthq Eng Struct Dyn 2005;34:1489–511. https://doi.org/10.1002/EQE.495.

[54] Lignos DG, Krawinkler H. Deterioration Modeling of Steel Components in Support of Collapse Prediction of Steel Moment Frames under Earthquake Loading. Journal of Structural Engineering 2011;137. https://doi.org/10.1061/(ASCE)ST.1943-541X.0000376.

[55] Sepulveda C, Cheng M, Becker T, Mosqueda G, Wang K-J, Huang B-C, et al. Selective Online Model Updating in Hybrid Simulation of a Full-Scale Steel Moment Frame. Earthquake Engineering and Structural Dynamics (under Review) 2024.

[56] Sepulveda C, Mosqueda G, Uang C, Chou CC, Wang KJ. Hybrid Simulation Using Mixed Displacement and Equivalent-Force Control to Capture Column Shortening in Frame Structures. 12th National Conference on Earthquake Engineering, NCEE 2022, 2022.

[57] Ozkula G, Sepulveda C, Mosqueda G, Uang C-M. Seismic Compactness Requirement for I-Shaped Columns with Varying Axial Load. 11th International Conference on Behaviour of Steel Structures in Seismic Areas (STESSA), Salerno, Italy: 2024.

[58] Hashemi MJ, Mosqueda G. Innovative substructuring technique for hybrid simulation of multistory buildings through collapse. Earthq Eng Struct Dyn 2014;43:2059–74. https://doi.org/10.1002/eqe.2427.

[59] Sepulveda C, Mosqueda G, Wang K-J, Huang B-C, Huang C-W, Uang C-M, et al. Hybrid Simulation Framework with Mixed Displacement and Force Control for Fully Compatible Displacements. Earthq Eng Struct Dyn 2024;53:838–55. https://doi.org/10.1002/eqe.4048.

[60] Stojadinovic B, Mosqueda G, Mahin SA. Event-Driven Control System for Geographically Distributed Hybrid Simulation. Journal of Structural Engineering 2006;132:68–77. https://doi.org/10.1061/(ASCE)0733-9445(2006)132:1(68).

[61] Wang K, Chou C, Huang C, Shen H, Sepulveda C, Mosqueda G, et al. Hybrid simulation of a steel dual system with buckling-induced first-story column shortening: A mixed control mode approach. Earthq Eng Struct Dyn 2023;52:3727–45. https://doi.org/10.1002/EQE.3944.

[62] MacRae G. The seismic response of steel frames. Ph.D. Thesis. University of Canterbury, 1989.

[63] Elkady A, Lignos DG. Improved Seismic Design and Nonlinear Modeling Recommendations for Wide-Flange Steel Columns. Journal of Structural Engineering 2018;144. https://doi.org/10.1061/(ASCE)ST.1943-541X.0002166.

[64] Ozkula G, Harris JL, Uang C-M. Buckling-Induced Shortening Of Deep W-Shape Columns In Seismic Steel Frames. 11th U.S. National Conference on Earthquake Engineering, 2018.

[65] Sepulveda C, Mosqueda G, Uang C-M, Chou C-C, Wang K-J. Hybrid Simulation Using Mixed Displacement and Equivalent-Force Control to Capture Column Shortening in Frame Structures. 12th National Conference on Earthquake Engineering, Salt Lake City, Utah, USA: 2022.

[66] Lin BZ, Chuang MC, Tsai KC. Object-oriented development and application of a nonlinear structural analysis framework. Advances in Engineering Software 2009;40:66–82. https://doi.org/10.1016/J.ADVENGSOFT.2008.03.012.

[67] Hashemi MJ, Al-Ogaidi Y, Al-Mahaidi R, Kalfat R, Tsang H-H, Wilson JL. Application of Hybrid Simulation for Collapse Assessment of Post-Earthquake CFRP-Repaired RC Columns. Journal of Structural Engineering 2017;143. https://doi.org/10.1061/(ASCE)ST.1943-541X.0001629.

[68] Al-Attraqchi AY, Hashemi MJ, Al-Mahaidi R. Hybrid simulation of bridges constructed with concrete-filled steel tube columns subjected to horizontal and vertical ground motions. Bulletin of Earthquake Engineering 2020;18:4453–80. https://doi.org/10.1007/S10518-020-00871-7.

[69] Ziegler JG, Nichols NB. Optimum Settings for Automatic Controllers. J Dyn Syst Meas Control 1993;115:220–2. https://doi.org/10.1115/1.2899060.

[70] Schellenberg AH, Huang Y, Mahin SA. Structural Finite Element Software Coupling Using Adapter Elements. Computer Modeling in Engineering & Sciences 2019;120:719–37. https://doi.org/10.32604/CMES.2019.04835.

[71] Sepulveda C, Mosqueda G. Performance Assessment of a Mixed Displacement and Force Control Mode for Hybrid Simulation. 13th Chilean Conference of Seismology and Earthquake Engineering, Vina Del Mar: 2023.

[72] Horiuchi T, Inoue M, Konno T, Namita Y. Real-Time Hybrid Experimental System with Actuator Delay Compensation and its Application to a Piping System with Energy Absorber. Earthquake Engng Struct Dyn 1999;28:1121–41. https://doi.org/10.1002/(SICI)1096-9845(199910)28:10<1121::AID-EQE858>3.0.CO;2-O.

[73] Mosqueda G, Stojadinovic B, Mahin SA. Real-Time Error Monitoring for Hybrid Simulation. Part I: Methodology and Experimental Verification. Journal of Structural Engineering 2007;133. https://doi.org/10.1061/ASCE0733-94452007133:81100.

[74] Hashemi MJ. Collapse simulation of multi-story buildings through hybrid testing with substructuring techniques. Ph.D. Thesis. The State University of New York at Buffalo, 2013.

[75] Scott MH, Haukaas T. Software Framework for Parameter Updating and Finite-Element Response Sensitivity Analysis. Journal of Computing in Civil Engineering 2008;22. https://doi.org/10.1061/ASCE0887-3801200822:5281.

[76] Ma F, Zhang H, Bockstedte A, Foliente GC, Paevere P. Parameter analysis of the differential model of hysteresis. Journal of Applied Mechanics, Transactions ASME 2004;71. https://doi.org/10.1115/1.1668082.

[77] Jones SL, Gary ;, Fry T, Engelhardt MD. Experimental Evaluation of Cyclically Loaded Reduced Beam Section Moment Connections. Journal of Structural Engineering 2002;128:441–51. https://doi.org/10.1061/(ASCE)0733-9445(2002)128:4(441).

[78] Bruneau M, Uang C, Sabelli R. Ductile Design of Steel Structures. 2nd edition, McGraw Hill; 2008.

[79] Galvis FA, Deierlein GG, Hutt CM, Baker JW. High-fidelity modeling of fracture-critical welded steel beam-to-column connections and their impact on earthquake stability of tall buildings. Proceedings of the Annual Stability Conference Structural Stability Research Council, Denver, Colorado: 2022.

[80] Schellenberg A, Huang Y, Mahin SA. Structural FE-Software Coupling Through The Experimental Software Framework, OpenFresco. 14th World Conference on Earthquake Engineering, Beijin, China: 2008.

[81] Elkady A. Collapse risk assessment of steel moment resisting frames designed with deep wide-flange columns in seismic regions. Ph.D. Thesis. McGill University, 2016.

[82] Fogarty J, El-Tawil. Collapse Resistance of Steel Columns under Combined Axial and Lateral Loading. Journal of Structural Engineering 2016;142:04015091. https://doi.org/10.1061/(ASCE)ST.1943-541X.0001350.

[83] Ozkula G, Harris J, Uang C-M. Classifying Cyclic Buckling Modes of Steel Wide-Flange Columns under Cyclic Loading. Structures Congress, Denver, Colorado: 2017.

[84] Suzuki Y, Lignos DG. Experimental Evaluation of Steel Columns under Seismic Hazard-Consistent Collapse Loading Protocols. Journal of Structural Engineering 2021;147. https://doi.org/10.1061/(ASCE)ST.1943-541X.0002963.

[85] Neuenhofer A, Filippou FC. Evaluation of Nonlinear Frame Finite-Element Models. Journal of Structural Engineering 1997;123:958–66. https://doi.org/10.1061/(ASCE)0733-9445(1997)123:7(958).

[86] Kolwankar S, Kanvinde A, Kenawy M, Lignos D, Kunnath S. Simulating Local Buckling-Induced Softening in Steel Members Using an Equivalent Nonlocal Material Model in Displacement-Based Fiber Elements. Journal of Structural Engineering 2018;144. https://doi.org/10.1061/(ASCE)ST.1943-541X.0002189.

[87] Kolwankar S, Kanvinde A, Kenawy M, Lignos D, Kunnath S. Simulating Cyclic Local Buckling–Induced Softening in Steel Beam-Columns Using a Nonlocal Material Model in Displacement-Based Fiber Elements. Journal of Structural Engineering 2020;146. https://doi.org/10.1061/(ASCE)ST.1943-541X.0002457.

[88] Valipour HR, Foster SJ. Nonlocal Damage Formulation for a Flexibility-Based Frame Element. Journal of Structural Engineering 2009;135:1213–21. https://doi.org/10.1061/(ASCE)ST.1943-541X.0000054/ASSET/FE699171-4540-4A6C-BBBB-B6DED5347829/ASSETS/IMAGES/LARGE/13.JPG.

[89] Coleman J, Spacone E. Localization Issues in Force-Based Frame Elements. Journal of Structural Engineering 2001;127:1257–65. https://doi.org/10.1061/(ASCE)0733-9445(2001)127:11(1257).

[90] Maity A, Kanvinde A, Rosa DIH, Albano De Castro E Sousa ;, Lignos DG. A Displacement-Based Fiber Element to Simulate Interactive Lateral Torsional and Local Buckling in Steel Members. Journal of Structural Engineering 2023;149. https://doi.org/10.1061/JSENDH.STENG-11889.

[91] Alghossoon A, Varma AH. Fiber-based model for simulating strength and stiffness deterioration of high-strength steel beams. Thin-Walled Structures 2023;183:110432. https://doi.org/10.1016/j.tws.2022.110432.

[92] Cook RD, Saunders H. Concepts and Applications of Finite Element Analysis. 4th Edition. Wiley; 2001. https://doi.org/10.1115/1.3264300.

[93] Arteta CA, Torregroza A, Gaspar D, Abrahamson N. Sensitivity of the conditional period selection in the structural response using the CMS as target spectrum. Earthquake Spectra 2022;38:1844–71. https://doi.org/10.1177/87552930221081150.

[94] Baker JW, Lin T, Shahi SK, Jayaram N. New Ground Motion Selection Procedures and Selected Motions for the PEER Transportation Research Program. Berkeley: 2011.

[95] Baker JW, Lee C. An Improved Algorithm for Selecting Ground Motions to Match a Conditional Spectrum. Journal of Earthquake Engineering 2018;22:708–23. https://doi.org/10.1080/13632469.2016.1264334.

[96] Baker JW. Conditional Mean Spectrum: Tool for Ground-Motion Selection. Journal of Structural Engineering 2010;137:322–31. https://doi.org/10.1061/(ASCE)ST.1943-541X.0000215.

[97] Wang KJ, Tsai KC. A uniform method to integrate testing equipment for large-scale quasi-static structural testing. 6th International Conference on Advances in Experimental Structural Engineering, vol. 2015- August, Urbana-Champaign, United States: 2015.